Politecnico di Torino

大阪大学
THE UNIVERSITY OF OSAKA

Master of Science in

Aerospace Engineering

Master's Thesis

Validation of Cloud Profiling Radar (CPR) measurements from the EarthCARE mission using observations from the Multi-Parameter Phased Array Weather Radar (MP-PAWR)

Candidate

Michele Fiore

Supervisors

Prof. Alessandro Battaglia

Prof. Tomoo Ushio

Academic Year: 2024–2025

Abstract

This thesis analyses the reflectivity measurements acquired by the Cloud Profiling Radar (CPR) onboard the EarthCARE satellite, operated by the European Space Agency (ESA) in collaboration with the Japan Aerospace Exploration Agency (JAXA), and those provided by the Multi-Parameter Phased Array Weather Radar (MP-PAWR), located in the Osaka region, Japan.
The main objective is to quantitatively evaluate the level of agreement between the two data sources, identifying the main sources of discrepancy due to instrumental, geometric, and physical factors, and to assess the ability of the phased array radar to accurately represent the vertical structure of clouds and precipitation compared to a spaceborne reference system.
In the first phase, a detailed technical study of the operational characteristics of both radar systems was carried out, with particular attention to the minimum detectable sensitivity of the MP-PAWR.
This analysis allowed determining the detectability threshold of reflectivity as a function of distance, atmospheric attenuation, and the receiver system specifications.
In parallel, algorithms were developed for the visualization, processing, and comparison of EarthCARE and MP-PAWR radar data, including procedures to identify satellite overpasses above the ground-based radar scanning volume, determined through an accurate analysis of the ground track repeat cycle.
To ensure geometric consistency between the two datasets, MP-PAWR data were transformed into the same reference system as the CPR, including correction for Earth's curvature. After verifying the spatio-temporal correspondence, the effective intersection volume was selected, and a direct comparison of reflectivity measurements was conducted.
For validation purposes, a volumetric matching approach based on the method of Schwaller and Morris was implemented, taking into account both spatial proximity and the similarity of radar reflectivity values between points in the two datasets.
The mean bias, Root Mean Square Error (RMSE), and Pearson correlation coefficient were calculated, accompanied by graphical representations including scatter plots and latitude–altitude cross-sections.
Analysis of multiple case studies revealed that, despite spatial and temporal consistency between observations, the reflectivity measured by MP-PAWR

differs significantly from that of the CPR. This discrepancy is partly attributable to the operating frequency difference between the two instruments: the CPR operates at 94 GHz (W-band), sensitive to ice particles and small droplets, while the MP-PAWR operates at 9.71 GHz (X-band), more suited to detecting larger hydrometeors. This spectral divergence induces variations in scattering response, amplified by non-Rayleigh scattering effects, signal attenuation, and the application of the Moving Target Indication (MTI) filter in the phased array system.
Overall, the results indicate that the MP-PAWR cannot be considered a direct validation tool for EarthCARE CPR observations, due to the physical and operational differences between the two systems. However, this work highlights the importance of the phased array radar as an experimental platform for algorithm testing and the development of methodologies for comparing spaceborne and ground-based radar observations.

Contents

List of Figures

List of Tables

Introduction

Understanding atmospheric processes and meteorological variability requires detailed and continuous observations of cloud and precipitation properties. Vertical profiling radars, such as the Cloud Profiling Radar (CPR) onboard the EarthCARE (Earth Cloud, Aerosol and Radiation Explorer) satellite, provide high-resolution vertical measurements of cloud reflectivity, enabling critical insights into cloud microphysics and the vertical distribution of precipitation. Similarly, advanced ground-based radars, such as the Multi-Parameter Phased Array Weather Radar (MP-PAWR), deliver observations with high temporal and spatial resolution, allowing continuous monitoring of precipitation structure and evolution at the local scale.

Integrating and comparing satellite and ground-based radar data is crucial for several reasons. First, it allows validation and calibration of satellite observations, improving the quality of retrievals and numerical weather prediction models. Second, analysing discrepancies between the two systems helps to identify the limitations of each radar, which may be influenced by factors such as spatial and temporal resolution, system sensitivity, and attenuation effects. Quantifying these differences is essential to develop data fusion strategies and assess the reliability of atmospheric models.

The primary objective of this thesis is to compare radar reflectivity data acquired by the CPR and the MP-PAWR in the Osaka region, evaluating their consistency and identifying the main sources of divergence. To this end, tools were developed to extract vertical profiles along specific tracks and to visualize the data in both three-dimensional and two-dimensional formats, providing a comprehensive representation of the observed atmospheric phenomena.

The work is organised into several methodological steps. First, raw radar data are processed and georeferenced to align coordinates across the different systems. Then, vertical profiles are extracted along predetermined tracks using a volumetric matching approach based on the method of Schwaller

and Morris, taking into account both spatial proximity and the similarity of radar reflectivity values, thereby ensuring an accurate comparison between satellite and ground-based observations. Finally, advanced statistical tools are applied to quantify bias, root-mean-square error (RMSE), and correlation between the two datasets, providing a rigorous quantitative assessment of the differences observed.
This thesis is structured as follows: Chapter 2 presents the EarthCARE mission, including its scientific objectives, satellite instruments, and characteristics of the observation products; Chapter 3 discusses the fundamentals of radar systems, the measured physical quantities, and the main radar equations; Chapter 4 describes the MP-PAWR system, ground-based observation procedures, and system characteristics; Chapter 5 illustrates the data evaluation methodologies and statistical measures used for the comparison; Chapter 6 presents the case studies, results, and detailed analyses. Finally, Chapter 7 concludes the thesis, summarizing the main findings and discussing their significance.

The EarthCARE mission

The *EarthCARE* (Earth Cloud, Aerosol and Radiation Explorer) satellite, a joint mission of the European Space Agency (ESA) and the Japan Aerospace Exploration Agency (JAXA), aims to observe and characterize the vertical structure of clouds, aerosols, and precipitation. In addition, the mission provides measurements of radiative fluxes and estimates of atmospheric heating rates. As described in [1], EarthCARE delivers global cloud, aerosol, and precipitation profiles alongside collocated radiative flux data, offering essential insights for climate research.

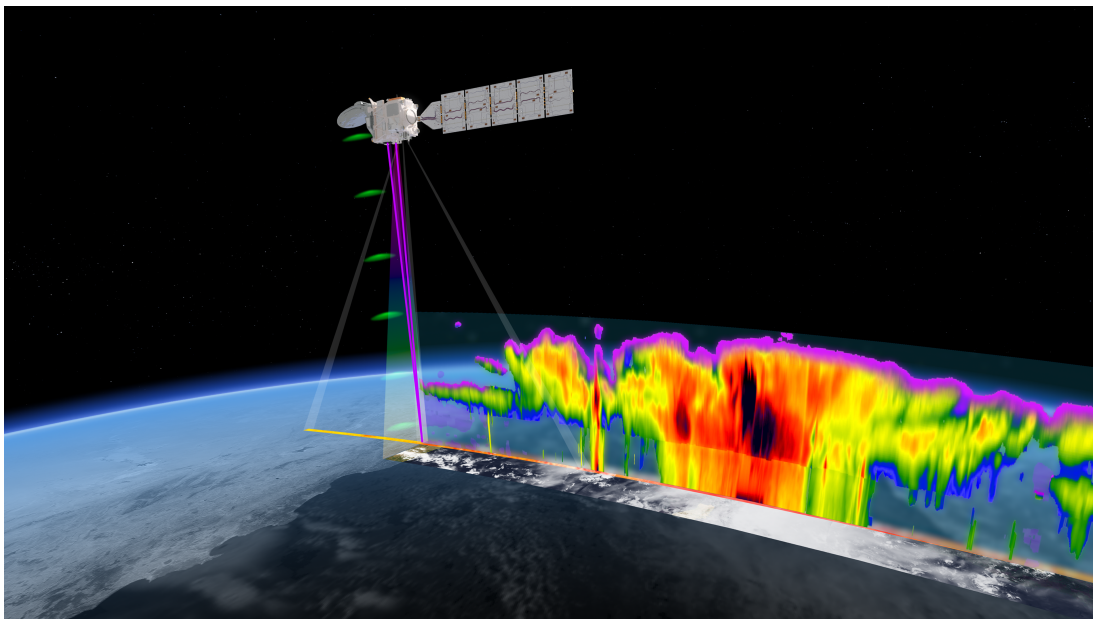

Figure 2.1: Schematic illustration of the EarthCARE satellite. Image: © ESA.

The *EarthCARE* satellite is equipped with four scientific instruments: a Doppler cloud radar, an atmospheric lidar, a multispectral imager, and a broadband radiometer. According to [1], all instruments underwent comprehensive characterization, calibration, testing, and integration before launch.

The lidar, operating at ultraviolet wavelengths, includes a high-spectral-resolution receiver and a depolarization measurement channel. This configuration allows it to capture vertical profiles of aerosols and thin clouds, as well as to discriminate between different aerosol types. The cloud radar, operating at $94\,GHz$ (W-band) with Doppler capabilities, provides measurements of clouds and precipitation. Its penetration depth exceeds that of the lidar, partially overlapping its range while reaching regions where the lidar signal is attenuated.
The multispectral imager has four solar and three thermal channels, enabling across-track observations of clouds and aerosols. It can also be used to reconstruct three-dimensional scenes of clouds, aerosols, and precipitation, supporting radiative transfer calculations.
Finally, the broadband radiometer measures solar and thermal radiances along three fixed viewing directions along the satellite's orbit, allowing precise determination of top-of-atmosphere radiative fluxes.

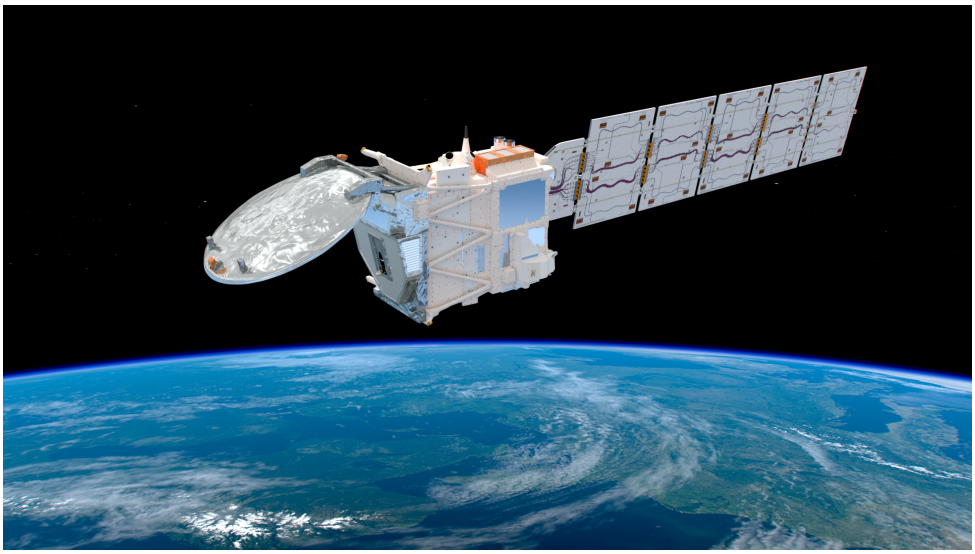

Figure 2.2: EarthCARE over Europe. Image: © ESA.

2.1 Mission science objectives

The EarthCARE mission was first selected in 2000 for a pre-feasibility study, followed by approval of the Phase A study in 2001, and finally greenlit for full implementation in 2004. As noted in [1], the mission's observational strategy is designed to tackle fundamental scientific questions. In particular, EarthCARE aims to provide:

1. vertically resolved profiles of clouds, aerosols, and precipitation along the satellite's nadir path;
2. three-dimensional representations of clouds and aerosols across the satellite track;
3. simultaneous measurements of solar and thermal broadband radiances and fluxes at co-located positions.

Clouds are currently the largest source of uncertainty in global climate models [1]. Aerosol–cloud interactions represent an additional significant challenge: although CMIP6 models incorporate more sophisticated representations of these processes compared to earlier generations, confidence remains only moderate that these improvements translate into more accurate simulations.
To address these challenges, active satellite instruments such as lidar and W-band radar are essential. Key cloud properties relevant for assessing climate feedbacks, such as type, phase, thickness, altitude, and vertical extent cannot be reliably retrieved from passive sensors alone. By integrating active and passive measurements, the EarthCARE mission will generate an unprecedented, long-term observational dataset, crucial for reducing uncertainties in the radiative effects of clouds and aerosols and for improving the accuracy of climate projections.
The mission is designed to provide global observations of the vertical structure of clouds and aerosols, along with radiative measurements [1]. These data will support more realistic representations of clouds and aerosols in both climate and weather models, enhancing the predictive capability of these systems.

2.2 EarthCARE system overview

The EarthCARE satellite is a purpose-built, three-axis stabilized platform constructed from carbon-fibre-reinforced polymer (CFRP), combining low mass with high structural stability. Its streamlined design, featuring a rear-mounted solar panel, minimizes the spacecraft's cross-sectional area and thereby reduces residual atmospheric drag at its relatively low operational altitude of 393 km [1].
This low-altitude orbit was specifically chosen to optimize the performance of EarthCARE's two active instruments: the lidar and the W-band radar. The satellite operates in a sun-synchronous orbit, crossing the equator at the descending node around 14:00 MLST, with an inclination of 97° and a revisit cycle of 25 days, corresponding to 398 orbits.
The spacecraft has a total mass of 2350 kg, which includes 313 kg of hydrazine propellant. This is sufficient to support a nominal mission duration of three years, with an additional one-year propellant reserve.

Parameter	Orbit Value (mean Kepler)
Semi-major axis	$a = 6771.28\,km$
Eccentricity	$e = 0.001283$
Inclination (sun-synchronous)	$i = 97.050°$
Argument of perigee	$\omega = 90°$
Mean Local Solar Time, Descending Node	$MLST = 14:00$
Repeat cycle/ cycle length	25 days, 389 orbits
Orbital duration	$5552.7\,s$
Mean Spherical Altitude	$393.14\,km$
Minimum Geodetic Altitude	$398.4\,km$
Maximum Geodetic Altitude	$426.0\,km$
Average Geodetic Altitude	$408.3\,km$
Dead band	$+/-\ 25\,km\,nominal$, $+/-\ 1\,km$ limited (time & areas)

Table 2.1: EarthCARE Orbit Parameters (Source: [2])

2.3 Satellite instruments

The scientific payload of the EarthCARE satellite consists of four instruments—ATLID, CPR, MSI, and BBR as reported in [1].

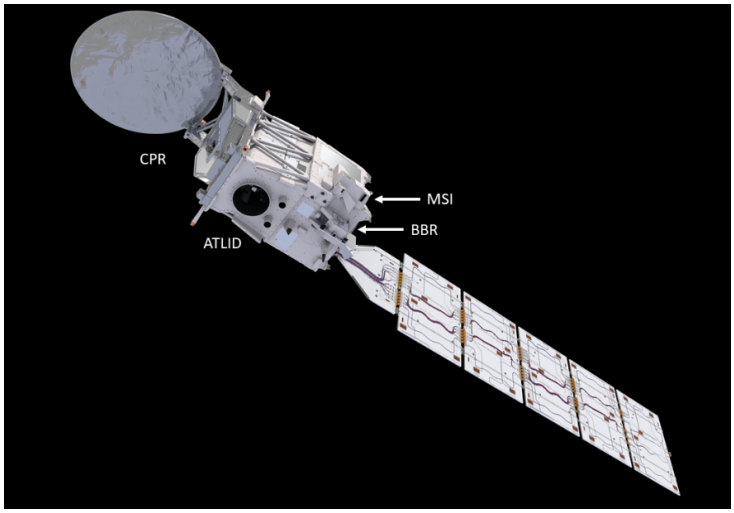

Figure 2.3: Placement of instruments (source: [1]).

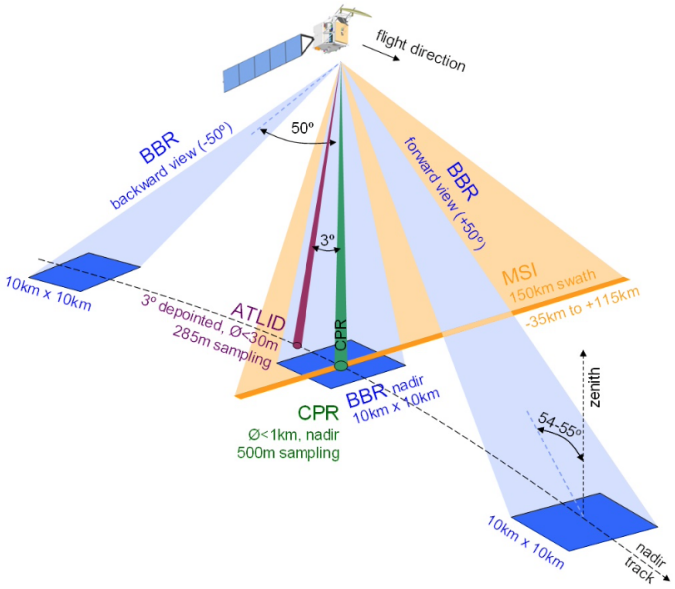

Figure 2.4: Viewing geometry of the instruments. Image: © ESA.

As reported in [2], Figure 2.4 illustrates the instrument viewing geometry. The satellite ground track is shown along with the orientation of each instrument: the CPR beam points at nadir; the ATLID lidar beam is tilted

3° backward to minimize specular reflections; the MSI scans across-track, with an offset in the anti-sun direction to reduce sun-glint[1]; and the three BBR views nadir, forward and backward, are used to retrieve the emitted flux.

2.3.1 The ATLID (Atmospheric LIDar) instrument

The primary goal of ATLID is to measure the vertical distribution of optically thin clouds and aerosols.

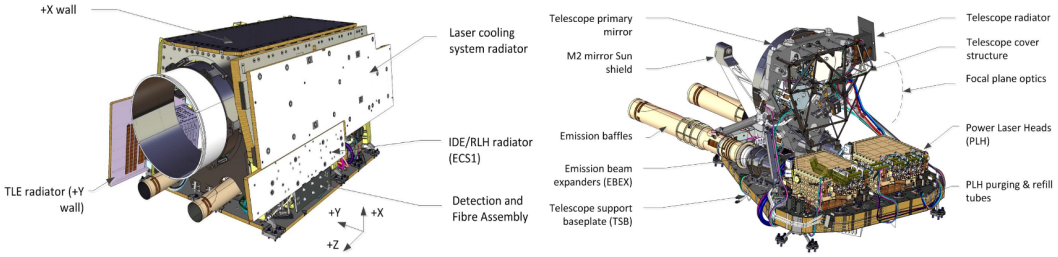

Figure 2.5: ATLID instrument configuration. Image: © ESA.

As reported in [2], ATLID observes the atmosphere in a near-nadir geometry, providing a vertical resolution of about 100 m from the surface up to 20 km, and 500 m between 20 km and 40 km altitude.
The transmitter emits short laser pulses at a repetition rate of 51 Hz, resulting in a horizontal sampling of approximately 140 m along the satellite track. This allows multiple consecutive pulses to be locally averaged, enhancing the signal-to-noise ratio. The ATLID receiver collects the backscattered photons using a telescope with an aperture of roughly 60 cm in diameter.

[1]Sun-glint: an optical effect occurring when sunlight reflects off a smooth water surface directly toward the sensor, producing very bright areas in satellite imagery and potentially affecting measurements of atmospheric or oceanic properties.

Item	Specification
Operating wavelength	354.8 nm
Emitted energy	38 mJ
Receiver footprint diameter	$\leq$ 30 m
PRF	51 Hz
Transmit pulse width	20 ns
Altitude range	-0.5 to +40 km
Vertical sampling interval	100 m
Along track sampling interval	285 m
Dynamic range	10^{-7} to $9.61 \times 10^{-3}\,\mathrm{sr}^{-1}\,\mathrm{m}^{-1}$
Radiometric stability	1%

Table 2.2: ATLID Instrument – Key Specifications (Source: [2])

2.3.2 Broadband radiometer (BBR)

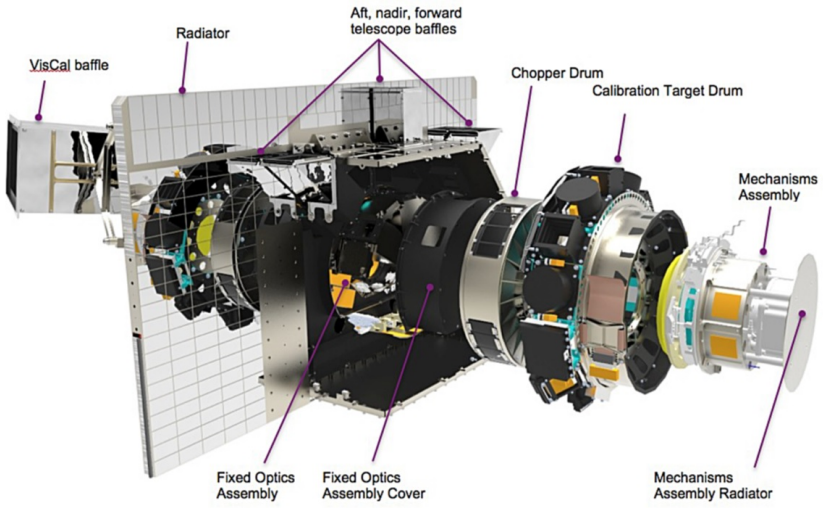

Figure 2.6: Detailed exploded view of the BBR instrument. Image: © ESA.

Covering scenes of roughly 10 km, the BBR instrument provides estimates of both the Earth's thermal emission and the outgoing solar reflected flux. According to [2], its 34 kg Optics Unit (OU) records top-of-atmosphere (TOA) radiance in two spectral bands through three quasi-simultaneous along-track views directed nadir, forward, and backward relative to nadir.

2.3.3 CPR: the Cloud Profiling Radar

The CPR is primarily designed to observe the vertical structure of clouds along the satellite's path, allowing the retrieval of both microphysical and macro-physical cloud properties, as well as the vertical velocities of cloud particles. The instrument was developed under the responsibility of JAXA in Japan.

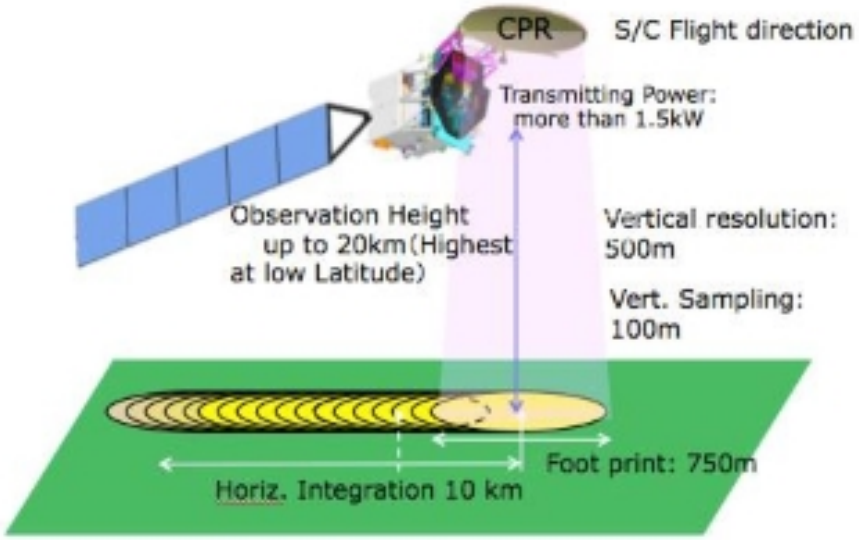

Figure 2.7: CPR measurement principle. Image: © ESA.

As reported in [2], the CPR is a high-power 94 GHz radar developed to provide vertical profiles of clouds along the sub-satellite track. It emits microwave pulses at variable repetition frequencies, which can penetrate lower cloud layers that are not accessible to optical instruments.
The instrument's measurement range spans from roughly -1 km, enabling the use of surface backscatter, up to approximately 20 km in altitude, with a vertical sampling interval of 100 m.

Parameter	Value
Centre frequency	$94.05\,GHz$
Pulse width	$3.3\,\mu s$
Polarisation	Circular
Transmit power	> 1.5
Height range	Up to 20 km (highest at low Latitude)
Vertical resolution	500 m (100 m sampling)
Horizontal resolution	750 m (antenna footprint)
Minimum sensitivity	$-35\,dBZ$
Pulse repetition frequency	Variable in range 6100 to 7500 Hz
Beam width	$0.095°$
Antenna aperture diameter	$2.5\,m$
Pointing accuracy	$< 0.015°$
Doppler range	$\pm 10\,m/s$
Doppler accuracy	$1\,m/s$

Table 2.3: Parameters of the CPR (Source: [2])

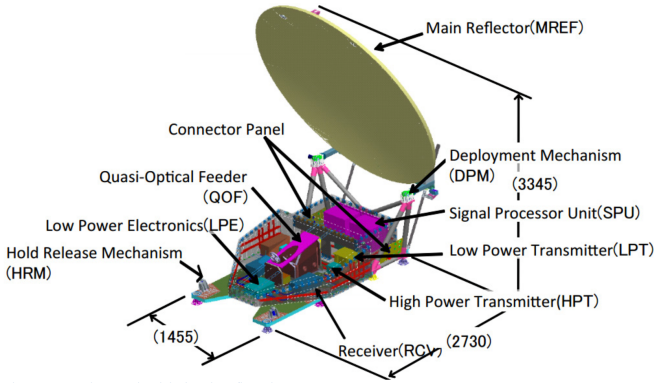

Figure 2.8: CPR in its operational configuration. Image: © ESA.

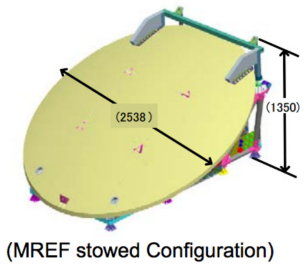

Figure 2.9: Principal Reflector. Image: © ESA.

Figure 2.9 shows the CPR reflector, which has an aperture diameter of 2.5 m, selected to satisfy the radar's performance requirements, including sensitivity, Doppler measurement capability, and field of view.
The Transmit-Receive Subsystem, as detailed in [2], comprises the radar transmitter, its power supply, and the receiver electronics. A quasi-optical feed system both directs the transmitted RF pulses toward the reflector and collects the returning signals for on-board processing. After down-conversion to an intermediate frequency (IF), these signals are transmitted

to the Signal Processing Unit (SPU). In addition to its high sensitivity, the CPR possesses a Doppler measurement capability that allows the determination of vertical velocities of cloud particles.

Calibration Challenges of EarthCARE and the Role of CloudSat Data

The previous NASA mission, CloudSat, with its Cloud Profiling Radar (CPR) operating at 94 GHz and featuring a well-established calibration, provides an invaluable reference for the calibration and validation of the EarthCARE CPR. CloudSat has been used to support the calibration of other airborne and ground-based radars, primarily because its radar is not only accurately calibrated but also offers a long-term, high-quality global dataset, making it ideal for comparative studies [3, 4].
As noted in [3], CloudSat, thanks to its well-characterized and stable calibration, can be used as a global reference to assess and correct the calibration of ground-based and airborne cloud radars, as demonstrated with ARM Barrow, Cabauw, and RASTA data. This capability is rooted in the rigorous pre-launch calibration procedures of CloudSat, which included internal link budgets, comparisons with predicted ocean surface backscatter at 94 GHz, direct measurements against airborne cloud radars, and statistical comparisons with ground-based radars across different sites worldwide.
Consequently, CloudSat provides a reliable and globally consistent reference, allowing the identification of calibration offsets in other radars and supporting the validation of new instruments like the EarthCARE CPR. Its stable calibration and extensive observational record make it a cornerstone for ensuring radiometric consistency across diverse platforms, from ground-based networks to airborne campaigns.
The primary distinction between the CloudSat Cloud Profiling Radar (CAR) and the EarthCARE Cloud Profiling Radar (CPR) is that the latter is capable of measuring Doppler velocity.
It is useful to see the comparative table 2.4 below.

Feature	EarthCARE CPR	CloudSat CPR
Frequency	94 GHz (W-band)	94 GHz (W-band)
Polarization	Single-polarized	Single-polarized
Viewing geometry	Nadir	Nadir
Vertical resolution	∼500 m	∼500 m
Mean Spherical Altitude	393.14 km	705 km
Sensitivity	∼-35 dBZ	∼-28 dBZ
Field of view	Limited to vertical column	Limited to vertical column
Calibration	Pre-launch in laboratory; in-orbit calibration using reference echoes and inter-satellite comparisons	Pre-launch in laboratory; in-orbit calibration using stratiform clouds and model comparisons
Reflectivity accuracy	+0.5–1 dB (good signal)	±1–2 dB (good signal)
Height accuracy	±250 m	±250 m

Table 2.4: Comparison of the main characteristics of the CloudSat CPR and EarthCARE CPR profiling radars.

Challenges and Mitigation of the EarthCARE CPR

The EarthCARE Cloud Profiling Radar (CPR) represents a significant advancement in spaceborne cloud and precipitation observation, providing high-sensitivity measurements in the W-band and the capability to retrieve Doppler velocity. However, several challenges inherent to this instrument must be carefully addressed to fully exploit its scientific potential. Strong attenuation at 94 GHz, particularly in heavy precipitation or dense cloud layers, can markedly reduce the radar return signal. Multiple scattering effects from ice crystals and large hydrometeors further complicate the retrieval of reflectivity [5, 6]. Moreover, the CPR exhibits reduced sensitivity to low-altitude clouds and a limited vertical resolution of approximately 500

m, which may impede the detection of thin or shallow cloud layers [7]. The instrument's geolocation accuracy has been confirmed to be on the order of 100 metres [8]. Its small antenna footprint and nadir-only pointing further constrain spatial coverage. Doppler velocity measurements introduce additional complexities, such as velocity aliasing [9], and require precise correction for platform motion, non-uniform beam filling [10], and antenna mis-pointing [11, 6]. A major source of uncertainty in CPR observations is the presence of multiple scattering (MS). When the radar beam propagates through optically thick clouds or intense precipitation, the returned signal may include contributions from photons that have undergone more than one scattering event before reaching the sensor. This violates the single-scattering assumption used in standard retrieval algorithms, leading to an artificial enhancement of apparent reflectivity. In deep ice clouds, MS can partially compensate for attenuation, making the cloud appear less attenuating than it actually is, whereas in rain or mixed-phase conditions it may introduce strong biases in both reflectivity and extinction retrievals. As MS becomes significant for optical depths greater than approximately three, its presence must be carefully accounted for in data interpretation and in higher-level product generation. For example, regarding the mis-pointing problem, even small deviations in the nadir-pointing direction of the CPR can introduce significant errors in observed Doppler velocities and in the vertical location of cloud layers. According to [8], at a satellite altitude of $393.14\,\mathrm{km}$, a mis-pointing error of 0.01° corresponds to a geolocation error of approximately $69\,\mathrm{m}$. Considering the satellite velocity of $7.6\,\mathrm{km/s}$, a minimal mis-pointing error of 0.01° along the along-track direction translates into a Doppler velocity bias of about $1.33\,\mathrm{m/s}$. From June to November 2024, a pointing correction was performed, allowing CPR data to be corrected to within 5–$7\,\mathrm{cm/s}$, significantly reducing Doppler velocity biases.

For calibration, an external method was applied, as reported in [12]. The study shows that the absolute calibration uncertainty of the W-band radar is expected to be less than 1 dB, approximately 0.5–1 dB. Residual calibration errors can bias cloud reflectivity estimates, particularly for weakly scattering clouds or snow, and propagate into derived microphysical and precipitation products. Other remaining issues include reduced sensitivity to low-altitude clouds, strong attenuation in heavy precipitation, and limited vertical resolution. These limitations can be assessed and partially validated through comparisons with ground-based radar measurements,

providing a benchmark for the quality of CPR data and derived products. Despite these challenges, the combination of high sensitivity, Doppler capability, and rigorous calibration makes EarthCARE CPR uniquely capable of providing unprecedented insights into cloud microphysics, precipitation processes [13, 5], and vertical air motion. Continued development and validation of correction algorithms, together with careful assessment of remaining uncertainties, are crucial to fully exploit the radar's potential for both weather and climate research.
In conclusion, while CPR data require careful processing and calibration, the adopted strategies and ongoing validation efforts are expected to deliver high-quality products that significantly advance our understanding of cloud and precipitation dynamics from space.

2.3.4 MSI: the Multi-Spectral Imager

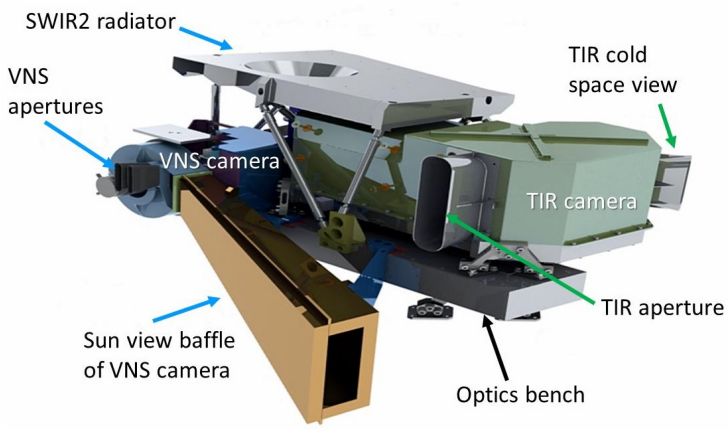

Figure 2.10: MSI Optical Bench Assembly. Image: © ESA.

According to [2], the MSI is a push-broom scanner operating in seven spectral bands, capable of acquiring images with a ground sampling distance of 500 m over a swath of 150 km. The swath is offset from nadir, extending from –35 to +115 km, in order to minimize sun-glint effects.
The acquired imagery provides contextual information for the quasi-simultaneous along-track measurements of the CPR and ATLID instruments, while also supplying additional data on cloud properties such as cloud type, texture, cloud-top temperature, and microphysical characteristics, including phase.

2.4 Processing chains

As reported in [14], instrument data are downlinked via the satellite's X-band antenna as Instrument Source Packets (ISPs). These packets are received by the ESA Payload Data Ground Segment (PDGS), where they are first organized into a continuous, time-ordered sequence. For each instrument, this produces a dedicated level 0 product, augmented with ancillary information.
Level 0 products are then processed by the EarthCARE Ground Processors (ECGPs) to generate level 1b data, which consist of fully calibrated and geolocated measurements. CPR, ATLID, and MSI data are provided on the instruments' native grids, while BBR data are delivered as a single-pixel product.
Level 1 products for ATLID, MSI, and BBR are generated within the ESA PDGS and subsequently transferred to the JAXA ground segment. In contrast, CPR follows a slightly different workflow: its level 0 data are first sent from ESA to JAXA, where level 1 products are created and returned to ESA. After level 1 processing, all four instruments have their products available at both ground segments, ready for the respective level 2 processing chains.
Finally, level 2 products are exchanged between ESA and JAXA, ensuring that the full set of EarthCARE data is accessible to end users from either agency, independent of where the processing was performed.

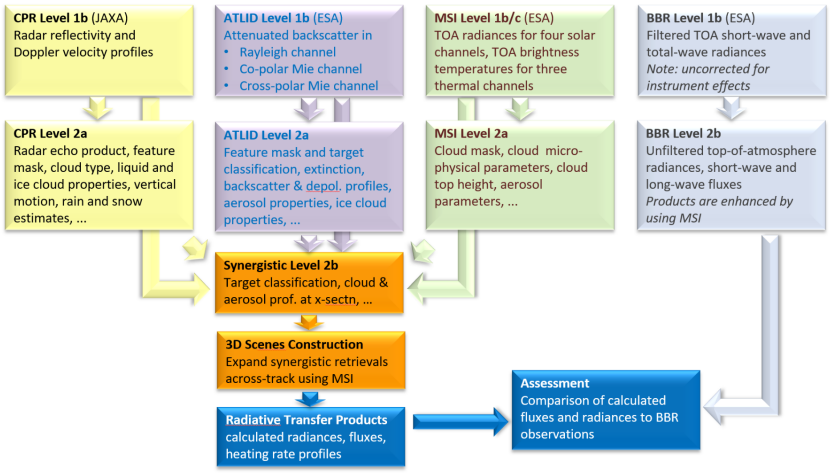

Figure 2.11: Overview of the EarthCARE data processing chain (source: [14]).

Figure 2.11, based on [14], presents the EarthCARE data processing workflow. Starting from the level 1 products, each instrument generates its own level 2a outputs, which are then combined to produce the level 2b products, integrating measurements from multiple sensors.

2.5 Conventions and format of the products

2.5.1 Product conventions

As described in [14], ESA products and processors use a naming convention consisting of two parts separated by a hyphen: a code of up to four letters (XXXX) identifying the instrument, and up to three letters (YYY) indicating the product type, resulting in the format XXXX-YYY. For most ESA products, XXXX corresponds to one or more of the four EarthCARE instruments (A = ATLID, C = CPR, M = MSI, B = BBR).
JAXA data products, in contrast, are labelled with two parts separated by an underscore (e.g., CPR_CLP). The first two or three characters denote the instrument(s) involved (CPR = CPR, ATL = ATLID, MSI = MSI, AC = ATLID–CPR, ACM = ATLID–CPR–MSI, AM = ATLID–MSI, ALL = all four instruments), while the final three characters indicate the geophysical content of the product, such as CLP for cloud properties or RAD for radiation.

2.5.2 Product format

As reported in [14], EarthCARE Level 1 and Level 2 data products are provided in NetCDF-4/HDF5 format. This format was selected due to its widespread use in the scientific community and its support for self-describing datasets. Each product is internally compressed and corresponds to a single frame, covering roughly 1/8 of an orbit, or about 5000 km along the satellite path.

Fundamentals of Radar Systems

3.1 Reflectivity(η), Reflectivity Factor(Z)

The radar reflectivity factor describes a characteristic of the hydrometeors contained within the radar's sampling volume. In practice, however, the radar retrieves only an approximation of this quantity. The estimated value may fluctuate due to several influences, including calibration uncertainties, limited sampling duration, and attenuation of the transmitted signal as it travels through the atmosphere and precipitation.
As stated by [15], the radar reflectivity factor (Z) is defined as

$$Z = \frac{\sum_n D_n^6}{V}, \tag{3.1}$$

where D represents the equivolume diameter of a raindrop, and the summation extends over all drops contained within a volume V. The reflectivity factor is typically expressed in units of $mm^6\, m^{-3}$. As further discussed in [15], it is often converted to a logarithmic scale and expressed in decibels (dBZ):

$$Z(dBZ) = 10 \log_{10}(Z). \tag{3.2}$$

The radar reflectivity ($\overline{\eta}$), on the other hand, is defined as the mean radar cross section (RCS), σ, per unit volume. In simple terms, the RCS of a target describes how large the object appears to the radar in an electromagnetic sense. Therefore, the radar reflectivity represents the average RCS per unit volume for all scatterers within V:

$$\overline{\eta} = \frac{\sum_{n=1}^{N} \sigma_n}{V}. \tag{3.3}$$

For additional details, the reader is referred to [15].

3.2 Observation Geometry

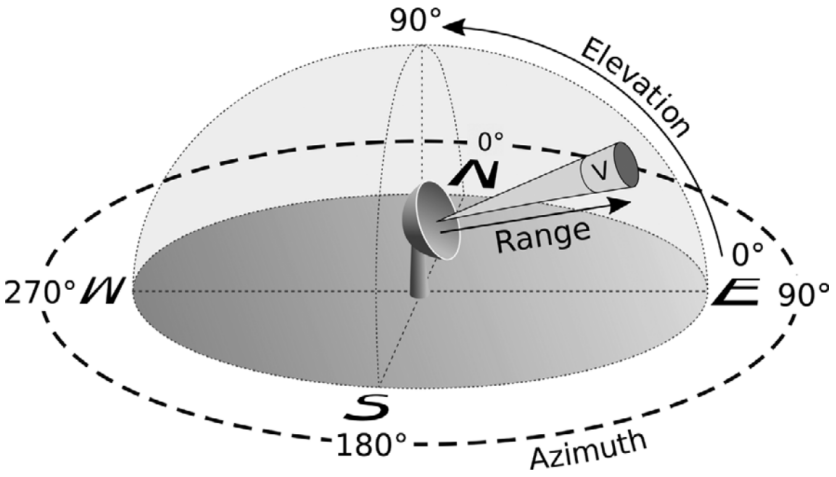

Figure 3.1: the spherical scanning geometry of the radar (source: [15])

Radar observations are most conveniently described using a modified spherical coordinate system, defined by range (r), azimuth (ϕ), and elevation (θ). In this framework, the radar is positioned at the origin and performs outward scanning. As noted in [15], scanning radar systems are capable of steering their beam in both azimuthal and elevational directions. The transmitted signal propagates radially from the antenna, and the backscattered echoes from precipitation are received along the same radial paths. In the Cartesian coordinate system, aligned with cardinal directions, the following conventions are adopted:

- The positive x-axis points east, while the negative x-axis points west.
- The positive y-axis points north, and the negative y-axis points south.
- The positive z-axis corresponds to the zenith, whereas the negative z-axis corresponds to the nadir, which is generally not relevant for ground-based radar systems.

As described in [15], the radar azimuth angle ϕ is defined such that 0° points north and increases clockwise, passing through east ($\phi = 90°$), south ($\phi = 180°$), and west ($\phi = 270°$). The elevation angle θ is measured from the horizontal plane (0°) and increases toward the zenith (90°).

Conversion from spherical to Cartesian coordinates, often required for further processing or visualization, is expressed as follows:

$$\begin{bmatrix} x \\ y \\ z \end{bmatrix} = \begin{bmatrix} r\cos\left(\frac{\pi}{2} - \phi\right)\cos(\theta) \\ r\sin\left(\frac{\pi}{2} - \phi\right)\cos(\theta) \\ r\sin(\theta) \end{bmatrix} \tag{3.4}$$

In this coordinate system, the zenith is aligned with $+z$, while the cardinal directions correspond as follows: west to $-x$, east to $+x$, south to $-y$, and north to $+y$. As discussed in [15], for short-range radar observations, the Earth's surface can be approximated as flat without introducing significant errors. However, at longer ranges, neglecting the Earth's curvature and the effects of atmospheric refraction may lead to considerable inaccuracies when estimating the altitude above the surface.
To estimate the radar beam height more accurately, it is common to adopt a modified Earth radius, allowing the propagation path to be treated as approximately straight, as illustrated in Figure 3.2.

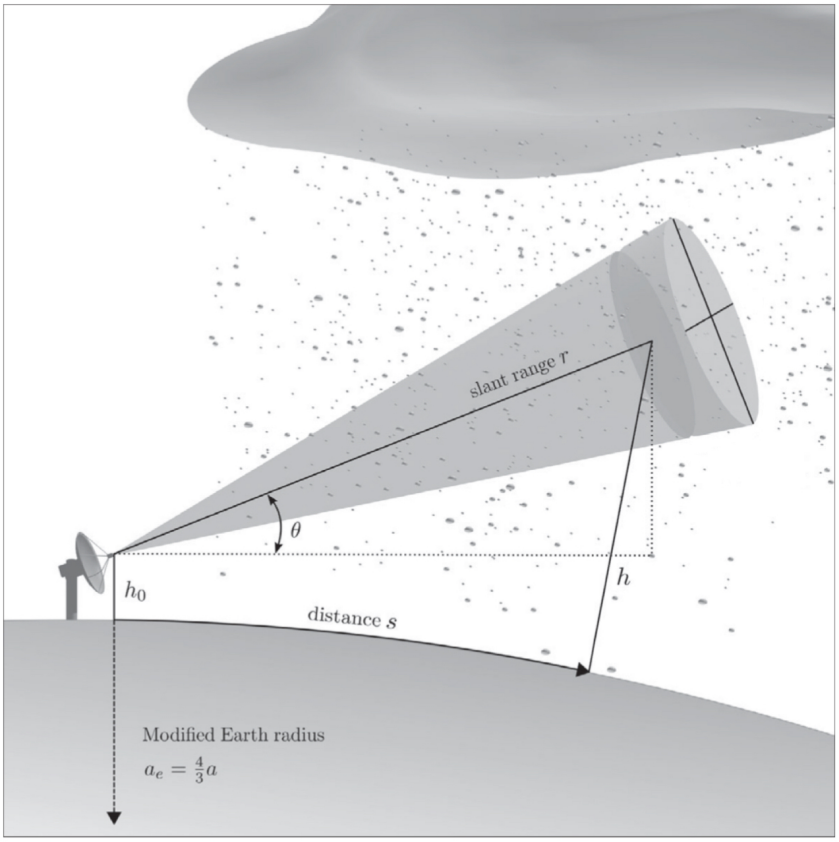

Figure 3.2: Illustration of the propagation path and radar resolution volume (source: [15])

According to [15], the Earth exhibits a slight oblateness, with its radius varying from roughly 6357 km at the poles to 6378 km at the equator. For simplicity, radar studies often adopt a spherical Earth approximation with a nominal radius of $a = 6371$ km. To incorporate the effects of atmospheric refraction, an effective Earth radius is frequently introduced, defined as $a_e = \frac{4}{3}a$.
When assuming a standard atmospheric profile, the altitude of the radar beam above the Earth's surface can then be determined as:

$$h(r, \theta) = h_0 + \sqrt{r^2 + a_e^2 + 2ra_e \sin\theta} - a_e, \tag{3.5}$$

where h_0 denotes the height of the radar antenna above the ground. The corresponding great-circle distance along the Earth's surface can be expressed as:

$$s(h, \theta) = a_e \arcsin\left(\frac{r\cos\theta}{a_e + h}\right). \tag{3.6}$$

Following [15], the radar beam's ground-relative Cartesian coordinates and height above a spherical Earth may be approximated by:

$$\begin{bmatrix} x_E \\ y_E \\ z_E \end{bmatrix} = \begin{bmatrix} \cos\left(\frac{\pi}{2} - \phi\right) a_e \arcsin\left(\frac{r\cos\theta}{a_e+h}\right) \\ \sin\left(\frac{\pi}{2} - \phi\right) a_e \arcsin\left(\frac{r\cos\theta}{a_e+h}\right) \\ h_0 + \sqrt{r^2 + a_e^2 + 2ra_e\sin\theta} - a_e \end{bmatrix}. \tag{3.7}$$

3.3 Radar Equation

As presented in [15], the radar equation establishes a quantitative link between the power transmitted by the radar and the power received after reflection from a target. This equation is a fundamental tool for assessing radar performance and system sensitivity.
The characteristics of a target, including its size and ability to reflect electromagnetic waves, are quantified by the Radar Cross-Section (RCS). The RCS measures the fraction of incident power that is scattered back toward the radar. Mathematically, it is expressed as:

$$\sigma = \lim_{r\to\infty} 4\pi r^2 \frac{S_s}{S_i}, \tag{3.8}$$

where r denotes the separation between the radar and the target, and S_i and S_s represent the incident and scattered power densities, respectively.

3.3.1 Single-Target Radar Equation

The single-target radar equation allows the calculation of the power returned to the radar from a target with a known RCS.
As reported in [15], for a transmitted power P_t, the incident power density on the target, assuming a directional rather than an isotropic antenna, can be expressed as:

$$S_i = \frac{P_t G_t}{4\pi r_t^2}, \tag{3.9}$$

here, G_t denotes the gain of the transmitting antenna, while the term $1/(4\pi r_t^2)$ corresponds to the surface area of a sphere with radius r_t.
Consequently, the total power scattered by the target can be expressed as:

$$P_s = S_i \sigma = \frac{P_t G_t \sigma}{4\pi r_t^2}, \tag{3.10}$$

where P_s is expressed in watts. The power density of the scattered wave at the radar receiver, situated at a distance r_r from the target, can then be written as:

$$S_r = \frac{P_s}{4\pi r_r^2} = \frac{P_t G_t \sigma}{(4\pi)^2 r_t^2 r_r^2}. \tag{3.11}$$

The received power can then be determined by multiplying the power density S_r by the effective area of the receiving antenna, A_e, resulting in:

$$P_r = S_r A_e = \frac{P_t G_t \sigma A_e}{(4\pi)^2 r_t^2 r_r^2}. \tag{3.12}$$

The gain of the antenna and its effective area are related by:

$$G_r = \frac{4\pi A_e}{\lambda^2}, \tag{3.13}$$

where λ denotes the wavelength of the transmitted signal. By substituting this relation into equation (3.12), one obtains the general radar equation for a point target:

$$P_r = \frac{P_t G_t G_r \lambda^2 \sigma}{(4\pi)^3 r_t^2 r_r^2}. \tag{3.14}$$

For a monostatic radar, where the same antenna is employed for both transmission and reception ($G_t = G_r = G$ and $r_t = r_r = r$), the equation reduces to the familiar form:

$$P_r = \frac{P_t G^2 \lambda^2 \sigma}{(4\pi)^3 r^4}. \tag{3.15}$$

As highlighted [15], radar power levels are commonly expressed on a logarithmic scale, using units of dBm or dBW.

3.4 Electromagnetic Scattering Principles for Meteorological Radar

According to [15], the interaction between radar waves and precipitation is governed by the principles of electromagnetic scattering. The scattering behavior depends strongly on the microphysical attributes of individual hydrometeors, such as their size, shape, and orientation, which determine how the incident energy is redistributed. Specifically, part of the transmitted energy is redirected toward the radar (backscattering), part is scattered in other directions, and part is absorbed by the particles. These mechanisms are described by the backscattering, total scattering, and extinction cross-sections, respectively.

To make the analysis more tractable, hydrometeors are typically idealized as geometrically simple bodies, for example, spheres or spheroids, which enable an analytical link between particle geometry and electromagnetic response. The deployment of dual-polarization and multi-frequency radar systems enhances the measurement capability by providing independent observations that improve the retrieval of microphysical parameters, such as the median drop diameter and precipitation rate.

As described in [15], radar observations can therefore be interpreted in terms of scattering characteristics within the sampled volume. In this context, the extinction cross-section (σ_e) represents the portion of the incident wave energy that is removed from the propagation path, either through absorption or through scattering away from the direction of incidence. This

relationship is expressed as:

$$\sigma_e = \sigma_a + \sigma_s, \tag{3.16}$$

where σ_a is the absorption cross-section, accounting for the conversion of electromagnetic energy into heat, and σ_s is the total scattering cross-section, representing energy re-radiated in all directions.

3.4.1 Scattering Phenomena in Spheres

To characterize the scattering behaviour of a general target, it is necessary to determine the far-field amplitude vector $\mathbf{s}(\hat{s}, \hat{i})$, which describes how an electromagnetic wave incident from direction $\hat{i}$ is scattered toward direction $\hat{s}$ [15].
For a general bistatic radar configuration, the radar cross-section (RCS) quantifies the strength of the scattered field observed in a given direction relative to the incident power. It is defined as

$$\sigma_{bi}(\hat{s}, \hat{i}) = 4\pi \left|\mathbf{s}(\hat{s}, \hat{i})\right|^2. \tag{3.17}$$

A specific case of interest is the backscattering cross-section, which corresponds to the situation in which the scattered wave propagates directly back toward the radar, that is, when $\hat{s} = -\hat{i}$:

$$\sigma_b = 4\pi \left|\mathbf{s}(-\hat{i}, \hat{i})\right|^2. \tag{3.18}$$

The total scattering cross-section represents the total amount of power scattered into all possible directions and can be computed by integrating over the entire solid angle:

$$\sigma_s = \int_{4\pi} \left|\mathbf{s}(\hat{s}(\Omega), \hat{i})\right|^2 d\Omega, \tag{3.19}$$

where the incident direction $\hat{i}$ remains fixed while the scattering direction $\hat{s}$ varies over the solid angle Ω.
Finally, the extinction cross-section quantifies the loss of power in the forward direction due to both scattering and absorption processes. It is given by

$$\sigma_e = -\frac{4\pi}{k_0} \operatorname{Im}\Big[\mathbf{s}(\hat{i}, \hat{i})\Big], \tag{3.20}$$

where k_0 denotes the free-space wavenumber.
This parameter quantifies the attenuation of the incident wave intensity in the forward direction, reflecting the combined effects of both scattering and absorption phenomena. As highlighted in [15], electromagnetic scattering by spherical (or spheroidal) particles can be classified into three distinct regimes Rayleigh, Mie, and optical depending on the ratio between the particle size and the wavelength of the incident radiation.
The scattering cross-section is typically expressed as a function of the size parameter, defined as

$$k_0 a = \frac{2\pi a}{\lambda}, \tag{3.21}$$

where $a = D/2$ denotes the particle radius.

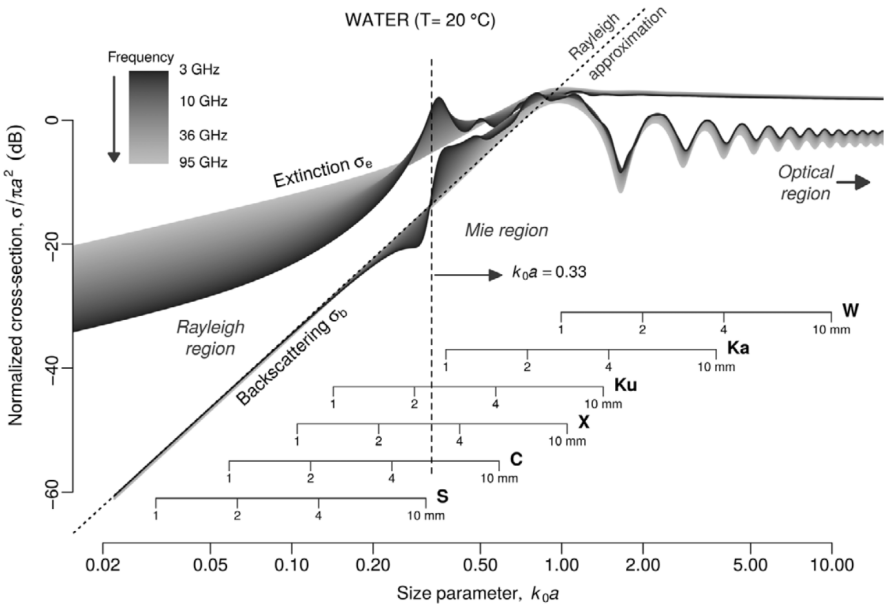

Figure 3.3: Normalized values of the backscattering and extinction cross sections (source: [15])

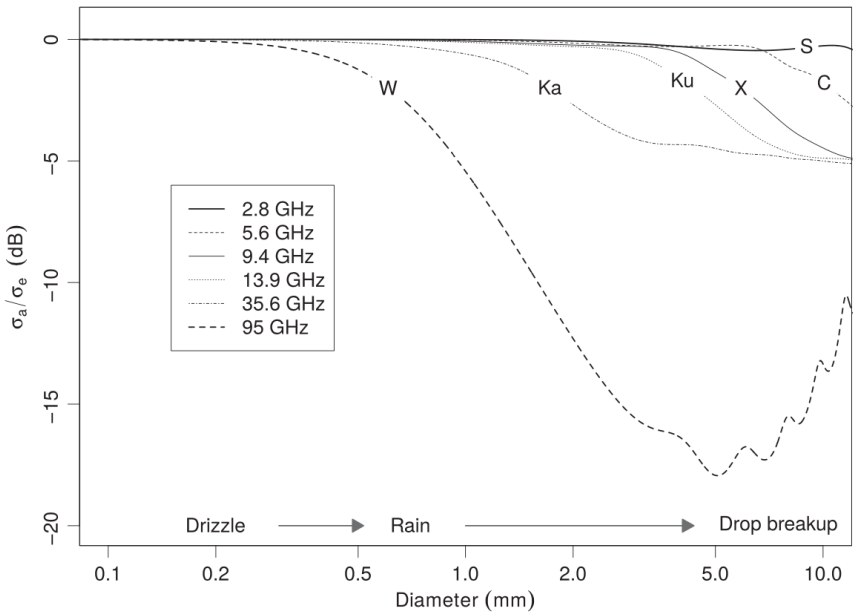

Figure 3.4: Proportion of the extinction cross-section arising from absorption (source: [15])

The scattering behaviour of hydrometeors is governed by the interplay between the radar signal frequency and the particle size. When the particle diameter is much smaller than the radar wavelength, scattering occurs in the Rayleigh regime, leading to minimal energy loss and low attenuation. As the particle size approaches or exceeds the wavelength, scattering transitions into the Mie or optical regimes, where interactions become stronger and geometrically more complex. Comprehensive discussions of these scattering regimes and their effects can be found in [15, 16].

3.5 Multiple Scattering

Multiple scattering (MS) occurs when a radar-emitted electromagnetic wave undergoes several interactions with cloud or precipitation particles before returning to the sensor. This section reviews the MS phenomenon, its impact on EarthCARE CPR observations, and the circumstances in which it becomes particularly relevant.
In single scattering, the radar signal is assumed to undergo only one backscattering event from particles in the medium, as described in [17], and can be expressed by the following relation:

$$\beta_{\text{app}}(r) = \beta_{\text{eff}}(r)e^{-2\tau(r)}, \tag{3.22}$$

where β_{app} is the apparent backscatter, β_{eff} is the intrinsic backscatter, $\tau(r)$ is the optical depth along the path.
The optical depth (τ) is a dimensionless quantity that measures the attenuation or scattering experienced by an electromagnetic wave as it propagates through a medium. It is defined as

$$\tau(r) = \int_0^r \sigma_e(s)\, ds, \tag{3.23}$$

where r is the distance along the propagation path, and $\sigma_e(s)$ is the extinction coefficient (including both scattering and absorption) of the medium. Physically, $\tau = 0$ corresponds to a completely transparent medium, $\tau \ll 1$ indicates negligible attenuation, while $\tau \gtrsim 1$ implies significant signal reduction.
In dense clouds or heavy precipitation, photons may undergo multiple scattering events, resulting in a contribution to the received signal that is not accounted for in standard retrieval algorithms. This violates the single-scattering assumption and introduces biases in derived quantities such as reflectivity, extinction, and Doppler velocity. In fact, in equation (3.22), this additional contribution is represented by $\beta_{\text{MS}}(r)$, which accounts for the effect of multiple scattering.
Multiple scattering can significantly impact EarthCARE CPR observations in several ways. First, it can lead to an artificial enhancement of reflectivity, causing clouds or precipitation to appear more reflective than they actually are [18, 19]. Second, Doppler velocity measurements may be biased, particularly in deep convective ice clouds, due to the additional scattering events [20]. Third, in thick ice clouds, multiple scattering can partially compensate for signal loss caused by absorption or single-scattering attenuation, which may result in an underestimation of the cloud optical depth. Finally, derived microphysical products such as ice water content, precipitation rate, and extinction can be substantially affected if multiple scattering is not properly accounted for.
The significance of multiple scattering depends on the atmospheric conditions. It becomes particularly important in optically thick clouds or heavy precipitation. Deep convective ice clouds, intense rainfall, or the presence of large hydrometeors such as hail are also conditions that enhance multiple

scattering. Additionally, thick ice layers in the upper troposphere can contribute to the effect, making it a key factor to consider when interpreting CPR measurements and retrieving cloud and precipitation properties.

3.5.1 Multiple Scattering Detection in EarthCARE CPR Data

As described in [17, 7], multiple scattering (MS) can have a substantial effect on observations from the Cloud Profiling Radar (CPR). To identify the presence of MS, the procedure begins by taking the observed radar reflectivity profile, Z_{OBS}, as input. A cumulative integral of the radar echo is then calculated from the top of the atmosphere (TOA) downward, considering only the layers where the reflectivity exceeds a threshold value, Z_{thres}. For convective profiles in EarthCARE CPR, this threshold was determined to be $Z_{\text{thres}} = 12$ dBZ. The cumulative integral is expressed as

$$I(z) = \int_{\text{TOA}}^{z} Z_{\text{OBS}}(z')\, dz', \quad \text{for } Z_{\text{OBS}}(z') > Z_{\text{thres}}, \tag{3.24}$$

which quantifies the accumulated backscatter from the higher-reflectivity layers and serves as a basis for identifying the regions affected by multiple scattering.

If the cumulative integral $C(z)$ exceeds a threshold value of 41 dB, then all radar observations below that height are considered to be significantly contaminated by multiple scattering. Above this height, multiple scattering may still be present, but its effect on the CPR observations is considered negligible.

To limit the effects of multiple scattering (MS), EarthCARE CPR processing uses MS-aware retrieval algorithms, marks areas where optical depth and reflectivity indicate strong MS, and combines radar with ATLID lidar to better define cloud boundaries. This approach improves the accuracy of cloud microphysical estimates, even in conditions with significant multiple scattering.

Multi-Parameter Phased Array Weather Radar (MP-PAWR)

4.1 Motivation for Ground-Based Validation

Since the early days of space-based observations, satellites have played a central role in monitoring the global distribution of clouds and precipitation. This capability is particularly valuable over oceans and remote land areas, where the deployment of ground-based instruments is often impractical [21]. Nevertheless, such measurements provide only limited insight into the vertical distribution of hydrometeors within the atmospheric column.
Despite their many advantages, spaceborne radars have inherent limitations. A major challenge for EarthCARE concerns the capability of the Cloud Profiling Radar (CPR) to accurately sample cloud structures in the lowest part of the atmosphere. The instrument's limited vertical resolution, combined with its near-surface blind zone, hampers the detection of shallow cloud layers and prevents a precise identification of cloud-base height. Moreover, attenuation caused by precipitation or dense hydrometeor regions further weakens the radar return, reducing sensitivity to weakly reflective targets such as thin boundary-layer clouds. As a result, CPR measurements become less reliable close to the surface, where accurate cloud profiling is most critical for radiative flux retrievals.

4.2 Multi-Parameter Phased Array Weather Radar (MP-PAWR) description

In recent years, phased array weather radar technology has undergone significant advancements. As reported in [22], dual-polarization radars are among the key radar types developed using phased array techniques.

A major advantage of these systems is their ability to perform both one-dimensional and two-dimensional electronic scanning, made possible by the flexibility of phased array antennas.
Specifically, the X-band PAWR (Phased Array Weather Radar) emits a fan-shaped beam and receives signals through a 128-element receiving array. By employing advanced digital beamforming techniques, it achieves high vertical resolution, greatly enhancing the precision of atmospheric measurements.

Figure 4.1: Radar system with antenna (source: [23])

Figure 4.2: MP-PAWR radome installed in Saitama University (source: [23])

The MP-PAWR represents an advanced dual-polarization version of the original PAWR radar. As described in [22], the system replaces the traditional one-dimensional slotted waveguide antenna with a two-dimensional patch array. This upgrade enables the MP-PAWR to perform electronic elevation scanning while simultaneously acquiring dual-polarization measurements. Figure 4.2 illustrates the MP-PAWR as installed at Saitama University, where it has been operational since late 2017.
According to [22], the MP-PAWR is capable of conducting dual-polarization observations within an 80 km radius and up to 15 km in altitude in as little as 30 seconds. This is achieved by combining electronic vertical scanning, which covers elevation angles from 0 to 90°, with mechanical rotation in azimuth, spanning 0 to 360°.

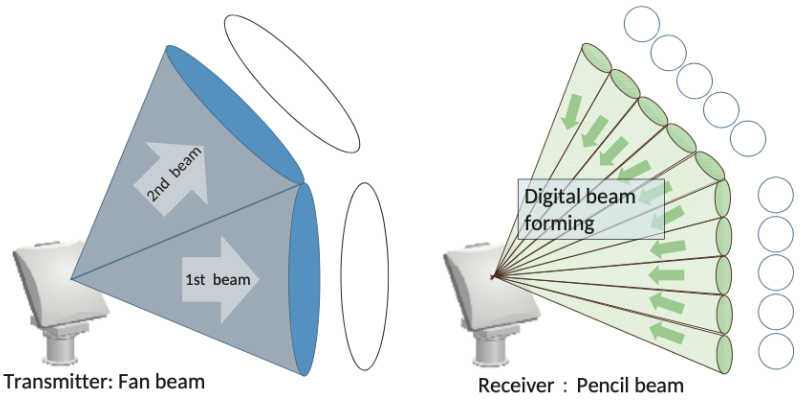

Figure 4.3: Schematic illustration of MP-MPAWR observation in the vertical (elevational) direction (source: [24])

While a conventional operational X-band radar with a parabolic antenna typically scans around 15 elevation angles over a period of roughly 5 minutes, the MP-PAWR can perform a full three-dimensional scan approximately ten times faster, spanning the entire 0–90° elevation range. This capability makes it particularly effective for monitoring rapidly developing and potentially hazardous convective systems. Consequently, the data rate produced by the MP-PAWR is nearly two orders of magnitude higher than that of standard operational radars. Its extremely fast 3D acquisition makes the system especially well-suited for observing cumulonimbus clouds, which evolve quickly and can reach altitudes close to the tropopause.

4.3 MP-PAWR Data Observation and Analysis Methodology

The MP-PAWR is an X-band radar capable of simultaneously transmitting and receiving signals in both horizontal and vertical polarizations. As reported in [22], the system utilizes fan-beam transmissions with an approximate beamwidth of 6°, paired with pencil-beam receptions. This arrangement allows fully electronic RHI scanning over elevation angles from 0° to 90° in about 0.1 s, while azimuthal coverage is obtained through mechanical rotation of the antenna. Under these operational conditions, volumetric measurements can be acquired up to 15 km in altitude and within a 60–80 km range in just 30 s, without any data gaps.
The primary radar observables provided by the MP-PAWR include reflectivity (Z), Doppler velocity, differential reflectivity (Z_{dr}), differential phase

(ϕ_{DP}) between the two polarizations, and the copolar correlation coefficient (ρ_{hv}).

4.4 Description of the MP-PAWR System

The MP-PAWR is installed at Osaka University, located at $Lat = 34.823256°$ and $Long = 135.52278099°$, with an elevation of $148.32\,m$ above sea level.

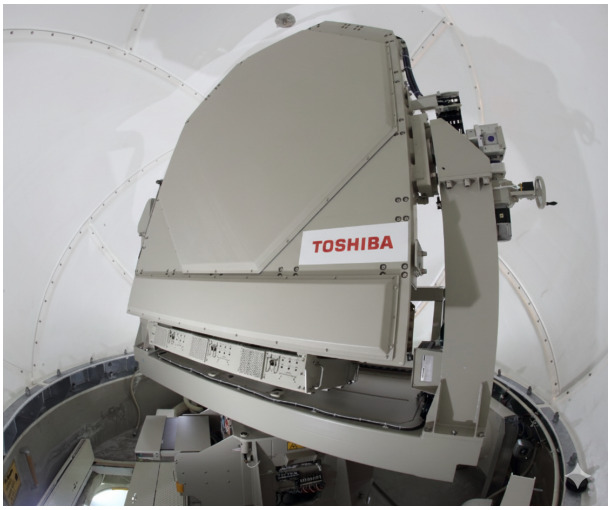

Figure 4.4: MP-PAWR at Osaka University (source: [25])

Figure 4.4 shows an external view of the MP-PAWR. The radar operates in the X-band at a frequency of 9.71 GHz and is equipped with a two-dimensional dual-polarization patch antenna. Signals from the patch antenna are summed along the horizontal axis, effectively making the MP-PAWR a one-dimensional phased-array system in elevation, similar to the original PAWR. According to [22], the antenna array consists of 12 transmitting and 112 receiving elements along the vertical direction.
For transmission, multiple fan-shaped beams with widths ranging from 6° to 27° cover the entire elevation range from 0° to 90°. On reception, digital beamforming is applied to generate 113 narrow beams with beamwidths smaller than 1°. The antenna achieves a sidelobe level of approximately 25 dB, and Moving Target Indicator (MTI) processing is used to suppress ground clutter [22].
In azimuth, mechanical scanning is performed with an angular increment of 1.2°, providing a range resolution of 150 m. Overall, the MP-PAWR can

observe targets within an 80 km radius with a temporal resolution of 30 s, enabling rapid three-dimensional volumetric data acquisition.

Parameter	Value
Operating Frequency	9.71 GHz (X-band)
Transmission Power	4.8 kW (SHV/max.)
Reception Antennas	112 groups / 5920 total elements
Transmit Gain	32 dBi (max.)
Receive Gain	41 dBi (max.)
Antenna Rotation Speed	1/2 rpm
Bandwidth	1.63 MHz
Range resolution	150 m
Azimuth resolution	1.2°
Elevation resolution	0.8°

Table 4.1: Technical specifications of the MP-PAWR at Osaka University (Suita) (Source: [25])

Moreover, according to [24], the MP-PAWR is capable of observing the evolution of cumulonimbus clouds, the creation of hydrometeors, and their subsequent descent as precipitation.

4.5 Moving Target Indicator (MTI) processing

Moving Target Indicator (MTI) processing is applied to MP-PAWR data to reduce ground clutter. Although the MP-PAWR is primarily a weather radar rather than a dedicated MTI system, the filtering operates on the same principles used in conventional MTI radars. To clarify the underlying concept, it is helpful to briefly review how MTI radars function. As explained in [26], an MTI radar is a pulsed system that utilizes the Doppler frequency shift to discriminate moving targets from stationary clutter.

4.5.1 Delay-Line Cancellation Filter

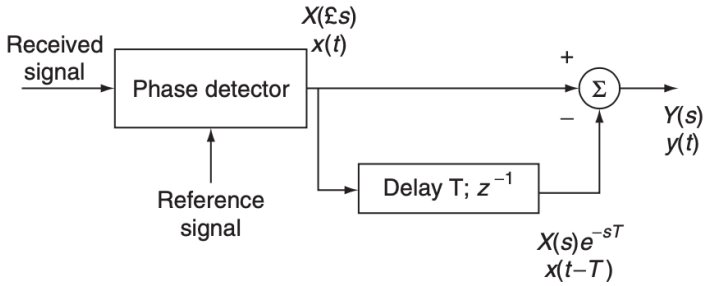

Figure 4.5: Single Delay-Line Canceller (source: [26])

Figure 4.5 shows a basic single delay-line canceller setup commonly employed in MTI radar systems. In this configuration, the delay line shifts the signal by an amount equal to the pulse repetition period. The received signal and the delayed reference signal are then fed into a phase detector (or mixer), producing an output that reflects the phase difference between the two inputs. As reported in [26], the canceller's time-domain response can be mathematically represented as follows:

$$y(t) = x(t) - x(t - T). \tag{4.1}$$

In the frequency domain, the canceller's output can be described by:

$$Y(\omega) = X(\omega)[1 - \exp(-j\omega T)]. \tag{4.2}$$

The transfer function of the filter is given by:

$$H(\omega) = \frac{Y(\omega)}{X(\omega)} = [1 - \exp(-j\omega T)] = 2j \sin \frac{\omega T}{2} \exp\left(-\frac{j\omega T}{2}\right), \tag{4.3}$$

$$|H(\omega)| = 2|\sin \frac{\omega T}{2}|. \tag{4.4}$$

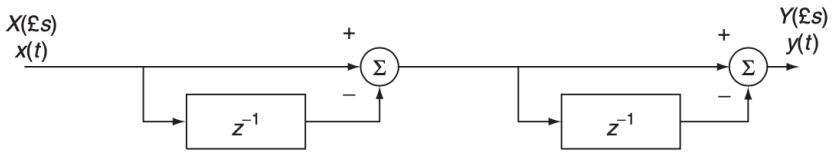

Figure 4.6: A Double Canceller (source: [26])

Two single delay-line cancellers can be cascaded to create a double canceller, as shown in Figure 4.6. The transfer function associated with this double-stage configuration is expressed as:

$$|H(\omega)| = 4\sin^3\frac{\omega T}{2}. \tag{4.5}$$

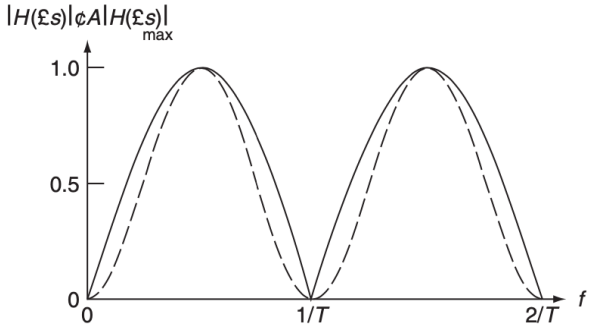

Figure 4.7: Frequency Responses of a Single Canceller (Solid Line) and a Double Canceller (Dashed Line) (source: [26])

4.5.2 Blind Speeds

Echoes from targets travelling at certain velocities are strongly attenuated, making them effectively invisible to the radar. These velocities are commonly referred to as blind speeds.
As discussed in [26], the blind speed problem can be alleviated by using a staggered Pulse Repetition Frequency (PRF) technique. This approach varies the time between pulses by employing multiple PRFs and incorporates the corresponding time delays within the canceller filter. By doing so, the first null in the filter's frequency response and consequently the associated blind speed is shifted to a higher velocity. Consider a double canceller operating with staggered pulse repetition intervals (PRIs) of aT and $(2-a)T$, which results in an average delay of T.

4.6 Radar Sensitivity of MP-PAWR

4.6.1 Received power from a single fixed particle

As discussed in [16] and [27], for a monostatic radar system where the same antenna is employed for both transmission and reception ($G = G_r = G_t$ and $R = R_r = R_t$) the radar equation for a point target reduces to the well-known form:

$$P_r = \frac{P_t\, G_t\, G_r\, \lambda^2\, \sigma}{(4\pi)^3\, R^4\, L}, \tag{4.6}$$

where:

- G_t: Transmit Array Gain
- G_r: Receive Array Gain, given by

$$G_r = \frac{4\pi A_{\text{eff}}}{\lambda^2}, \quad A_{\text{eff}} = A \cdot \eta, \quad \eta = 0.7$$

- L: Total System Losses (linear scale), defined as

$$L = 10^{L_{\text{dB}}/10}, \quad L_{\text{dB}} \approx 3 \text{ dB}$$

- λ: Wavelength
- P_t: Transmitted Power
- σ: Radar Cross-Section (RCS), which quantifies how detectable a target is by radar. It represents the portion of transmitted energy scattered back to the radar receiver. RCS is usually expressed in square meters (m^2):

$$\sigma = \lim_{R \to \infty} 4\pi R^2 \frac{|E_s|^2}{|E_i|^2}, \tag{4.7}$$

where:

  - R: distance between the radar and the target
  - E_s: scattered electric field

– E_i: incident electric field

The RCS of a single droplet (if it is isolated and does not interact with others) does not change with distance from the radar.
On the other hand, radar does not observe individual droplets, but measures the power reflected by an entire volume (called the resolution volume), which varies with distance.

- Resolution volume increases with R: The radar sampling volume increases with the square of the distance

  $$V(R) \propto R^2 \, \Delta r \, \theta_{beam}^2$$

  Even if the concentration of raindrops is constant, the farther you go, the more drops are included in each "bin" $\longrightarrow$ thus more power is backscattered $\longrightarrow$ leading to a higher volumetric RCS.

- Absorption and attenuation (in X-band): The X-band is strongly affected by attenuation caused by rain. At greater distances, the power reflected by more distant drops can be absorbed or scattered by nearer ones, causing the RCS to appear to decrease with distance, even though the individual drops remain unchanged.

- System noise and radar sensitivity: The radar has a minimum detectable signal threshold. At longer distances, the backscattered signal can drop below the noise floor.

  This can make it seem like the drops "disappear" or have a lower RCS.

4.6.2 Received power from distributed particles in a volume

Following [16] and [28], instead of considering an individual particle, a collection of scatterers distributed within a volume (e.g., raindrops in a given air volume) is analysed. The volume backscattering cross section per unit volume, denoted as η, is then introduced.

$$\eta = \frac{d\sigma}{dV}. \tag{4.8}$$

The definition (4.8) is the radar backscattering cross section per unit volume, the sum of all individual radar cross sections σ_i of the particles inside a unit volume.
A weather radar observes a volume containing N particles per cubic meter, each with a backscatter cross-section σ_b. The volume backscatter density η is defined as:

$$\eta = N \cdot \sigma_b \quad \left[\mathrm{m}^{-1}\right] \tag{4.9}$$

The power received, as read in [16] and [28], from a radar resolution volume V is:

$$P_r = \frac{P_t G^2 \lambda^2}{(4\pi)^3 R^4 L} \cdot \eta \cdot V, \tag{4.10}$$

where:
P_t is the transmitted power,
G is the antenna gain,
λ is the radar wavelength,
R is the range,
L represents system losses.

The radar resolution volume $V(R)$ is:

$$V(R) = c\tau \frac{\theta\phi}{2} R^2, \tag{4.11}$$

where:
c is the speed of light,
τ is the transmitted pulse duration,
θ, ϕ are the beamwidths in radians.

Substituting (4.11) into the (4.10) equation yields:

$$P_r = \frac{P_t G^2 \lambda^2 c\tau\theta\phi}{2(4\pi)^3 L R^2} \cdot \eta. \tag{4.12}$$

For spherical raindrops in the Rayleigh scattering regime ($D \ll \lambda$), the backscatter cross-section of each drop is:

$$\sigma_b = \frac{\pi^5 |K|^2 D^6}{\lambda^4}, \tag{4.13}$$

where:
D is the drop diameter,
$|K|^2$ is the dielectric factor of water (approximately 0.93 for liquid water).

The radar reflectivity factor Z, as reported in [15], is defined as the sum of D^6 over all drops:

$$Z = \sum D^6 \implies \eta = \frac{\pi^5 |K|^2}{\lambda^4} Z. \tag{4.14}$$

Therefore, the received power can be expressed as:

$$P_r = \frac{C \cdot Z}{R^2}, \tag{4.15}$$

where the constant C includes all radar system parameters:

$$C = \frac{P_t G^2 c\tau\theta\phi\pi^5 |K|^2}{2(4\pi)^3 L\lambda^2} \tag{4.16}$$

Finally, reflectivity is often expressed in decibel units (dBZ):

$$\text{dBZ} = 10 \log_{10}(Z)$$

4.6.3 Noise in Radar Systems

In according with [16] and [27], the radar receiver's signal includes noise in addition to the echo power. This noise power (P_n) determines the minimum detectable signal power of the receiver. This noise power comes from the environment, which is received by the antenna, but noise is also generated within the radar receiver's electronics. In the absence of any echo power, the power measured at the output of the receiver is noise. Interference from anthropogenic sources is neglected because it does not typically drive the

estimates of radar system performance.
The noise power of a noise temperature (T_n) and a system bandwidth B is

$$P_n = k_B \, T_n \, B, \tag{4.17}$$

where $k_b = 1.380649 \cdot 10^{-23} J \, K^{-1}$ is Boltzmann's constant.
For determining receiver noise for the minimum detectable signal, B is the receiver filter's bandwidth.
The total noise temperature is a function of the radar system and the environment. This noise temperature is largely dominated by the receiver's physical temperature but can be influenced by the background temperature in the direction the antenna is pointing.
Each component has its own noise contribution. Some can be negligible, some significant. The noise factor (F) defines the ratio of the input signal-to-noise ratio (SNR) to the output SNR as

$$F = \frac{SNR_{in}}{SNR_{out}}, \tag{4.18}$$

where $F \geq 1$. This means that the SNR of the output is the same as or lower than SNR at the input of the device (without changing the bandwidth).
The SNR, as reported in [16] and [27], determines the radar's ability to detect a given signal power, and therefore the radar system's performance is strongly tied to receiver's noise figure.
If the physical temperature of the device is varied, the input noise temperature and therefore noise factor are also varied. The additional noise temperature contribution of the system (T_{sys}) and the noise factor (F), are related as

$$F = \frac{T_{sys}}{T_0} + 1, \tag{4.19}$$

$$T_{sys} = T_0(F - 1), \tag{4.20}$$

where $T_0 = 290 \, K$.

The noise power can be calculated using the system and reference temperatures, or equivalently the noise factor, as

$$P_n = k_B(T_{sys} + T_0)B = k_B\, T_0\, F\, B \tag{4.21}$$

Note that the radar signal's bandwidth (B) is typically the only parameter available to the radar operator once the radar is designed and built.

Minimum Detectable Power

As reand in [16], to compute the minimum detectable power P_{min}, the rain attenuation A along the propagation path can be incorporated into the radar equation or included in the minimum required SNR threshold.

$$P_{min} = \frac{SNR_{min}\, P_{noise}}{A}, \tag{4.22}$$

$$A = \exp(-2\gamma R), \tag{4.23}$$

where:
P_{min} is the Minimum detectable power at the radar receiver (this is the lowest signal power the radar can detect above noise),
SNR_{min} is the Minimum signal-to-noise ratio,
P_{noise} is the Noise power at the receiver,
A is the Attenuation factor representing the fraction of power remaining after propagation through an attenuating medium,
γ is the Specific attenuation coefficient (usually in dB/km or Np/km), representing how much the signal power is reduced per unit distance in the medium,
R is the One-way distance the radar signal travels through the attenuating medium.
The specific attenuation γ (dB/km), in according with [29], is obtained from the rain rate R_r (mm/h) using the power-law relationship:

$$\gamma = k\, R_r^{\alpha} \tag{4.24}$$

Values for the coefficients k and α, as read in [29], are determined as functions of frequency, f (GHz), in the range from 1 to 1000 GHz, from

the following equations, which have been developed from curve-fitting to power-law coefficients derived from scattering calculations:

$$\log_{10} k = \sum_{j=1}^{4} \left(a_j \exp \left[- \left(\frac{\log_{10} f - b_j}{c_j} \right)^2 \right] \right) + m_k \log_{10} f + c_k, \quad (4.25)$$

$$\alpha = \sum_{j=1}^{5} \left(a_j \exp \left[- \left(\frac{\log_{10} f - b_j}{c_j} \right)^2 \right] \right) + m_\alpha \log_{10} f + c_\alpha, \quad (4.26)$$

where:
f is the frequency (GHz),
k: either k_H or k_V,
α: either α_H or α_V.

The constants for the coefficient k_H corresponding to horizontal polarization are listed in Table 4.2, while those for the coefficient k_V (vertical polarization) are provided in Table 4.3. Similarly, Table 4.4 presents the constants associated with the coefficient α_H for horizontal polarization, and Table 4.5 reports those for α_V corresponding to vertical polarization.

j	a_j	b_j	c_j	m_k	c_k
1	−5.33980	−0.10008	1.13098	−0.18961	0.71147
2	−0.35351	1.26970	0.45400		
3	−0.23789	0.86036	0.15354		
4	−0.94158	0.64552	0.16817		

Table 4.2: Coefficients for k_H (source: [29])

j	a_j	b_j	c_j	m_k	c_k
1	−3.80595	0.56934	0.81061	−0.16398	0.63297
2	−3.44965	−0.22911	0.51059		
3	−0.39902	0.73042	0.11899		
4	0.50167	1.07319	0.27195		

Table 4.3: Coefficients for k_V (source: [29])

j	a_j	b_j	c_j	m_α	c_α
1	−0.14318	1.82442	−0.55187		
2	0.29591	0.77564	0.19822		
3	0.32177	0.63773	0.13164	0.67849	−1.95537
4	−5.37610	−0.96230	1.47828		
5	16.1721	−3.29980	3.43990		

Table 4.4: Coefficients for α_H (source: [29])

j	a_j	b_j	c_j	m_α	c_α
1	−0.07771	2.33840	−0.76284		
2	0.56727	0.95545	0.54039		
3	−0.20238	1.14520	0.26809	−0.053739	0.83433
4	−48.2991	0.791669	0.116226		
5	48.5833	0.791459	0.116479		

Table 4.5: Coefficients for α_V (source: [29])

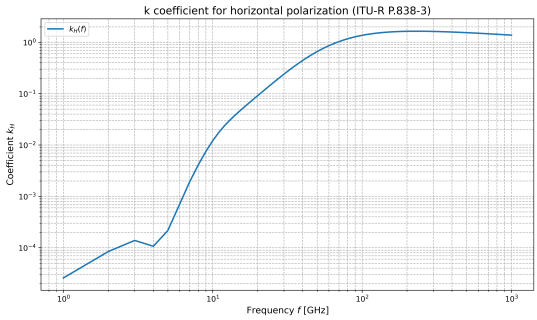

Figure 4.8: k for horizontal polarization (source: [29])

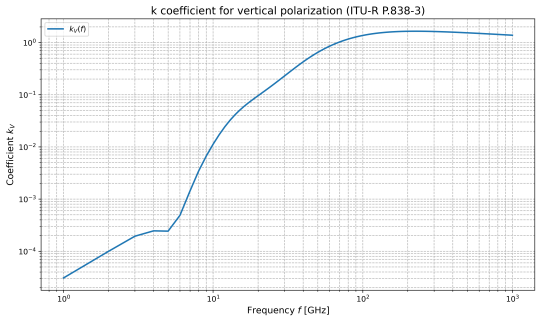

Figure 4.9: k for vertical polarization (source: [29])

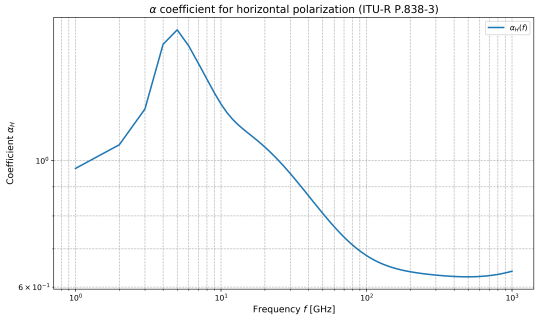

Figure 4.10: α for horizontal polarization (source: [29])

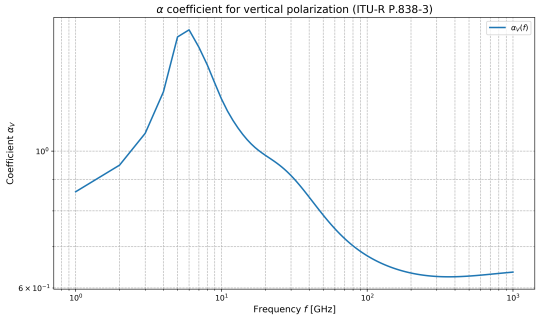

Figure 4.11: α for vertical polarization (source: [29])

According to [29], for both linear and circular polarizations and for any propagation path geometry, the coefficients in equations for α and k can be determined using the following relations:

$$k = \frac{1}{2}\left[k_H + k_V + (k_H - k_V)\cos^2\theta\cos 2\tau\right], \tag{4.27}$$

$$\alpha = \frac{1}{2k}\left[k_H\alpha_H + k_V\alpha_V + (k_H\alpha_H - k_V\alpha_V)\cos^2\theta\cos 2\tau\right], \tag{4.28}$$

where θ denotes the elevation angle of the propagation path, and τ represents the polarization tilt angle with respect to the horizontal plane ($\tau = 45°$ for circular polarization). For the present study, θ is fixed at 45° for the selected beam direction, and τ is set at 0°, as the phased array is dual-polarised and only the horizontal polarisation component is considered. Considering equation (4.24), it is possible to evaluate the specific attenuation coefficient for different rainfall rates (R_r).

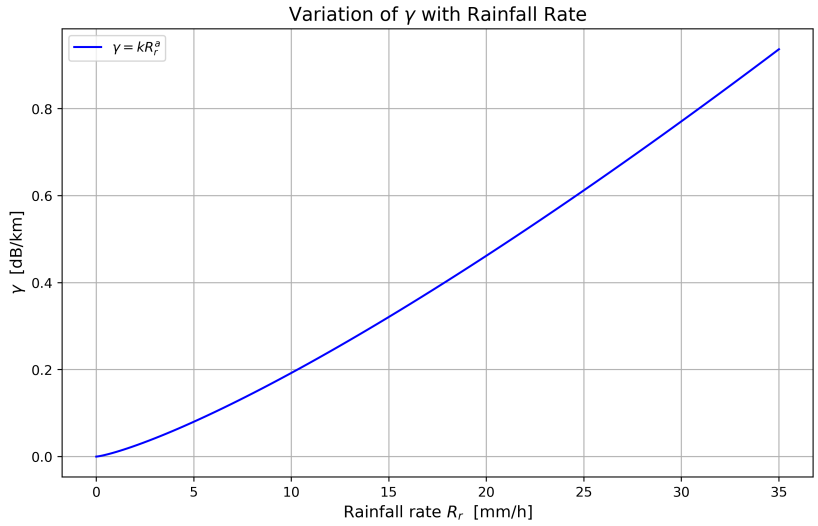

Figure 4.12: Variation of γ as a function of rainfall rate R_r [mm/h]

In Figure 4.12, for a rainfall rate of $R_r = 10$ mm/h, the specific attenuation coefficient can be estimated as $\gamma \approx 0.2$ dB/km. This implies that, over a propagation path of 10 km, the total power loss amounts to approximately 2 dB.

4.6.4 MP-PAWR Radar Sensitivity as a Function of Range

As discussed in [16, 28], the minimum detectable reflectivity $Z_{\min}$ of a radar system can be derived from its minimum detectable power $P_{\min}$. Specifically, $Z_{\min}$ is related to $P_{\min}$ through the radar equation, and is given by:

$$Z_{\min} = \frac{P_{\min}\, r^2}{C}, \tag{4.29}$$

where r is the distance to the target and C is the radar constant, which depends on the system parameters. By knowing the minimum power the radar can detect, the target range, and the radar constant, one can estimate the weakest reflectivity signal that the radar is capable of observing.

Parameter	Value
Frequency, f	9.71 GHz
Transmitted Power, P_t	4800 W
Transmitting Antenna Gain, G_t	32 dBi
Receiving Antenna Gain, G_r	41 dBi
Beamwidth Elevation, θ	0.0436 rad
Beamwidth Azimuth, ϕ	0.165 rad
Boltzmann Constant, k_b	1.38×10^{-23} J/K
Reference Temperature, T	290 K
Bandwidth, B	1.63 MHz
Noise Figure, F	1.2
Pulse Duration, τ	0.5 μs
Losses, L	3 dB
Speed of Light, c	3×10^8 m/s
Minimum Signal-to-Noise Ratio, SNR_{min}	2 (linear)
Dielectric Factor, K^2	0.93

Table 4.6: Radar Parameters Used for Sensitivity Calculation

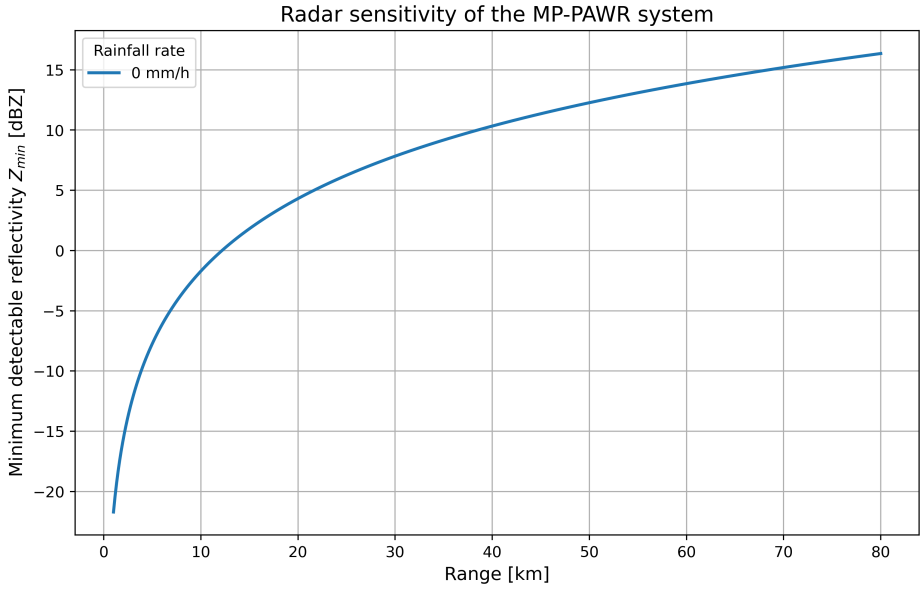

Figure 4.13: Minimum detectable radar reflectivity

Figure 4.13 illustrates the radar sensitivity of the MP-PAWR system, for a rainfall rate of $R_r = 0$ mm/h.

Methods for Data Evaluation and Statistical Analysis

5.1 Volumetric Matching of Radar Observations

Volume matching, as presented in [30, 31], is a technique used to compare observations from two radar systems that are sampling the same atmospheric volume. Its primary aim is to assess the degree of spatial and temporal consistency between their respective measurements.
Schwaller and Morris proposed a methodology that explicitly acknowledges the three-dimensional nature of radar data and the inherently irregular manner in which radars sample the atmosphere. Instead of relying on direct point-to-point comparisons, their approach identifies and examines corresponding three-dimensional volumes within the two datasets. By doing so, the comparison is grounded in a more physically meaningful framework, ensuring that both radars are effectively observing the same portion of the atmosphere.
A central difficulty in comparing measurements from two radar systems lies in the fact that they do not sample the atmosphere in an identical fashion. Each radar possesses its own spatial resolution, governed by factors such as beamwidth, pulse length, range resolution, and scanning strategy. These characteristics determine the size and shape of the atmospheric volume sensed by the radar at any given moment. Consequently, two radars observing the same meteorological system may effectively "see" it at different spatial scales and with differently shaped sampling volumes. Such disparities in spatial resolution can be sufficiently large to render simple point-to-point comparisons misleading or entirely inappropriate. The volume matching technique was specifically developed to address this issue.

Instead of comparing individual radar gates, which rarely coincide spatially or represent equivalent atmospheric volumes, the method isolates regions of the atmosphere that are genuinely sampled by both radars. These shared regions form the foundation of a meaningful and reliable comparison.
Volume matching overcomes the limitations imposed by differing sampling geometries by modelling the precise three-dimensional pulse volumes of each radar and determining where these volumes intersect. From this, the technique constructs common comparison volumes that represent only those parts of the atmosphere jointly observed by both systems. Within such volumes, the measurements from each radar can be regarded as observations of the same atmospheric target, irrespective of differences in their native resolutions.
Once the overlapping volumes have been established, the radar data can be combined, averaged, or re-gridded so that both systems contribute information to the same spatial units. By explicitly accounting for differences in spatial sampling, volume matching provides a rigorous and physically coherent foundation for radar inter-comparison, making it particularly valuable in studies involving ground-based and satellite radars, dual-polarisation instruments, or sensors with markedly different spatial resolutions.

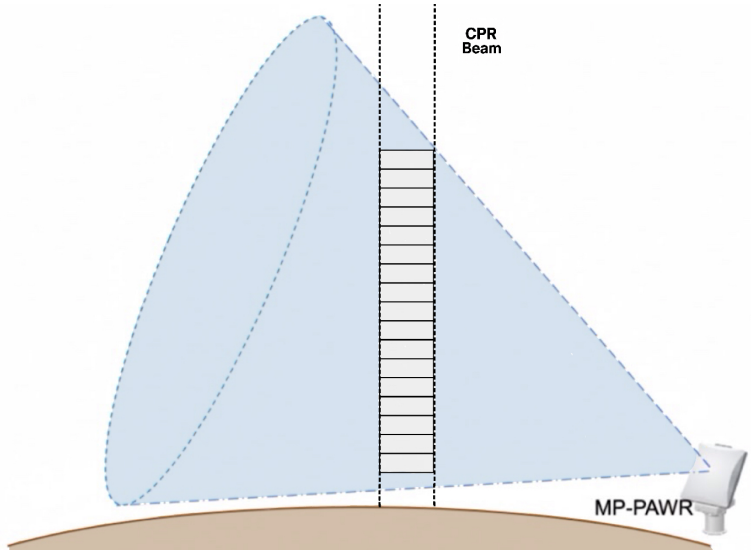

Figure 5.1: Schematic illustration of volume matching

In Figure 5.1, the grey area of the CPR (Cloud Profiling Radar) beam indicates the averaging volume used for the comparison.
Considering the EarthCARE CPR and the MP-PAWR radar, the two instruments exhibit different spatial resolutions. The CPR has a vertical

resolution of 500 m and a horizontal resolution of 1000 m (Joint Standard Grid), whereas the MP-PAWR has a range resolution of 150 m and an angular resolution in elevation of 0.8° and in azimuth of 1.2°. However, the transverse cell size varies along the range, meaning that the overall spatial resolution is not constant with distance. In the case studies presented, the MP-PAWR spatial resolution is considerably finer than that of the CPR. Therefore, comparison must be performed on a common grid, associating each EarthCARE CPR point with a parallelepiped volume centred on the point with dimensions dx, dy, and dz. This volume represents the comparison volume, the space within which corresponding MP-PAWR points are sought.
For each EarthCARE point (x_0, y_0, z_0), it is possible to identify MP-PAWR points located within a radius

$$r = \sqrt{(dx/2)^2 + (dy/2)^2 + (dz/2)^2}. \tag{5.1}$$

Subsequently, it is possible to apply a precise filter to select only the points contained within the parallelepiped, according to the following equations:

$$|x_i - x_0| \leq dx/2, \quad |y_i - y_0| \leq dy/2, \quad |z_i - z_0| \leq dz/2. \tag{5.2}$$

After performing a volumetric match, the linear reflectivity values from the MP-PAWR are averaged, with the following equation:

$$\overline{Z}_{lin} = \frac{1}{N} \sum_{i=1}^{N} Z_{lin,i}. \tag{5.3}$$

Finally, by employing the volumetric matching method, the mean distance and mean time difference can be calculated. These metrics are essential for quantifying the spatial and temporal correspondence between the EarthCARE and MP-PAWR measurements.

$$d_{mean} = \frac{1}{N} \sum_{i=1}^{N} \sqrt{(x_i - x_0)^2 + (y_i - y_0)^2 + (z_i - z_0)^2}, \tag{5.4}$$

where the i-th term represents the MP-PAWR point, and the term with subscript 0 represents the CPR point.
For each EarthCARE point, the mean temporal difference is determined by first selecting all MP-PAWR points within the associated comparison volume. The absolute time difference between each of these MP-PAWR

points and the EarthCARE point is then calculated, using the following equation.

$$\Delta t_i = \left| t_{\text{MP-PAWR},i} - t_{\text{EarthCARE}} \right| . \tag{5.5}$$

The mean time difference is subsequently calculated by taking the average of these individual values, offering an indication of the temporal correspondence between the matched MP-PAWR and EarthCARE observations, as expressed by the following equation:

$$\Delta t_{\text{mean}} = \frac{1}{N} \sum_{i=1}^{N} \Delta t_i. \tag{5.6}$$

After performing the volumetric matching, a scatter plot is generated to compare the measurements from the two radars.

5.2 Statistical Measures for Model Assessment

5.2.1 Bias

The Bias is a measure of the systematic difference between two datasets. It quantifies whether one dataset tends to overestimate or underestimate the other. For example, considering the datasets of MP-PAWR ($\sigma_{MP-PAWR}$) and the Cloud Profiling Radar (CPR) of EarthCARE (σ_{EC}), the BIAS can be calculated as:

$$BIAS = \frac{1}{N} \sum_{i=1}^{N} \left(\sigma_{MP-PAWR,i} - \sigma_{EC,i} \right) , \tag{5.7}$$

where N is the number of matched data points.
If the BIAS value is greater than zero, the values obtained with MP-PAWR tend to be higher than those obtained with the CPR of EarthCARE. For further details, see [32].

5.2.2 RMSE (Root Mean Square Error)

The Root Mean Square Error (RMSE), as reported in [32], measures the magnitude of the differences between two datasets, regardless of the sign. The RMSE is defined as:

$$RMSE = \sqrt{\frac{1}{N}\sum_{i=1}^{N}\left(\sigma_{MP-PAWR,i} - \sigma_{EC,i}\right)^2}. \tag{5.8}$$

A large RMSE indicates that the datasets differ substantially, even if the BIAS is small.

5.2.3 Pearson Correlation Coefficient (r)

The Pearson Correlation Coefficient quantifies the degree to which two datasets vary linearly with respect to each other. It is defined as the ratio between the covariance of the two variables and the product of their standard deviations.

$$r = \frac{\sum_{i=1}^{N}\left(\sigma_{MP-PAWR,i} - \bar{\sigma}_{MP-PAWR}\right)\left(\sigma_{EC,i} - \bar{\sigma}_{EC}\right)}{\sqrt{\sum_{i=1}^{N}\left(\sigma_{MP-PAWR,i} - \bar{\sigma}_{MP-PAWR}\right)^2}\sqrt{\sum_{i=1}^{N}\left(\sigma_{EC,i} - \bar{\sigma}_{EC}\right)^2}}, \tag{5.9}$$

where $\bar{\sigma}_{MP-PAWR}$ and $\bar{\sigma}_{EC}$ represent the mean of the datasets:

$$\bar{\sigma}_{MP-PAWR} = \frac{1}{N}\sum_{i=1}^{N}\sigma_{MP-PAWR,i} \ , \ \bar{\sigma}_{EC} = \frac{1}{N}\sum_{i=1}^{N}\sigma_{EC,i}. \tag{5.10}$$

If $r \approx 1$, there is a strong positive correlation, whereas if $r \approx -1$, there is a strong negative correlation, meaning that the datasets vary in opposite directions. When $r \approx 0$, there is no linear correlation.

Methodology and Study Cases

6.1 Methodology

The methodology employed is presented step by step, detailing the implementation in Python scripts, the main functions used, and the overall data processing workflow. A Python script was initially developed to extract the attributes from the EarthCARE files downloaded from the ESA website, allowing a clear visualization of the data structure and organization. This initial exploration provided the necessary understanding to proceed with subsequent analyses.

The satellite's ground track was then plotted, offering an overview of the entire frame coverage over Japan. This visualization enabled the identification of regions of interest and provided context for the spatial and temporal extent of the data. Reflectivity data for the entire frame was subsequently corrected for gas attenuation, focusing on the orbit of interest to ensure relevant coverage. For further theoretical details regarding the reflectivity correction, refer to [7]. Using the known positions of the MP-PAWR radar extracted from the RAW data files, a code was created to visualize the radar's scanning volume. This visualization allowed the determination of the temporal intervals when the satellite entered and exited the radar's scanning volume, enabling a direct comparison of both spatial and temporal coverage between the EarthCARE CPR and the MP-PAWR radar. Once the relevant latitude and longitude coordinates were identified, the visualization volume of the EarthCARE CPR data was reduced to match the corresponding MP-PAWR scanning region, considering the satellite's entry and exit points from the phased array radar volume. This step ensured that the analysis was confined to the overlapping observational domain, providing a consistent basis for comparison. For additional information, see Chapter 4 (section 4.4).

Finally, along-track and altitude plots of the EarthCARE CPR data were

generated for the reduced volume, providing a detailed representation of reflectivity along the satellite's trajectory and facilitating a direct comparison with MP-PAWR measurements within the same spatial and temporal domain. Once the EarthCARE CPR reflectivity values were visualized, a study was conducted to identify regions potentially affected by attenuation, sensitivity variations, and scattering. In particular, a Python script was developed to visualize the multi-scattering phenomenon, as described in detail in [7]. For issues related to attenuation, see Section 4.6, and for non-Rayleigh scattering, see Section 3.4.

The processing of MP-PAWR radar data was carried out using a series of Python scripts designed to handle RAW data files, visualize the radar scanning volume, and extract relevant information for comparison with EarthCARE CPR measurements. Initially, a function was implemented to read the RAW MP-PAWR files and extract both the radar measurements and associated metadata. This function takes as input the file paths of the RAW data and outputs a structured array containing reflectivity, range, azimuth, elevation, and timestamp information. Proper interpretation of the binary format ensures that the metadata is correctly associated with each measurement.

To enable spatial analysis and comparison with EarthCARE, the radar measurements in azimuth, elevation, and range were converted to geodetic coordinates (latitude, longitude, and altitude) through a dedicated function. This function calculates local ENU (East, North, Up) coordinates from the radar measurements and then applies a rotation matrix to transform these coordinates into the Earth-Centered Earth-Fixed (ECEF) reference frame. By adding the radar's ECEF position, the absolute ECEF coordinates of the target points are obtained and subsequently converted back to geodetic coordinates in the WGS84 system. This procedure provides accurate spatial positioning of the radar measurements in a global reference frame. A further function was developed to visualize the three-dimensional scanning volume of the MP-PAWR radar. Using the radar position and the beam parameters extracted from the RAW data, the function generates a 3D representation of the radar scan. This visualization is essential for determining the spatial intersection with the EarthCARE CPR scanning volume and for identifying the temporal intervals during which the satellite enters and exits the radar's scanning region. The entry and exit times are obtained by combining the satellite trajectory with the radar volume boundaries, allowing a precise comparison of spatial and temporal coverage between the two systems.

Additionally, a function was created to extract vertical profiles of reflectivity along user-defined tracks. The function takes as input latitude-longitude points defining the track and the radar data array, and outputs vertical profiles of reflectivity versus altitude for each point. Spatial interpolation is employed to ensure that the profiles accurately correspond to the radar measurements. Finally, additional functions allow filtering of the radar data in altitude and range and the generation of both 3D and 2D visualizations. These functions produce along-track and altitude plots, providing a detailed representation of the radar reflectivity and facilitating direct comparison with EarthCARE CPR data within the same spatial and temporal domain.
For the validation, a Python script was developed implementing a volumetric matching approach based on the method of Schwaller and Morris. For further theoretical details, see Section 5.1. This approach allows each MP-PAWR measurement to be associated with the corresponding EarthCARE CPR voxel, taking into account both spatial proximity and the similarity of radar reflectivity values. Following this volumetric association, the MP-PAWR data were resampled onto a common grid matching the spatial resolution of EarthCARE, effectively degrading the MP-PAWR resolution to ensure consistency between the two datasets. A scatter plot was then generated to compare the reflectivity values observed by MP-PAWR and EarthCARE.
Furthermore, statistical metrics such as the global mean bias, root-mean-square error (RMSE), and Pearson correlation coefficient were computed to quantify the agreement between the two datasets.

6.2 Study Cases

After analysing the available data for comparison, only three days were deemed suitable for the study. These selected days are summarized in the table below.

Date	Obs. Start (UTC)	Obs. End (UTC)	Orbit	Frame
25-08-2024	05:08:35.554	05:20:25.766	1373	D
16-07-2025	05:04:16.623	05:16:07.108	6430	D
10-08-2025	05:04:09.735	05:16:00.085	6819	D

Table 6.1: Selected days for MP-PAWR and EarthCARE comparison.

6.2.1 Study Case 1

Case Study 1 refers to August 25th, 2024, for which a visualization of the ground track of the corresponding orbit 1373 and frame D was obtained.

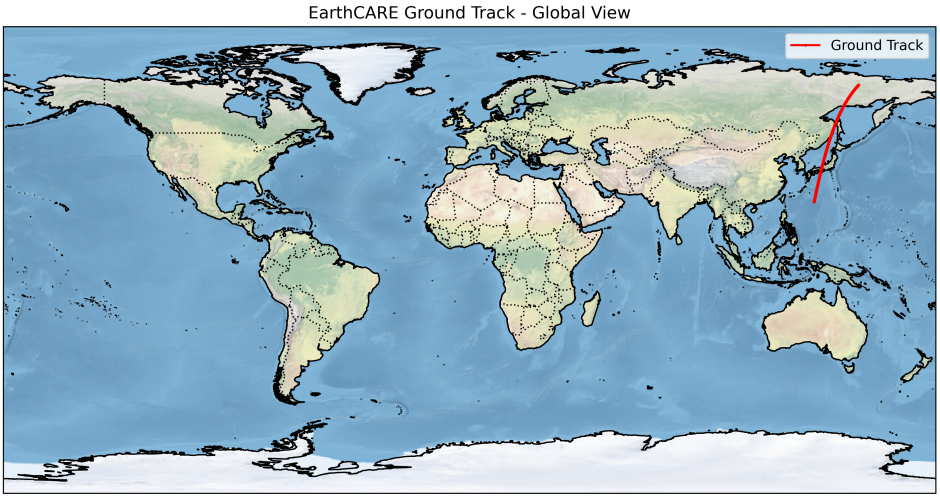

Figure 6.1: EarthCARE global ground track on 25 August 2024

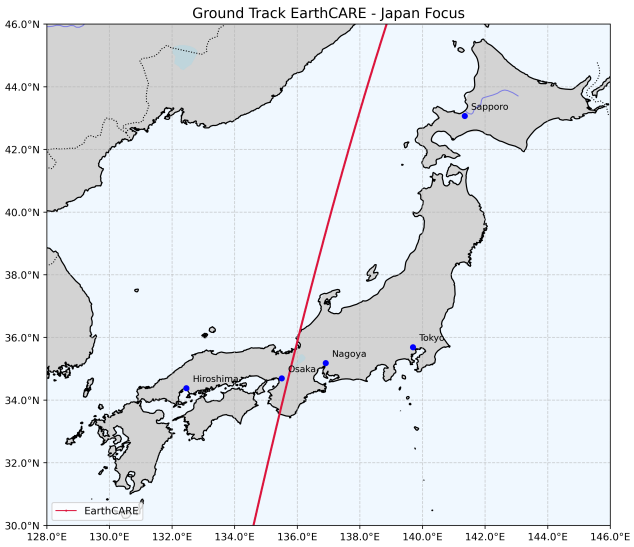

Figure 6.2: EarthCARE ground track above Japan on 25 August 2024

Afterwards, it is possible to obtain the reflectivity and Multi Scattering status for the entire frame, as shown in the figures below.

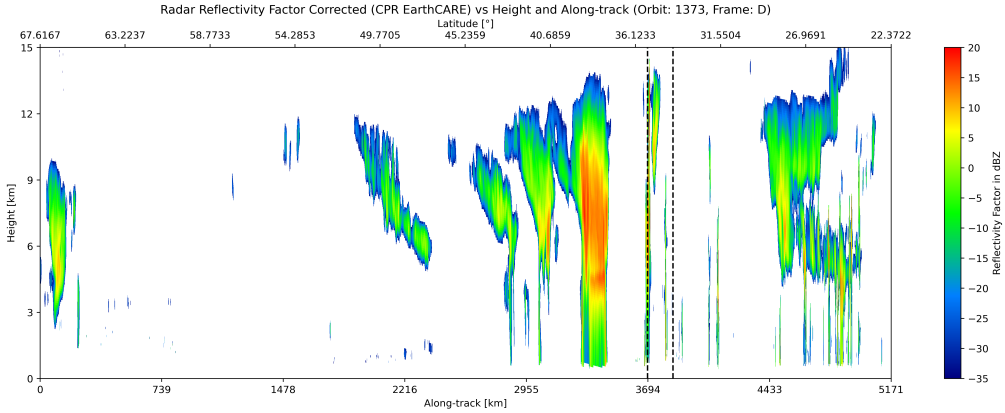

Figure 6.3: Reflectivity observed by the CPR on board EarthCARE on 25 August 2024

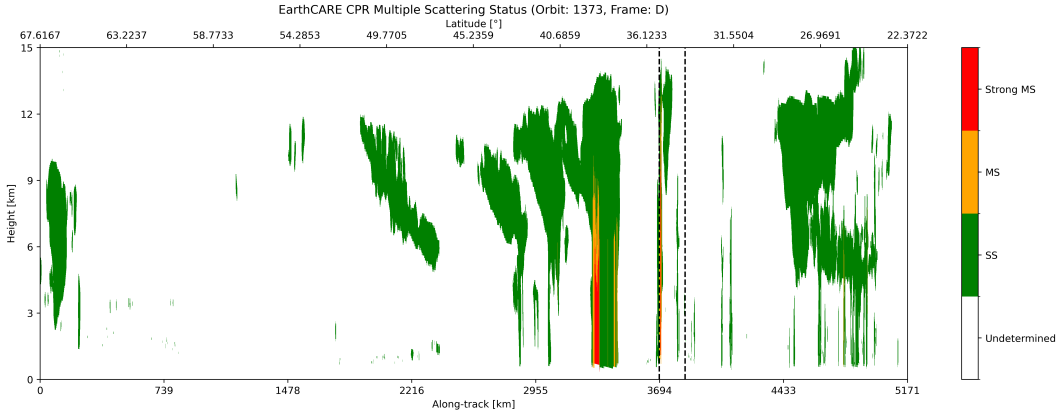

Figure 6.4: MS status observed by the CPR on board EarthCARE on 25 August 2024

For both figures the dashed lines indicate the boundaries of the volume of interest where the ground-based radar is located. From Figure 6.3 one can identify many atmospheric structures: extended cumulus systems that develop up to 10-12 km and isolated convective cells. Variations in reflectivity are visible due to the presence of the bright band, the layer where snow melts into rain located at approximately 4-5 km altitude. In the bright-band region hydrometeors have a higher effective dielectric constant than dry ice, so the radar measures reflectivity values that are larger than the true values.
The red column of high reflectivity between latitudes 36.1233° and 40.6859°

corresponds to a cumulonimbus (a convective cloud). In that region significant signal absorption can occur; consequently the backscattered power returning to the CPR is reduced. This is a major issue for the CPR because attenuation increases with frequency, indeed EarthCARE's CPR operates at 94 GHz (W band), where absorption by precipitation and wet hydrometeors is especially strong. Within this convective region, hydrometeors are closely spaced, leading to a high probability of the radar beam being scattered multiple times by different particles. This phenomenon of multiple scattering, as can be seen in the Figure 6.4, can significantly affect the measured reflectivity (for further thermal information, see [7]).
Following the visualization of the MP-PAWR scanning volume, the area of interest is identified by applying both spatial and temporal synchronization.

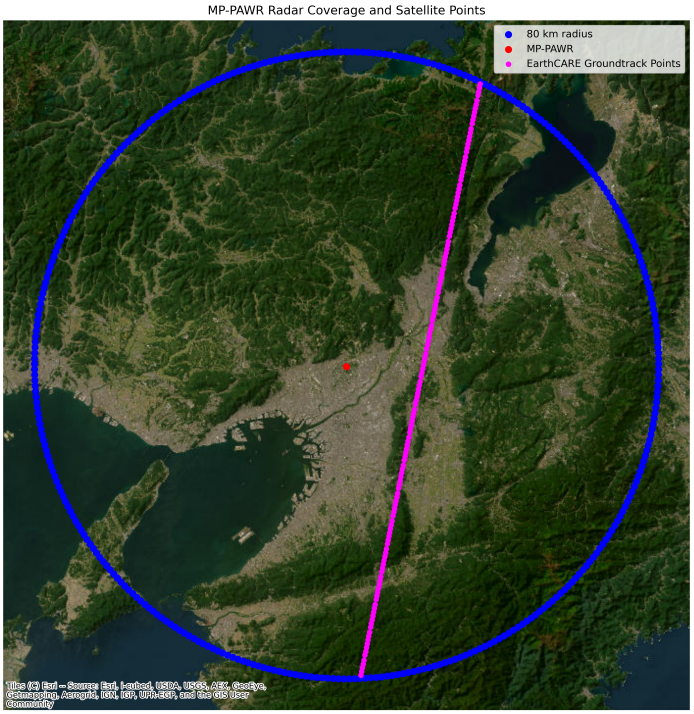

Figure 6.5: MP-PAWR scan volume overlaid with satellite positions on 25 August 2024

The code provides the positions in latitude and longitude at one-second intervals. The satellite enters the scanning volume at 05:18:00.004227 UTC with coordinates $Lat = 35.470994°$ and $Long = 135.897355°$, and exits at 05:18:21.140314 UTC with coordinates $Lat = 34.110143°$ and $Long = 135.563043°$. The minimum distance between the ground-based radar and the EarthCARE radar is 19.23 km, calculated at the same latitude.

The reflectivity and multiple-scattering status within the volume of interest can be visualized.

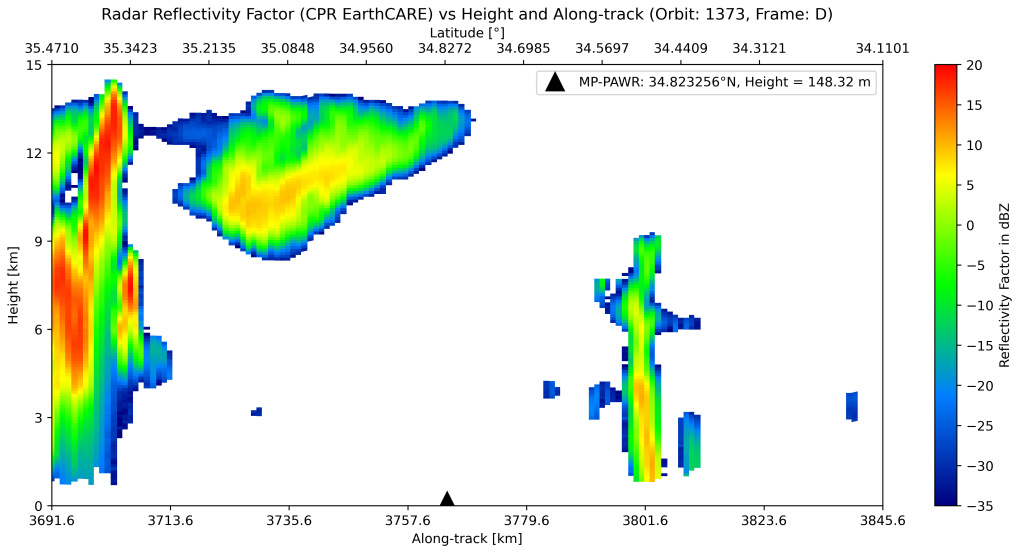

Figure 6.6: Reflectivity of the CPR within the area of interest on 25 August 2024

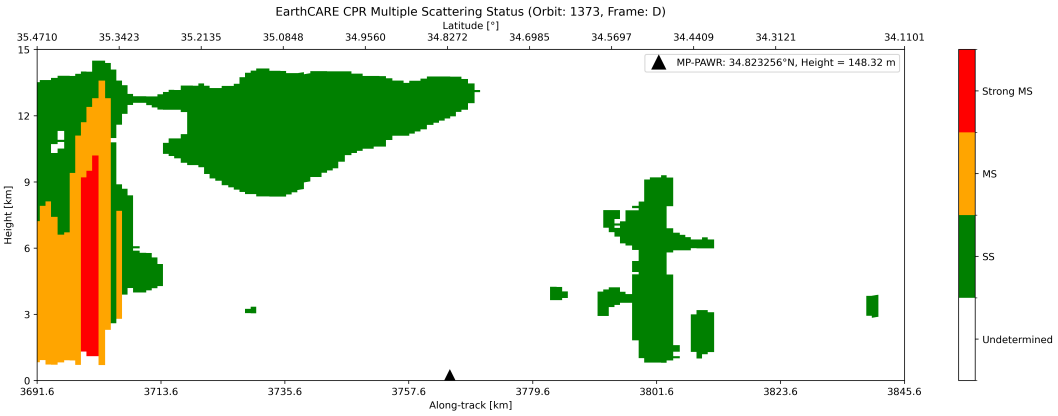

Figure 6.7: Multi-scattering occurrence within the area of interest on 25 August 2024

3D visualization of MP-PAWR data obtained by converting polar to Cartesian coordinates. The comparison is made between reflectivity from horizontal polarization with and without the MTI filter. The dataset includes 331 azimuth and 78 elevation angles.

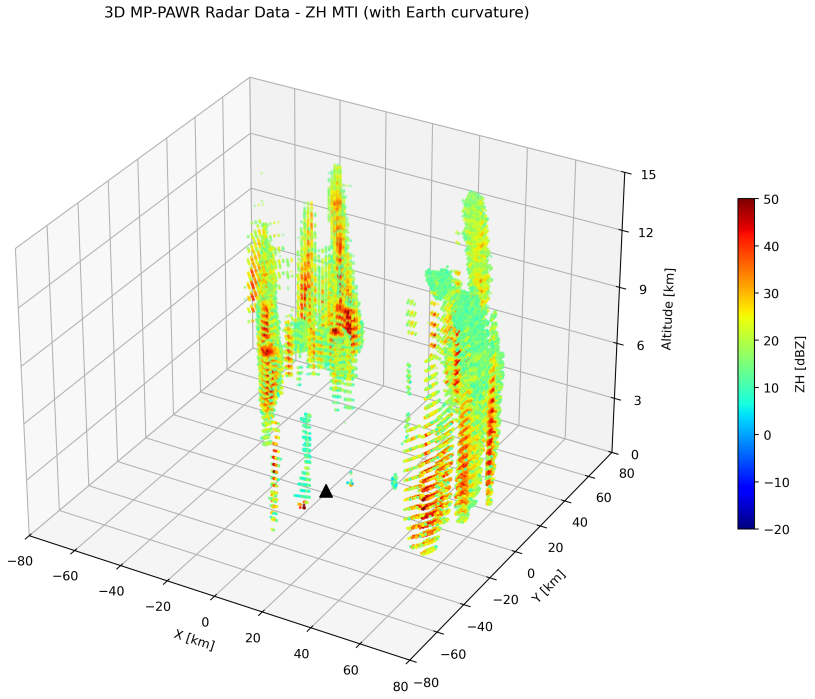

Figure 6.8: 3D visualization with MTI on 25 August 2024

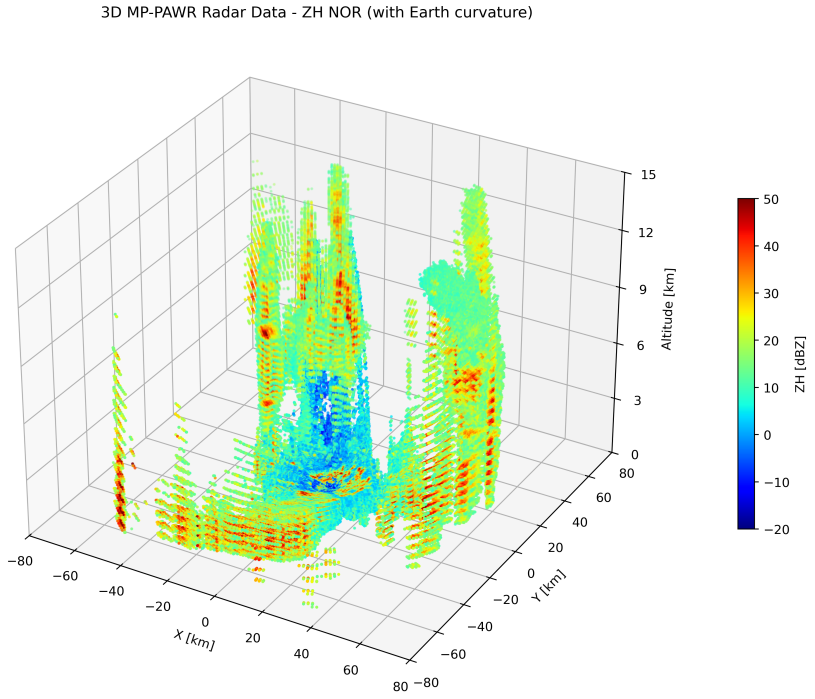

Figure 6.9: 3D visualization without MTI on 25 August 2024

As shown in Figures 6.8 and 6.9, it is possible to observe how the Moving

Target Indicator (MTI) filter operates. The MTI filter is designed to suppress stationary echoes by exploiting the phase differences between consecutive pulses. However, if a target moves slowly, its phase variation can be similar to that of a stationary target, and thus it may be removed as clutter. Additionally, the figures illustrate the effect of the radar's "cone of silence." Directly above the radar, it is impossible to obtain measurements, and at higher altitudes the returned signal is weak, resulting in very low reflectivity values. Furthermore, meteorological events can be analysed using two-dimensional Plan Position Indicator (PPI) plots at low altitudes, around 2–3 km. At these altitudes, the main precipitation structures and rain layers can be observed without clutter interference, allowing an evaluation of the MTI filter's effect.

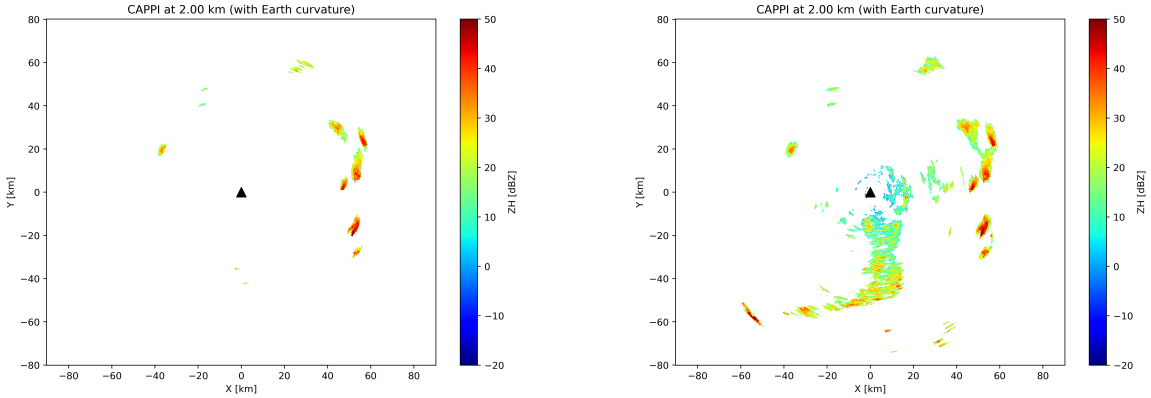

(a) With MTI filter **(b)** Without MTI filter

Figure 6.10: Plan Position Indicator (PPI) at 2 km altitude on 25 August 2024

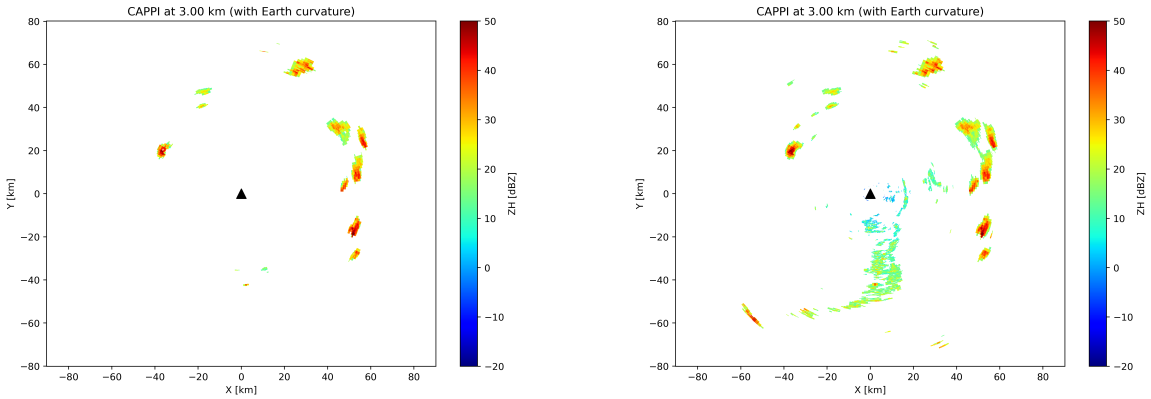

(a) With MTI filter **(b)** Without MTI filter

Figure 6.11: Plan Position Indicator (PPI) at 3 km altitude on 25 August 2024

The images above show the presence of different convective system cells with high precipitation intensity (greater than 40 dBZ), particularly in the eastern and northern quadrants. By fixing the azimuth and elevation angles, it is possible to observe the reflectivity values along the range.

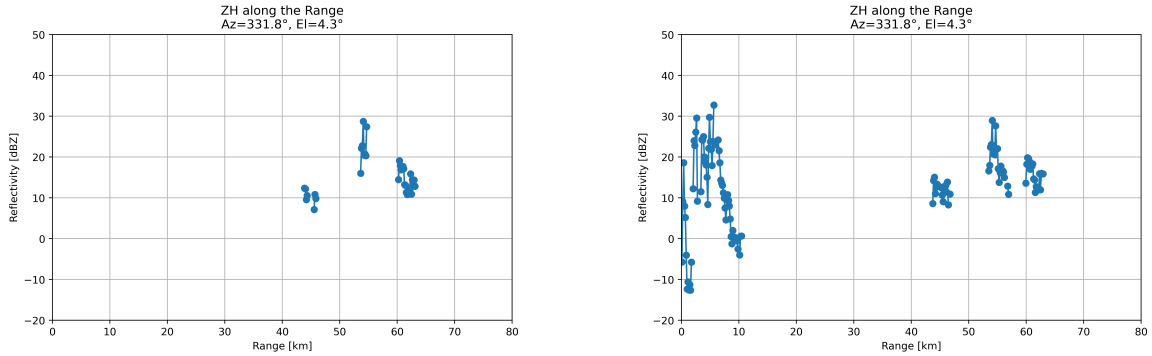

(a) With MTI filter **(b)** Without MTI filter

Figure 6.12: ZH along the range at fixed azimuth 331.8° and elevation 4.3° on 25 August 2024

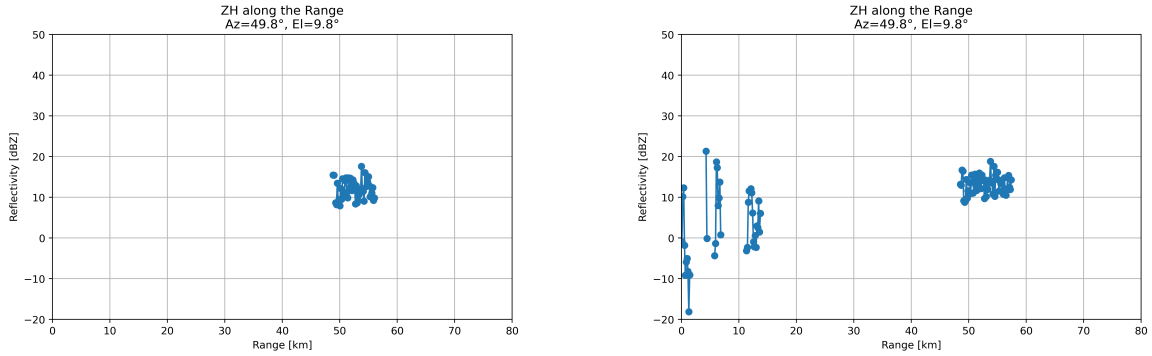

(a) With MTI filter **(b)** Without MTI filter

Figure 6.13: ZH along the range at fixed azimuth 49.8° and elevation 9.8° on 25 August 2024

After converting the MP-PAWR measurements from polar coordinates to Cartesian space and subsequently to geographical coordinates (latitude, longitude, and altitude), including the effect of Earth curvature, it becomes possible to extract vertical profiles of radar reflectivity. These profiles can then be directly compared with the Cloud Profiling Radar (CPR) reflectivity measurements from the EarthCARE satellite.
This comparison enables the evaluation of consistency between ground-based phased array radar observations and spaceborne CPR measurements,

taking into account the differences in frequency, viewing geometry, spatial resolution, and sensitivity between the two instruments.

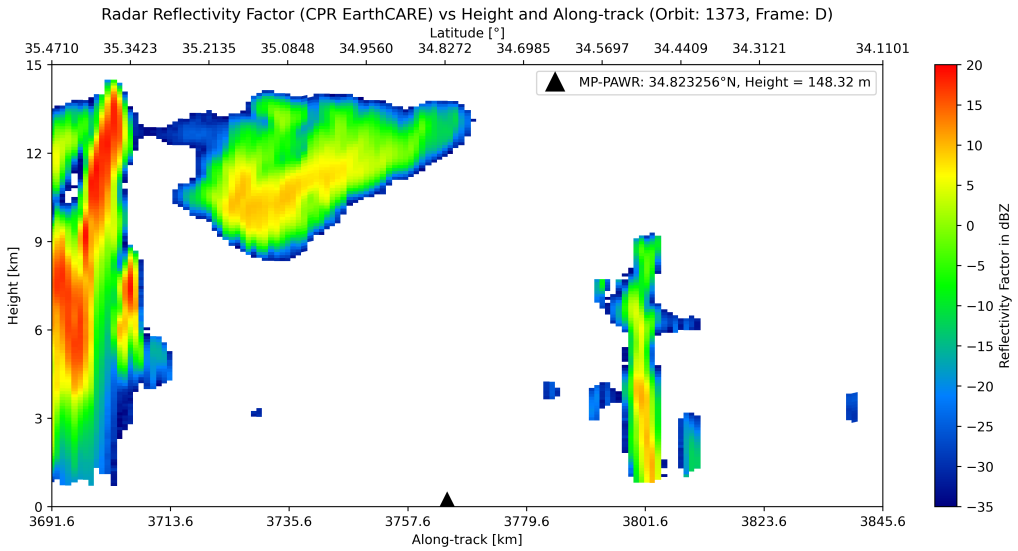

Figure 6.14: Reflectivity of the CPR on 25 August 2024

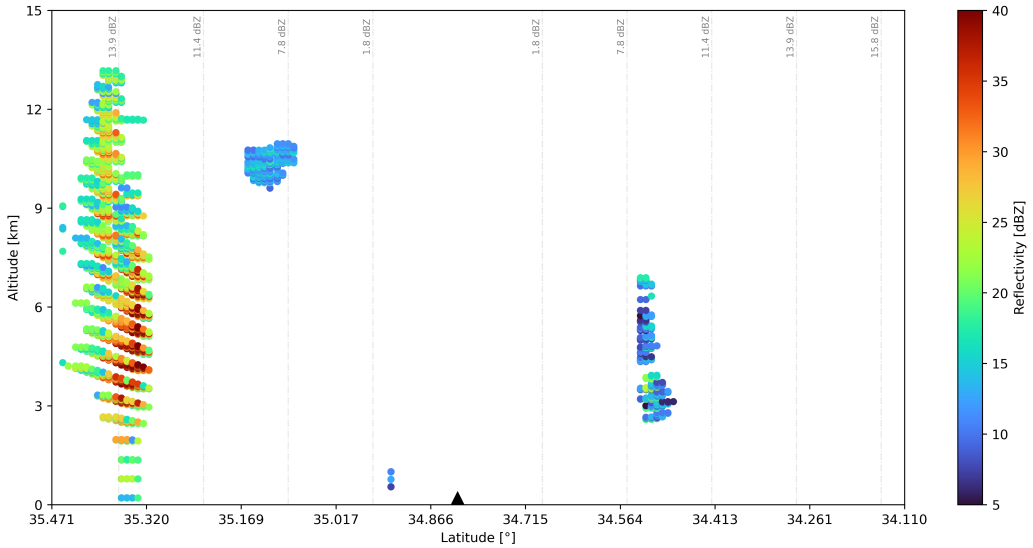

Figure 6.15: MP-PAWR vertical reflectivity profile showing dBZ contour lines, observed on 25 August 2024

In Figure 6.14, a cloud complex can be observed between approximately 35.4° N and 34.7° N latitude. This is a very deep structure extending up to 14-15 km in altitude, with peak reflectivity values reaching 20 dBZ, typical of a large convective system. At lower altitudes, reflectivity values are

attenuated due to the presence of heavy rain beneath the cumulonimbus. Furthermore, around 34.6° N and 34.4° N, a cloud column is visible, extending from approximately 2 to 9 km in altitude, representing a more localized convective structure. The next figure, Figure 6.15, the dashed gray lines indicate the minimum reflectivity values detectable by the MP-PAWR, providing insight into the system's sensitivity. The attenuation issue may occur in the cells located around Lat = 35.471°. A cumulonimbus cloud containing hail or large ice particles, characterized by high reflectivity, can absorb part of the radar signal energy. Consequently, the cells located behind the cumulonimbus, with respect to the radar position, may appear with a lower reflectivity than their actual value. Conversely, the sensitivity issue arises at large distances from the radar, where hydrometeors with weak reflectivity values may not be detected due to the reduced power of the returned signal. After performing a graphical visualisation of the data, a quantitative comparison can be carried out using a volumetric matching approach based on the Schwaller & Morris method. This method allows for pairing values from the two radars by identifying overlapping volumes in space, taking into account the different resolution and orientation of the measurement volumes of the instruments. In the scatter plot, the x-axis represents the reflectivity values measured by EarthCARE, while the y-axis represents the corresponding values from the MP-PAWR radar.

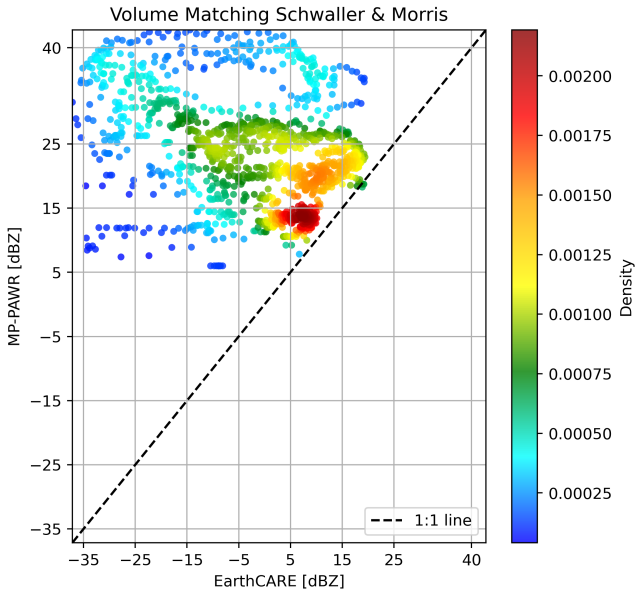

Figure 6.16: Scatter plot of reflectivity on 25 August 2024

Figure 6.16 provides information on the measurements of the two radars. Most of the points lie above the 1:1 line, indicating that the MP-PAWR generally observes higher reflectivity values than the CPR. For validation, it is important to compute the global bias between MP-PAWR and CPR, which is 25.18 dB. Additionally, the Root Mean Square Error (RMSE) was calculated and found to be 31.28 dB. These values confirm that MP-PAWR measures higher reflectivity than CPR. To assess the correlation between the datasets, the Pearson correlation coefficient was computed, resulting in -0.313, indicating no significant correlation.

In Fig. 6.16 it can be seen that a single geolocated point in space may exhibit very different reflectivity values when compared between EarthCARE and MP-PAWR. In some cases, EarthCARE reports a very low reflectivity, while MP-PAWR shows significantly higher values for the same nominal location. This behaviour indicates that a simple one-to-one comparison between the two measurements is not sufficient, and that a more detailed analysis is required to understand the origin of these discrepancies.

To interpret these differences properly, it is useful to distinguish between two possible sources of error: a spatial error and a temporal error. The spatial error is related to the actual distance between the volume observed by EarthCARE and the nearest volume sampled by MP-PAWR. Even when the geographic coordinates appear very similar, the two systems may still be sampling different portions of the atmosphere, especially in regions with strong reflectivity gradients such as convective cores. Even small spatial offsets can therefore result in substantial variations in the observed reflectivity. In parallel, the temporal error arises from the lack of perfect simultaneity between the orbital measurement of EarthCARE and the volumetric scan of MP-PAWR.

The atmosphere can evolve rapidly, and a temporal offset of even a few seconds may lead to significant changes in the reflectivity structure. Thus, an observed difference between the two radars may reflect real atmospheric evolution rather than a measurement issue. For these reasons, it is essential to represent and quantify both the spatial distance between the paired points and the temporal difference between their respective acquisition times. Combining this information with the reflectivity difference allows for a more accurate interpretation of the discrepancies and helps determine whether the anomalous points highlighted in the figure are primarily due to spatial mismatch, temporal misalignment, or to intrinsic differences between the two radar systems.

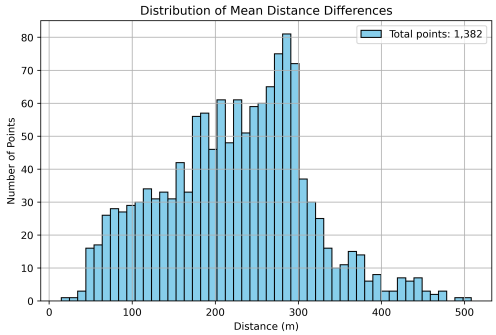

(a) Mean spatial error on 25 August 2024

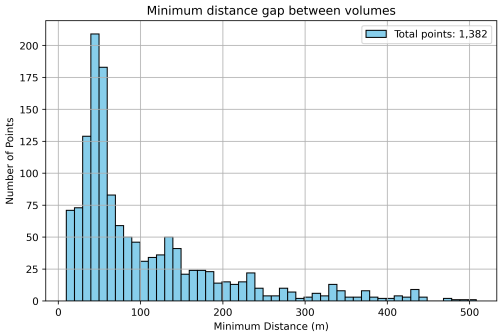

(b) Minimum spatial error on 25 August 2024

Figure 6.17: Mean and minimum spatial errors on 25 August 2024

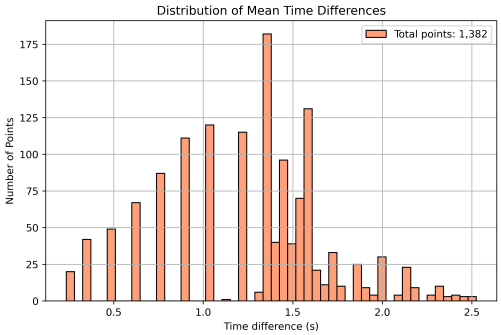

(a) Mean temporal error on 25 August 2024

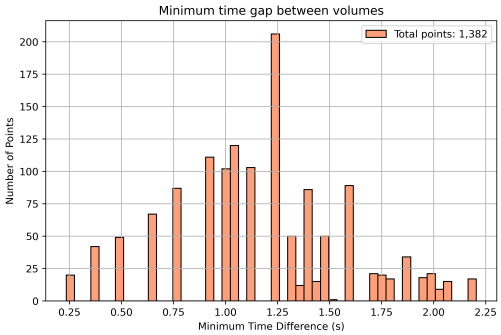

(b) Minimum temporal error on 25 August 2024

Figure 6.18: Mean and minimum temporal errors on 25 August 2024

Figures 6.17a and 6.18a represent the mean values within the volume resolution of the Cloud Profiling Radar, whereas Figures 6.17b and 6.18b show the minimum errors between two volumes.
The analysis of the two radar datasets shows no significant spatial or temporal mismatch. The mean spatial error of approximately 280 metres, as illustrated in Figure 6.17a, indicates that the MP-PAWR data, while contained within the corresponding EarthCARE volumes, are slightly offset. This small discrepancy can affect reflectivity differences, particularly in regions with strong gradients, and highlights the value of a volumetric matching approach such as the Schwaller & Morris method. Any remaining differences are likely due to factors such as viewing geometry, radar frequency, resolution, sensitivity, or georeferencing.

6.2.2 Study Case 2

The same methodological conventions and figure styles as in Case Study 1 are applied. Only the results specific to this date and orbit are discussed. Case Study 3 pertains to July 16th, 2025, during which a ground track visualization of orbit 6430 and frame D was produced.

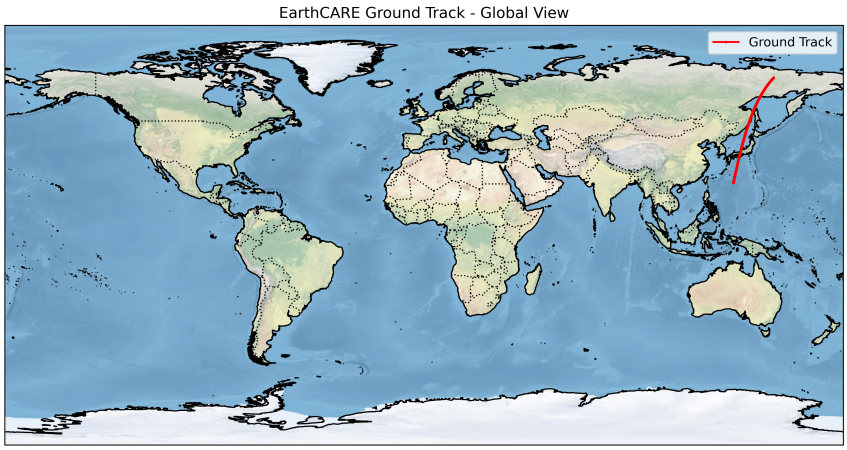

Figure 6.19: EarthCARE global ground track on 16 July 2025

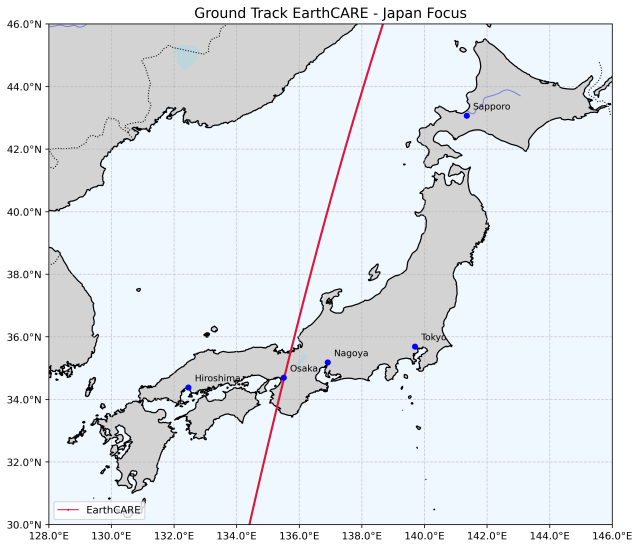

Figure 6.20: EarthCARE ground track above Japan on 16 July 2025

Subsequently, the reflectivity and Multi Scattering status for the entire frame can be retrieved, as illustrated in the figures below.

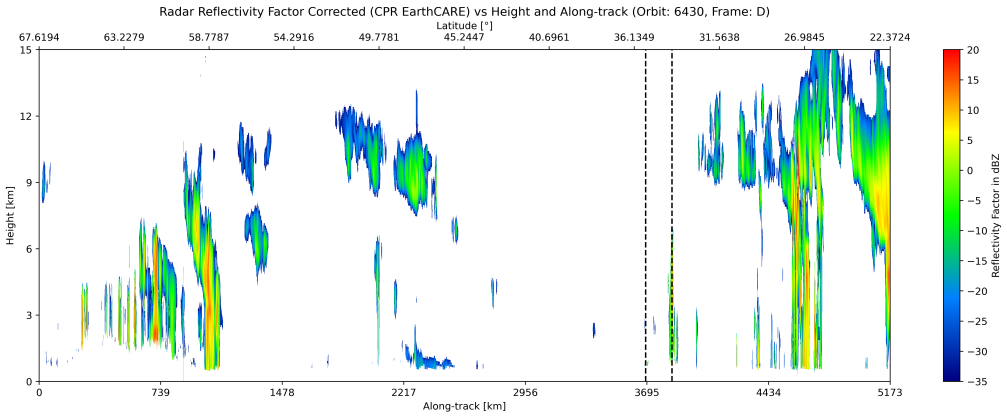

Figure 6.21: Reflectivity observed by the CPR on board EarthCARE on 16 July 2025

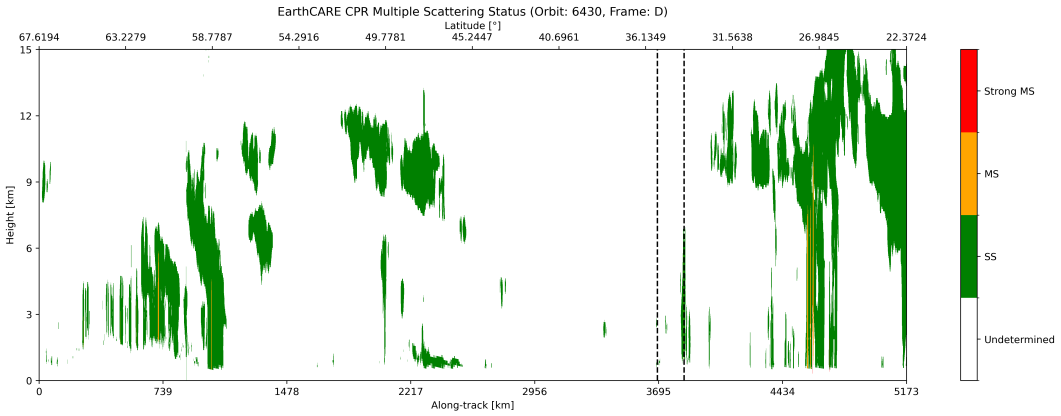

Figure 6.22: MS status observed by the CPR on board EarthCARE on 16 July 2025

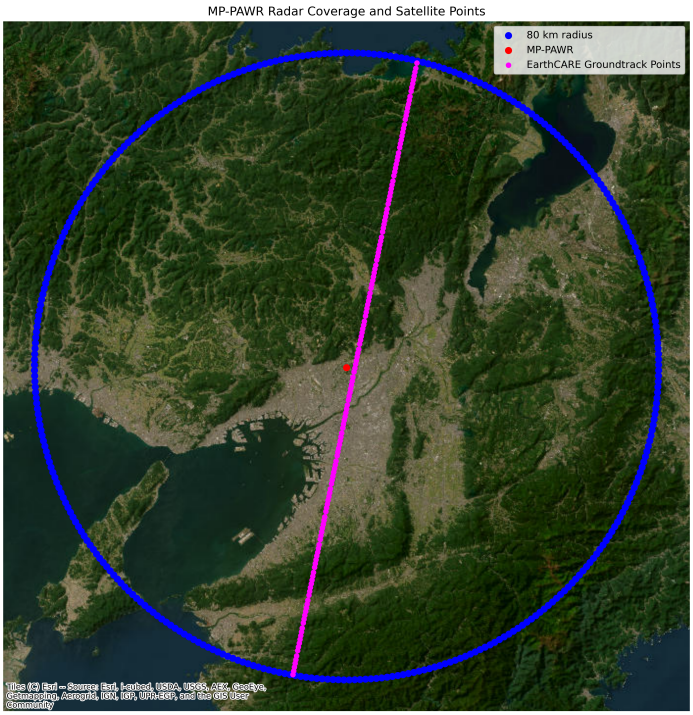

Figure 6.23: MP-PAWR scan volume overlaid with satellite positions on 16 July 2025

The script outputs the satellite positions in terms of latitude and longitude at one-second intervals. The satellite enters the scanning volume at 05:13:39.480883 UTC with coordinates $Lat = 35.521058°$ and $Long = 135.719696°$, and exits at 05:14:01.345063 UTC with coordinates $Lat = 34.113956°$ and $Long = 135.372310°$. The closest distance between the ground-based radar and the EarthCARE radar is 2.13 km, computed at the same latitude.
The reflectivity and multiple-scattering conditions within the target volume can also be visualized.

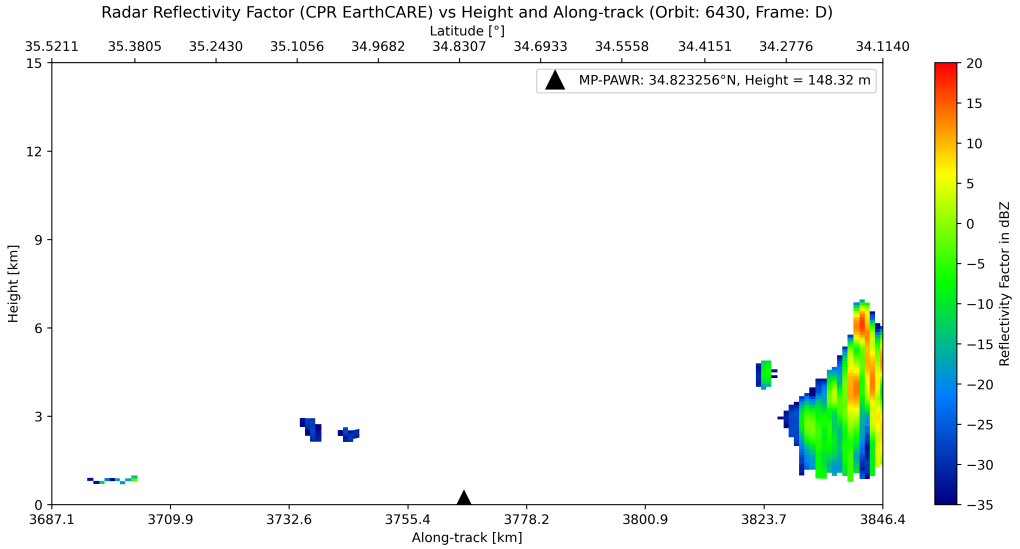

Figure 6.24: Reflectivity of the CPR within the area of interest on 16 July 2025

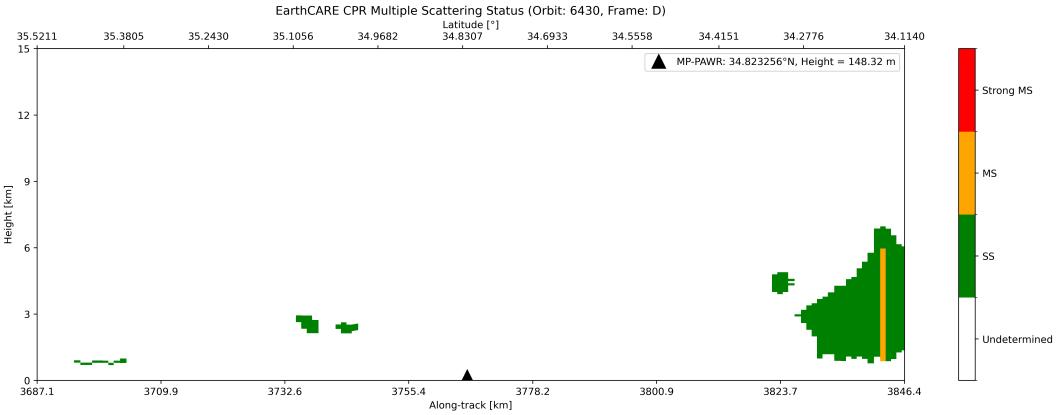

Figure 6.25: Multi-scattering occurrence within the area of interest on 16 July 2025

Three-dimensional visualization of MP-PAWR data obtained by transforming measurements from polar to Cartesian coordinates. The figure compares the horizontal polarization reflectivity fields with and without the application of the MTI filter.

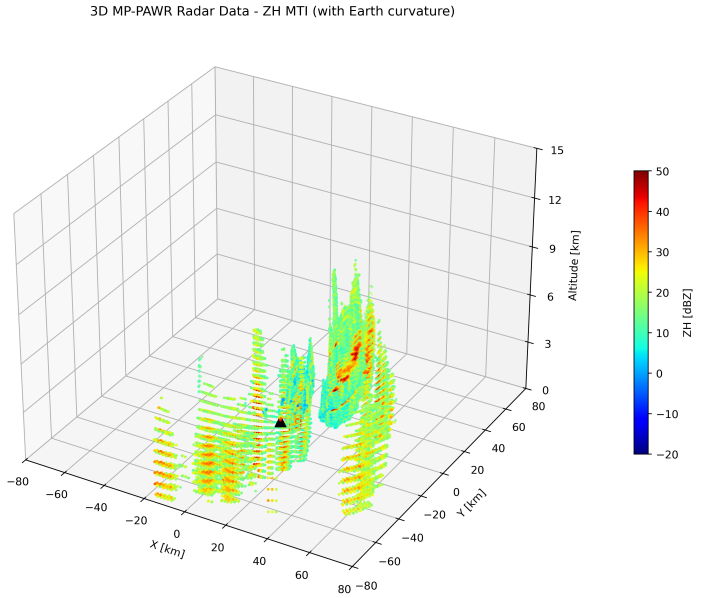

Figure 6.26: 3D visualization with MTI on 16 July 2025

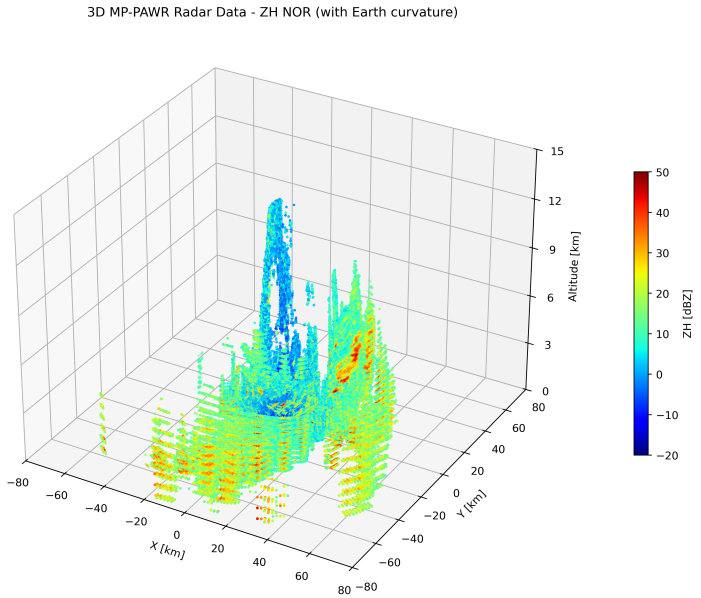

Figure 6.27: 3D visualization without MTI on 16 July 2025

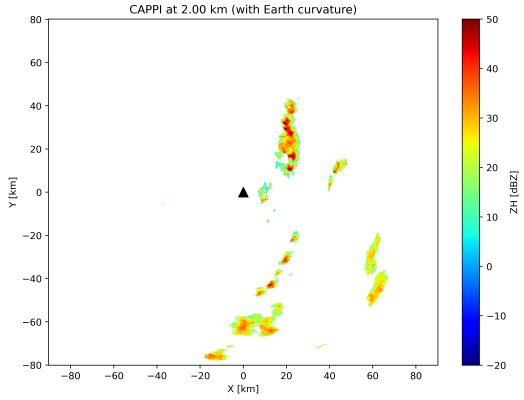

(a) With MTI filter

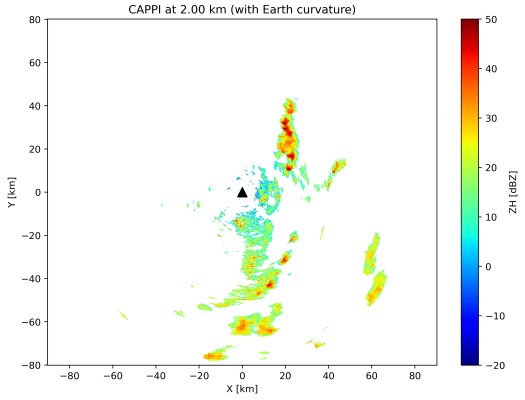

(b) Without MTI filter

Figure 6.28: Plan Position Indicator (PPI) at 2 km altitude on on 16 July 2025

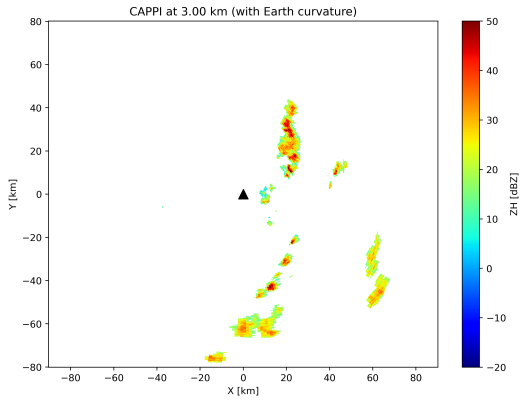

(a) With MTI filter

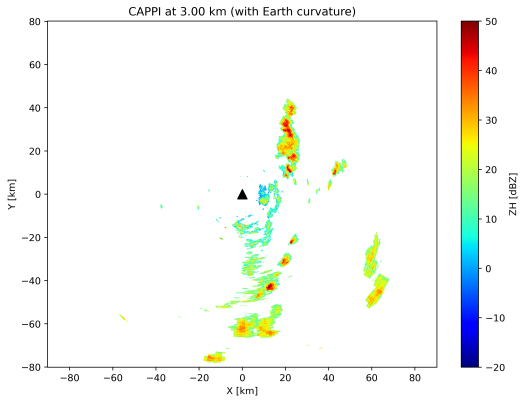

(b) Without MTI filter

Figure 6.29: Plan Position Indicator (PPI) at 3 km altitude on 16 July 2025

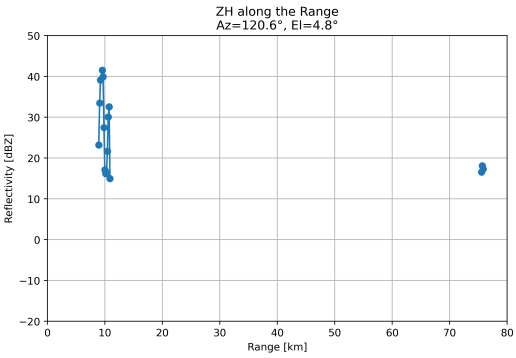

(a) With MTI filter

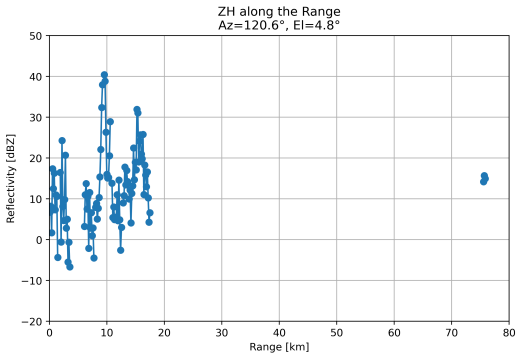

(b) Without MTI filter

Figure 6.30: ZH along the range at fixed azimuth 120.6° and elevation 4.8° on 16 July 2025

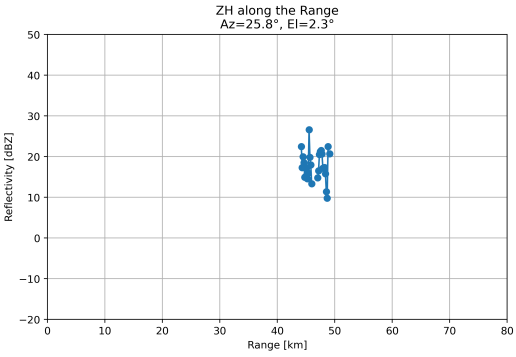

(a) With MTI filter

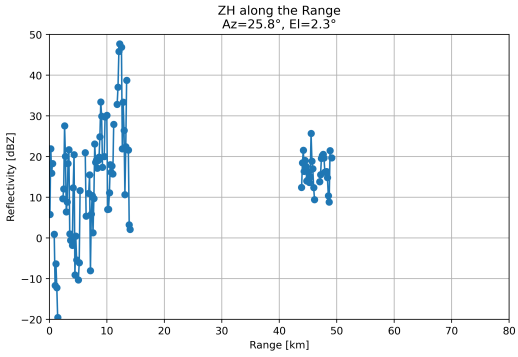

(b) Without MTI filter

Figure 6.31: ZH along the range at fixed azimuth 25.8° and elevation 2.3° on 16 July 2025

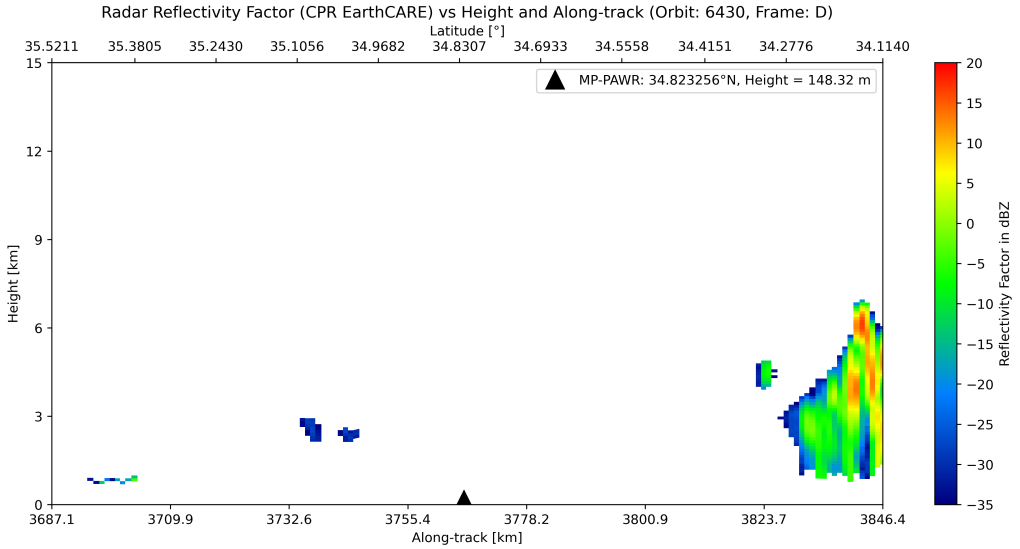

Figure 6.32: Reflectivity of the CPR on 16 July 2025

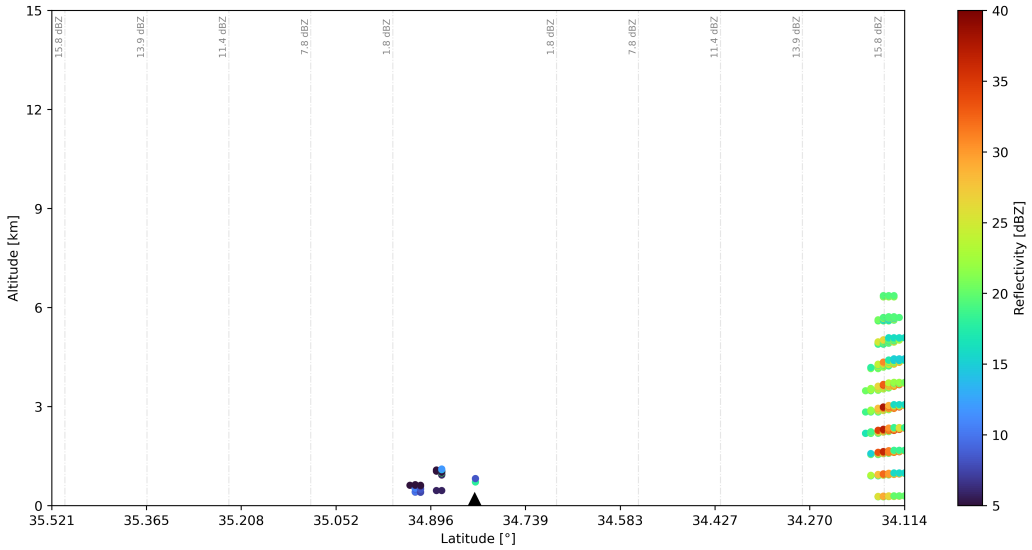

Figure 6.33: MP-PAWR vertical reflectivity profile showing dBZ contour lines, observed on 16 July 2025

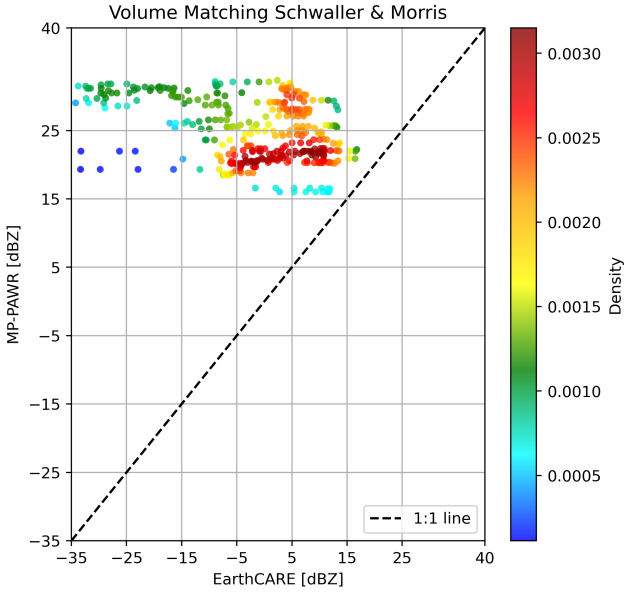

Figure 6.34: Scatter plot of reflectivity on 16 July 2025

Metric	Value
Global Bias (dB)	26.77
RMSE (dB)	30.23
Pearson correlation coefficient	-0.346

Table 6.2: Statistical comparison on 16 July 2025

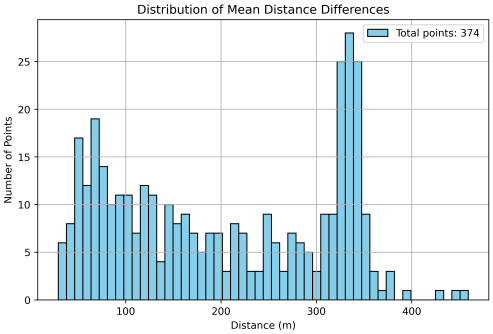

(a) Mean spatial error on 16 July 2025

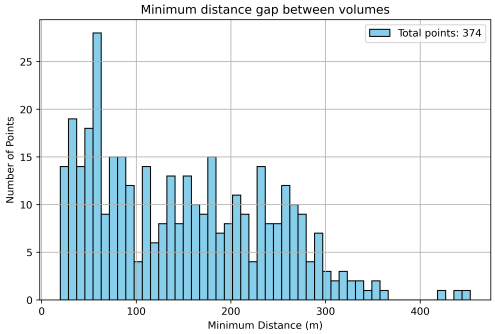

(b) Minimum spatial error on 16 July 2025

Figure 6.35: Mean and minimum spatial errors on 16 July 2025

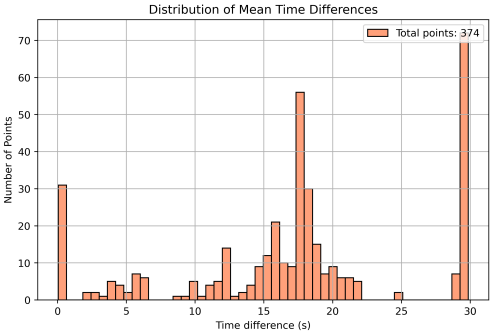

(a) Mean temporal error on 16 July 2025

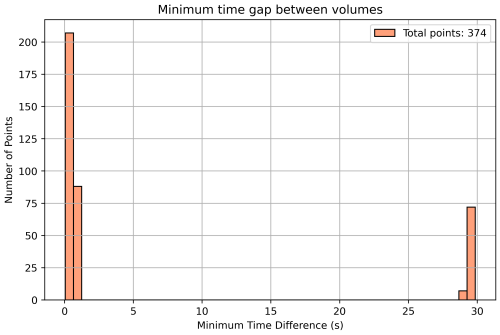

(b) Minimum temporal error on 16 July 2025

Figure 6.36: Mean and minimum temporal errors on 16 July 2025

6.2.3 Study Case 3

The same methodology and figure formatting used in Case Study 1 are maintained. Here, only the results specific to this date and orbit are presented.
Case Study 3 focuses on August 10th, 2025, during which a ground track visualization was generated for orbit 6819 and frame D.

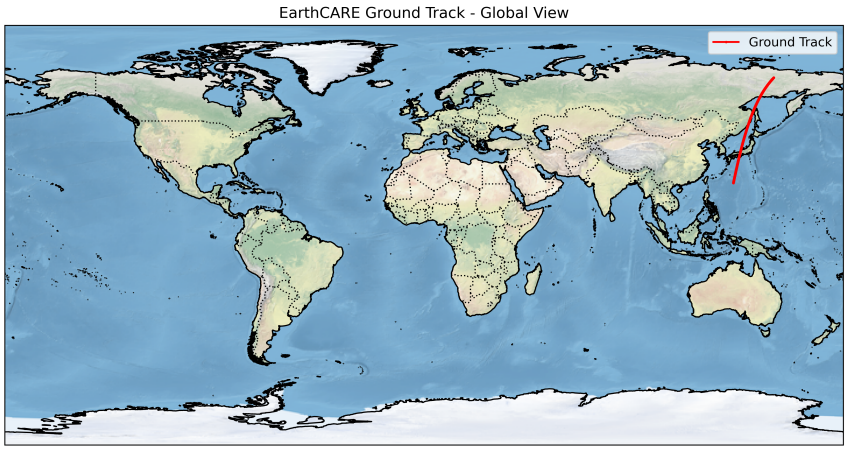

Figure 6.37: EarthCARE global ground track on 10 August 2025

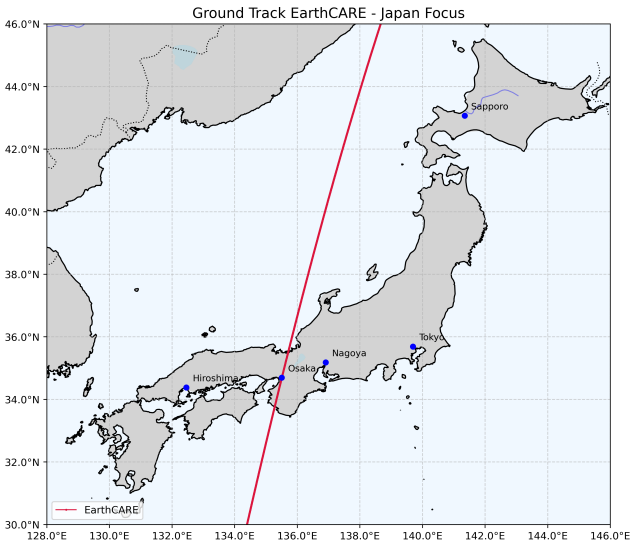

Figure 6.38: EarthCARE ground track above Japan on 10 August 2025

Subsequently, the reflectivity and Multi Scattering status for the entire frame can be retrieved, as illustrated in the figures below.

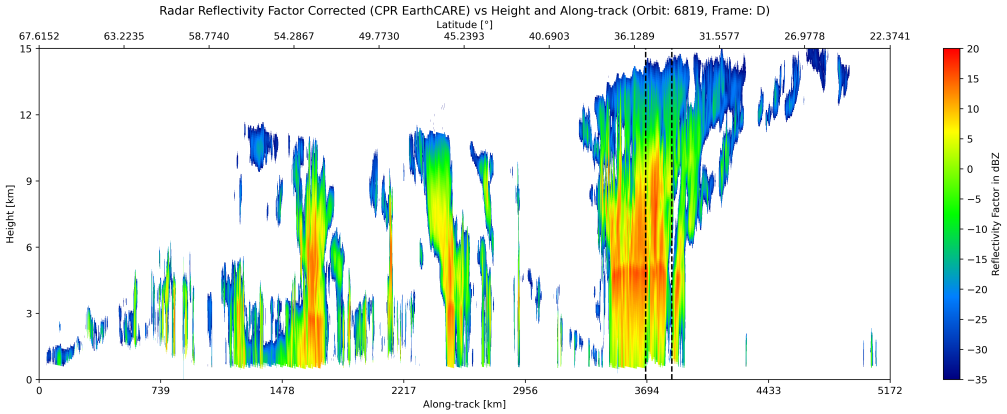

Figure 6.39: Reflectivity observed by the CPR on board EarthCARE on 10 August 2025

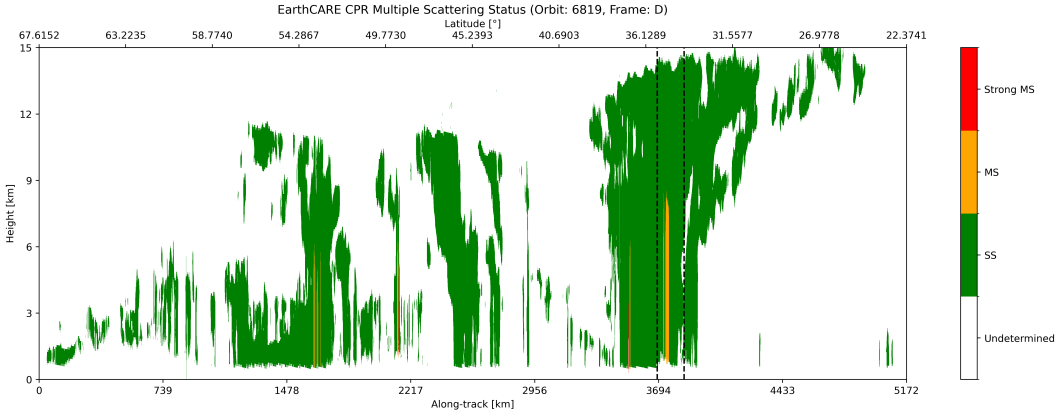

Figure 6.40: MS status observed by the CPR on board EarthCARE on 10 August 2025

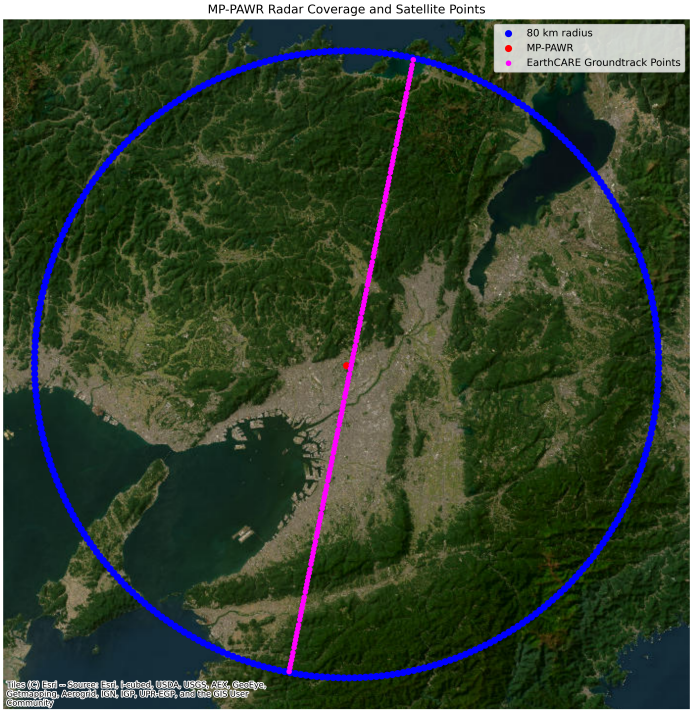

Figure 6.41: MP-PAWR scan volume overlaid with satellite positions on 10 August 2025

The script provides the satellite positions in latitude and longitude at one-second intervals. The satellite enters the scan volume at 05:13:32.593099 UTC with coordinates $Lat = 35.523775°$ and $Long = 135.709889°$, and leaves at 05:13:54.457381 UTC with coordinates $Lat = 34.116706°$ and $Long = 135.361854°$. The minimum distance between the ground radar and the EarthCARE radar is 1.21 km, evaluated at the same latitude.
Reflectivity and multiple-scattering conditions inside the target volume can also be displayed.

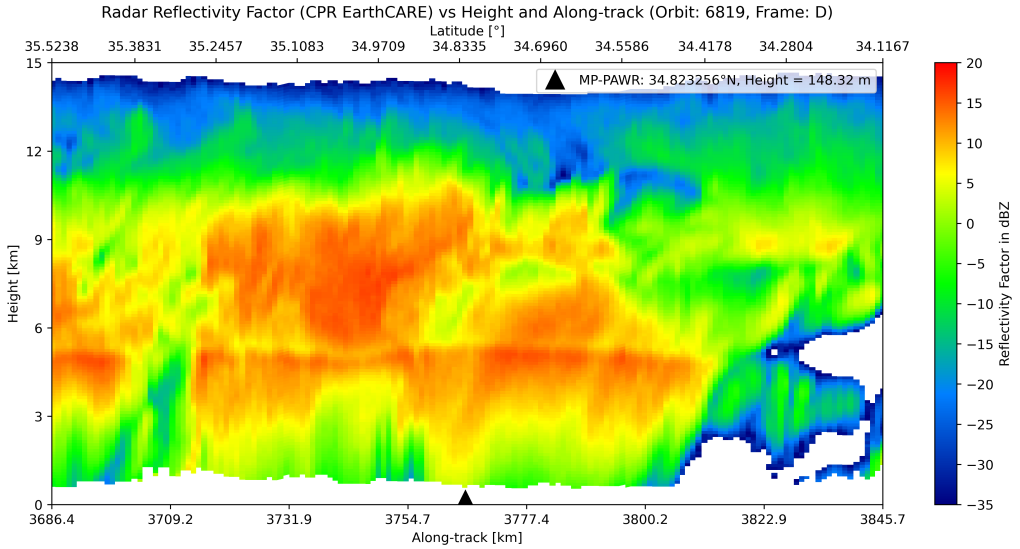

Figure 6.42: Reflectivity of the CPR within the area of interest on 10 August 2025

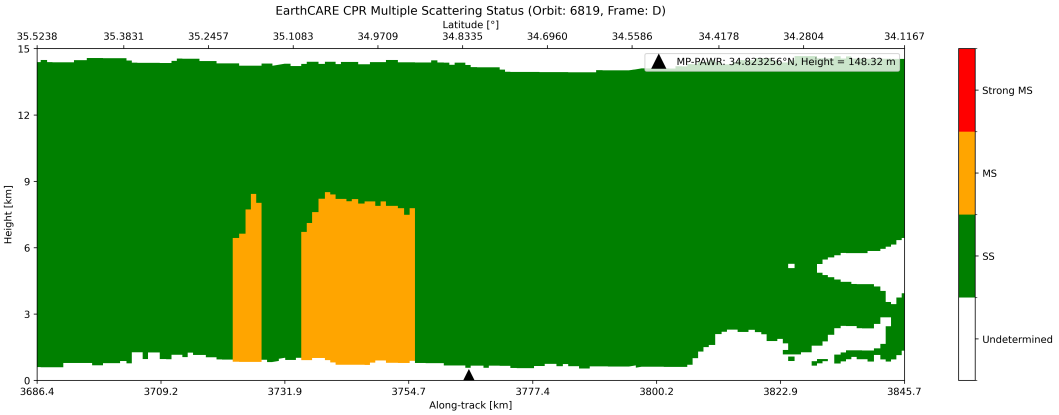

Figure 6.43: Multi-scattering occurrence within the area of interest on 10 August 2025

Three-dimensional visualization of MP-PAWR data obtained by transforming measurements from polar to Cartesian coordinates. The figure compares the horizontal polarization reflectivity fields with and without the application of the MTI filter.

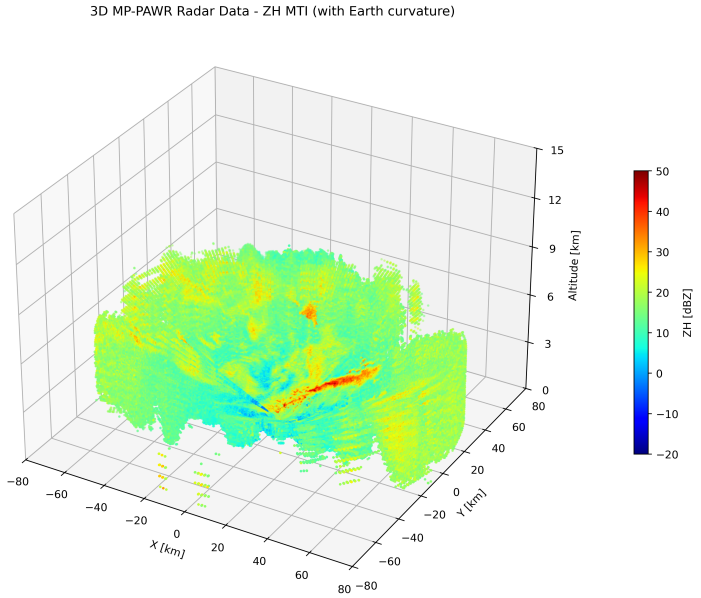

Figure 6.44: 3D visualization with MTI on 10 August 2025

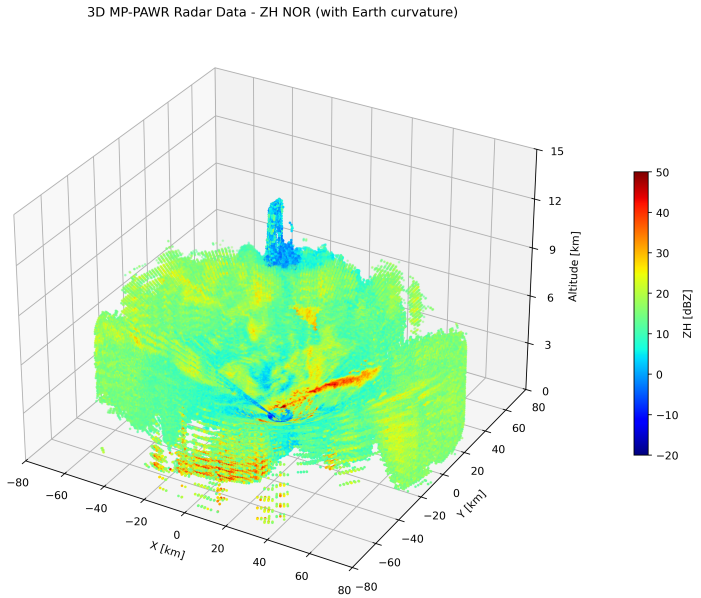

Figure 6.45: 3D visualization without MTI on 10 August 2025

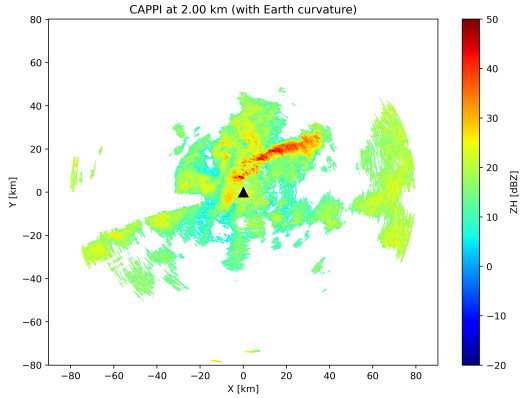

(a) With MTI filter

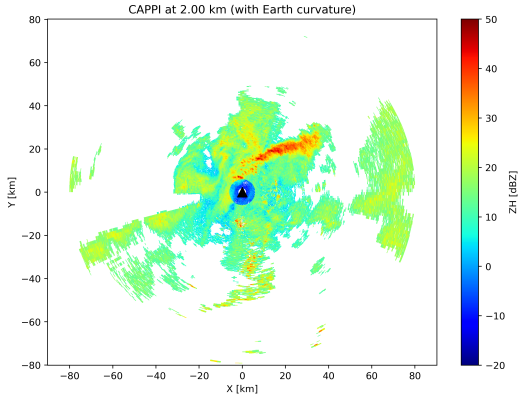

(b) Without MTI filter

Figure 6.46: Plan Position Indicator (PPI) at 2 km altitude on 10 August 2025

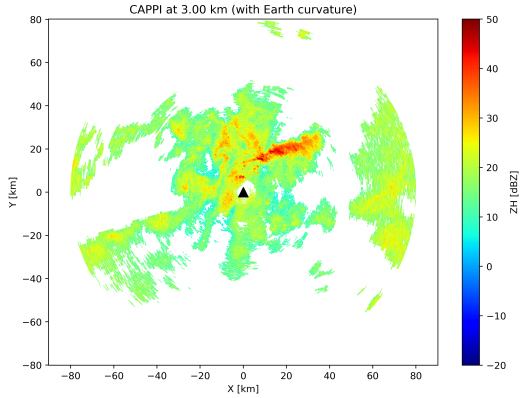

(a) With MTI filter

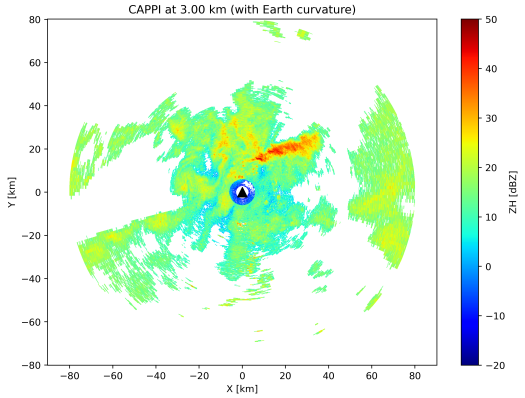

(b) Without MTI filter

Figure 6.47: Plan Position Indicator (PPI) at 3 km altitude on 10 August 2025

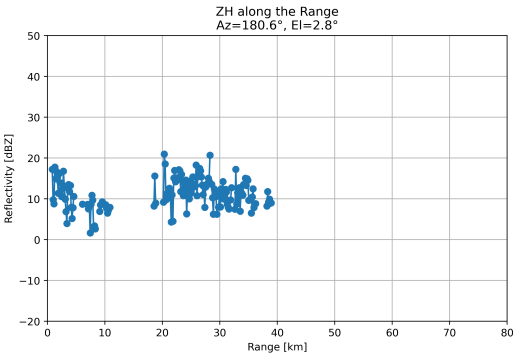

(a) With MTI filter

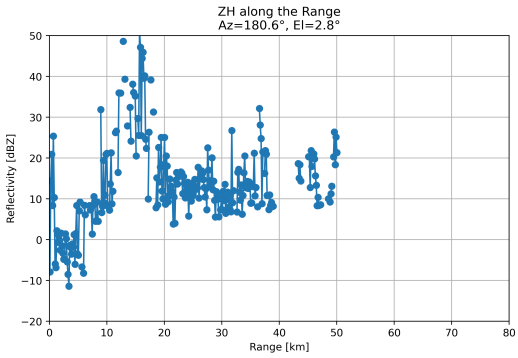

(b) Without MTI filter

Figure 6.48: ZH along the range at fixed azimuth 180.6° and elevation 2.8° on 10 August 2025

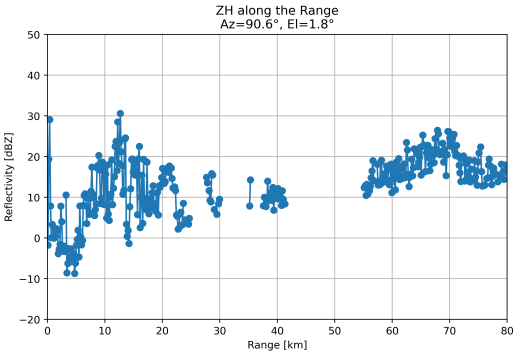

(a) With MTI filter

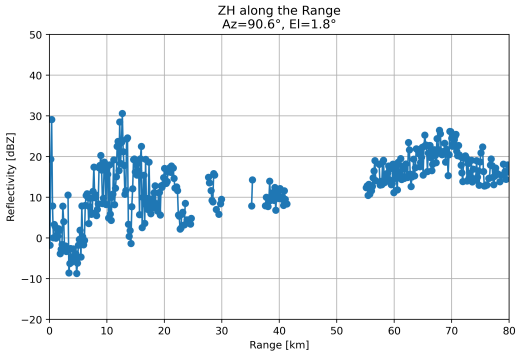

(b) Without MTI filter

Figure 6.49: ZH along the range at fixed azimuth 90.6° and elevation 1.8° on 10 August 2025

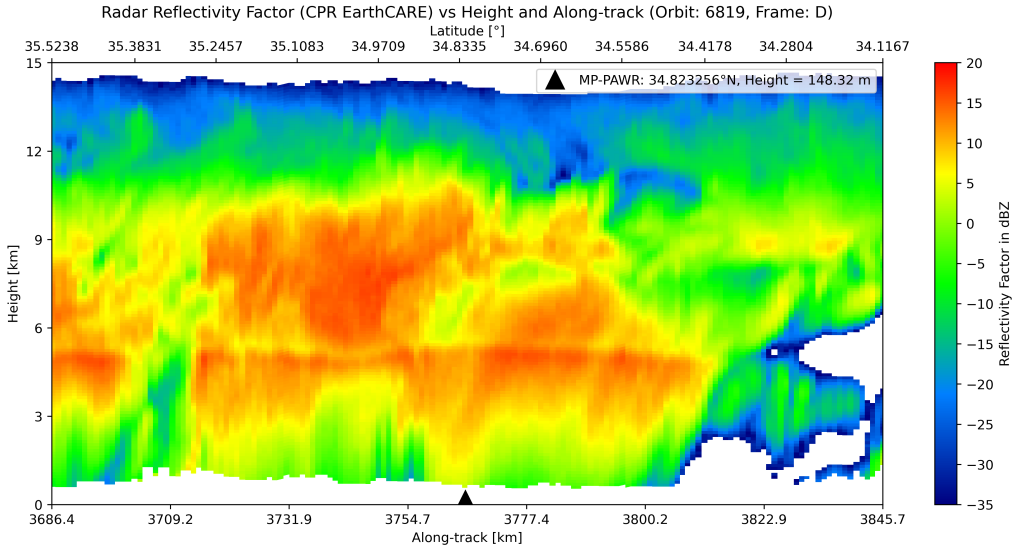

Figure 6.50: Reflectivity of the CPR on 10 August 2025

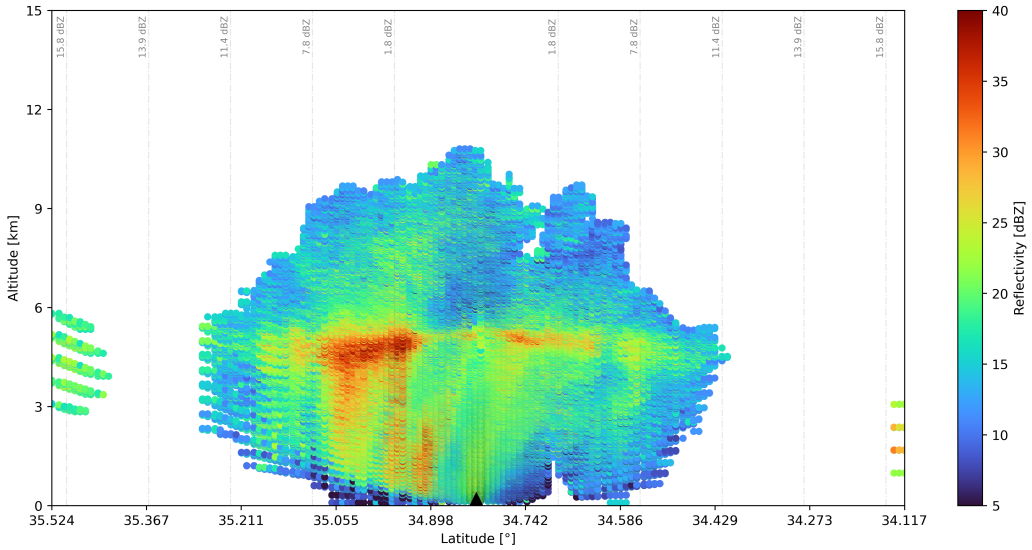

Figure 6.51: MP-PAWR vertical reflectivity profile showing dBZ contour lines, observed on 10 August 2025

Figure 6.50 shows a well-defined vertical structure of the cloud field observed by the EarthCARE CPR. In the upper troposphere (11-15 km), a widespread cirrus layer is visible, characterized by very low reflectivity values. The light–blue to blue shading corresponds to reflectivities between approximately −20 and −35,dBZ, typical of thin ice clouds composed of small ice crystals. These features are well detected thanks to the high sensitivity of the W-band (94 GHz) radar. The irregular upper boundary reflects the instrument noise floor, while localized increases in reflectivity, reaching about −10, dBZ, indicate regions containing thicker or denser ice. Between roughly 3 and 10 km, a large yellow–orange–red region denotes an extensive deep stratiform cloud system with embedded convection. The presence of bright vertical columns rising to 8–10 km suggests embedded convective towers, whereas more homogeneous areas with moderate reflectivity are typical of stratiform precipitation and ice. In this region, reflectivity values reach up to +15–20,dBZ, which are consistent with W-band observations of mixed-phase hydrometeors.

Around 4–5 km, a thin and horizontally continuous band of enhanced reflectivity (yellow–orange colors) marks the melting layer or bright band, where snowflakes transform into raindrops. Here, reflectivity increases by approximately 3–5 dBZ compared with the ice layer above. Despite operating at W-band, the CPR clearly captures this classical melting signature.

Below the melting layer, reflectivity weakens and becomes more irregular and patchy, with values typically between −5 and +5,dBZ. This behaviour indicates the presence of evaporating precipitation (virga), small raindrops, or residual ice particles, combined with the strong attenuation characteristic of 94 GHz radar measurements.

Near the surface (0–1 km), the irregular light-blue to white boundary is caused by ground clutter and surface backscatter rather than precipitation. The CPR surface echo is typically strong and generates a sharp lower limit in the reflectivity field.

Finally, a weak-echo region can be identified on the right side of the transect (3800–3825 km). The dark-blue or near-zero reflectivity between 7 and 12 km is likely associated with very thin ice clouds producing returns close to the noise level.

The second Figure 6.51 shows a vertical cross section reconstructed by the MP-PAWR using the multi-RHI technique. Compared to the CPR, the X-band radar provides much better spatial resolution near the ground, but it has significantly lower sensitivity above 10–12 km. As a result, the upper

part of the cloud is not fully captured.
A well-defined convective–stratiform structure is visible between 3 and 9 km, corresponding to the main body of the cloud. In this region, reflectivity values range from 20 to 30 dBZ, with local maxima up to 35–40 dBZ near the central sector (latitude $\approx 34.90°$). These values are noticeably higher than those observed by the CPR because the MP-PAWR operates in X-band rather than W-band. X-band measurements are less sensitive to small particles and less affected by attenuation at high altitudes, thereby highlighting larger hydrometeors typically found in the mixed or liquid phase regions.
The 35–40 dBZ peak suggests either a strong melting layer signature or a moderately intense convective core with grown hydrometeors (graupel, wet snow, or heavy rain).
The melting layer is very prominent in the MP-PAWR data: it appears as a bright horizontal band (orange–red colors) around 4.5–5 km, much stronger than in the CPR observations. This is consistent with the expected behavior, as the melting layer produces a stronger electromagnetic signature in X-band, whereas it is more subdued in W-band.
Below 4 km, precipitation reaches the surface, with reflectivity values between 10 and 25 dBZ, typical of moderate rainfall. In the central region, just below the melting layer, some deep-blue patches indicate X-band attenuation caused by intense rain along the radar path.
In the upper part of the cloud (above 10–11 km), the density of detected points decreases sharply. The MP-PAWR cannot observe the thin cirrus layers detected by the CPR (–25/–30 dBZ) because its operational sensitivity at such ranges is typically around +5 to +10 dBZ. The high cloud is therefore present but remains below the X-band radar's detection threshold.
Finally, unlike the CPR, the virga is almost absent in the MP-PAWR data. This is due to the limited sensitivity of X-band to very small hydrometeors and to the dominance of noise and ground clutter below the cloud base.
Following a visual inspection of the data, a quantitative comparison can be performed using a scatter plot based on the volumetric matching method of Schwaller & Morris. This approach pairs measurements from the two radars by identifying overlapping volumes in space, taking into account the differing resolution and orientation of each instrument's measurement volumes. In the resulting scatter plot (Figure 6.52), the x-axis shows the reflectivity values recorded by EarthCARE, while the y-axis displays the corresponding measurements from the MP-PAWR radar.

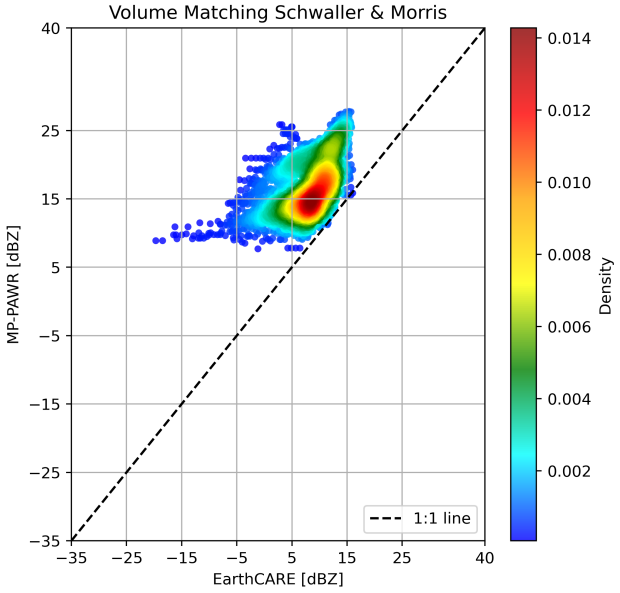

Figure 6.52: Scatter plot of reflectivity on 10 August 2025

Metric	Value
Global Bias (dB)	8.84
RMSE (dB)	9.79
Pearson correlation coefficient	0.522

Table 6.3: Statistical comparison on 10 August 2025

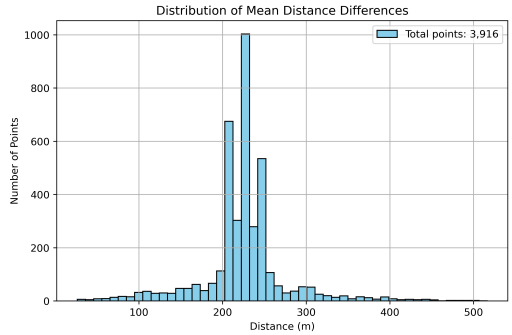

(a) Mean spatial error on 10 August 2025

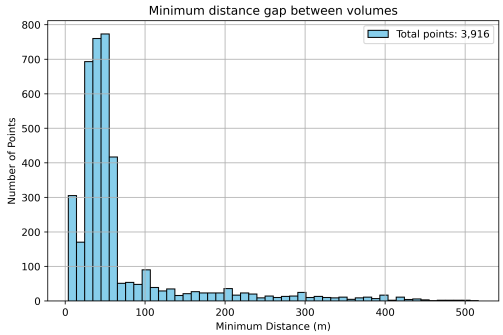

(b) Minimum spatial error on 10 August 2025

Figure 6.53: Mean and minimum spatial errors on 10 August 2025

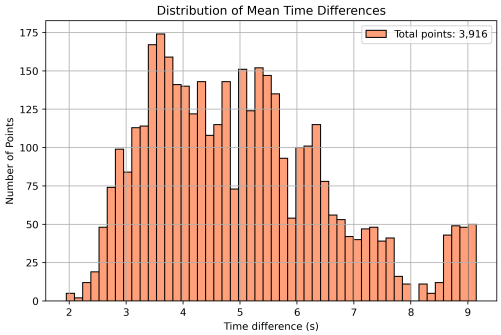

(a) Mean temporal error on 10 August 2025

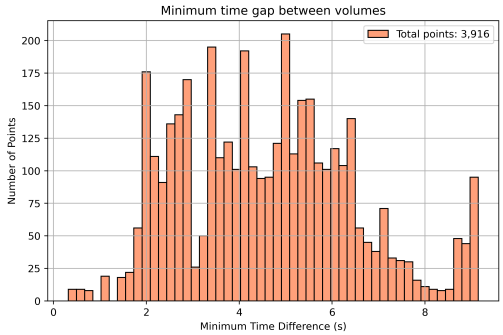

(b) Minimum temporal error on 10 August 2025

Figure 6.54: Mean and minimum temporal errors on 10 August 2025

The figures above indicate that there is no significant spatial or temporal mismatch between the two radar systems. In addition, the temporal error is negligible, which allows the observation of slower phenomena, such as stratiform rain and extended cloud systems, where an acceptable time difference is around 30 seconds. Conversely, for rapidly evolving events, such as convective thunderstorm cells or microbursts, the acceptable temporal difference is on the order of 10 seconds, which is particularly critical for the MP-PAWR measurements.
As highlighted in Case Study 1, Figure 6.52 shows a geolocated point where EarthCARE reports very low reflectivity (around –25 dBZ), while the MP-PAWR measurement is significantly higher. Since no notable spatial or temporal mismatch is present, these discrepancies are likely caused by factors such as differences in viewing geometry, radar frequency, spatial resolution, sensitivity, or possible uncertainties in georeferencing.

Conclusions

The comparison between the Cloud Profiling Radar (CPR) onboard EarthCARE and the ground-based MP-PAWR radar highlights several fundamental differences in radar design, observational capabilities, and the physical regimes they probe. The CPR operates from orbit at a constant altitude, ensuring stable sensitivity throughout its measurements and allowing consistent detection of cloud layers regardless of range. In contrast, the MP-PAWR is a ground-based radar whose sensitivity decreases with distance, so at long ranges small hydrometeors may not be detected due to signal attenuation and beam spreading, making the minimum detectable reflectivity range-dependent.

Another key difference concerns operating frequencies and target applications. The CPR operates at 94 GHz (W-band, $\lambda \approx 3.2\,mm$), optimized for observing cloud microphysics, including thin clouds and small hydrometeors. Its high frequency increases sensitivity to small particles but also makes the radar more susceptible to attenuation. The MP-PAWR operates at 9.71 GHz (X-band, $\lambda \approx 3\,cm$) and is designed for observing precipitation and convective phenomena such as heavy rain, hail, and tornadoes. The lower frequency allows detection of larger hydrometeors (up to approximately 3 cm in diameter) with reduced attenuation, making it suitable for intense precipitation events. Consequently, the CPR cannot accurately measure high-reflectivity rainfall above roughly 20 dBZ, whereas the MP-PAWR can detect light precipitation only down to around 5 dBZ.

This lower sensitivity limit of the MP-PAWR is partly related to the Moving Target Indicator (MTI) implemented to filter out stationary echoes from the ground or fixed objects and isolate returns from moving hydrometeors. While effective at reducing clutter, the MTI introduces a minimum signal threshold: very weak echoes, corresponding to light precipitation or small hydrometeors, can be attenuated or removed, establishing the practical detection limit around 5 dBZ.

Differences in frequency also affect the scattering regimes observed by the two radars. At X-band, the MP-PAWR wavelength is often larger than hydrometeor size, so scattering occurs primarily in the Rayleigh regime, where the backscattered intensity strongly depends on wavelength, scattering is nearly isotropic, and polarization effects are relatively simple to interpret. At W-band, the CPR wavelength is often comparable to hydrometeor size, placing scattering in the Mie regime, where scattering depends complexly on particle size, shape, and orientation, is strongly forward-directed, and produces polarization variations that, although not fully exploited by the single-polarization CPR can affect retrieval accuracy, particularly for larger or non-spherical particles.

Attenuation further differentiates the two radars. High-frequency radars like the CPR are more affected by attenuation, especially in thick clouds or heavy precipitation, reducing returned power from cloud volumes behind dense regions such as cumulonimbus clouds. The MP-PAWR, operating at a lower frequency, can detect hydrometeors through intense rainfall more effectively.

In summary, the CPR and MP-PAWR are designed for complementary purposes: the CPR focuses on high-resolution vertical profiling of clouds and their microphysical properties, while the MP-PAWR observes precipitation and convective events near the surface. Differences in frequency, scattering regime, sensitivity, attenuation, and the presence of the MTI mean that the two radars do not observe exactly the same atmospheric phenomena, making direct validation challenging. Nevertheless, when used together, they provide a comprehensive view linking cloud microphysics to surface precipitation processes, offering valuable insights into both cloud development and severe weather dynamics.

References

[1] Tobias Wehr et al. "The EarthCARE mission – science and system overview". In: *Atmospheric Measurement Techniques* 16.15 (2023), pp. 3581–3608. DOI: 10.5194/amt-16-3581-2023. URL: https://doi.org/10.5194/amt-16-3581-2023.

[2] European Space Agency (ESA). *EarthCARE Instruments Description*. Issue 1. Available at: https://earth.esa.int/eogateway/documents/20142/37627/EarthCARE-instrument-descriptions.pdf. 2017.

[3] A. Protat et al. "CloudSat as a Global Radar Calibrator". In: *Journal of Atmospheric and Oceanic Technology* 28.3 (Mar. 2011), pp. 445–452. DOI: 10.1175/2010JTECHA1443.1. URL: https://doi.org/10.1175/2010JTECHA1443.1.

[4] Pavlos Kollias, Bernat Puigdomènech Treserras, and Alain Protat. "Calibration of the 2007–2017 record of Atmospheric Radiation Measurements cloud radar observations using CloudSat". In: *Atmospheric Measurement Techniques* 12.9 (Sept. 2019), pp. 4949–4964. DOI: 10.5194/amt-12-4949-2019. URL: https://doi.org/10.5194/amt-12-4949-2019.

[5] S. Sasikumar et al. "The Estimation of Path Integrated Attenuation for the EarthCARE Cloud Profiling Radar". In: *EGUsphere* 2025 (2025), pp. 1–25. DOI: 10.5194/egusphere-2025-3573. URL: https://egusphere.copernicus.org/preprints/2025/egusphere-2025-3573/.

[6] J. Kim et al. "Evaluation of the EarthCARE Cloud Profiling Radar (CPR) Doppler velocity measurements using surface-based observations". In: *Atmospheric Chemistry and Physics* 25.21 (2025), pp. 15389–15402. DOI: 10.5194/acp-25-15389-2025. URL: https://acp.copernicus.org/articles/25/15389/2025/.

[7] P. Kollias et al. "Processing reflectivity and Doppler velocity from EarthCARE's cloud-profiling radar: the C-FMR, C-CD and C-APC products". In: *Atmospheric Measurement Techniques* 16.7 (2023),

pp. 1901–1914. DOI: 10.5194/amt-16-1901-2023. URL: https://amt.copernicus.org/articles/16/1901/2023/.

[8] B. Puigdomènech Treserras et al. "EarthCARE's cloud profiling radar antenna pointing correction using surface Doppler measurements". In: *Atmospheric Measurement Techniques* 18.20 (2025), pp. 5607–5618. DOI: 10.5194/amt-18-5607-2025. URL: https://amt.copernicus.org/articles/18/5607/2025/.

[9] A. Galfione et al. "First insights into deep convection by the Doppler velocity measurements of the EarthCARE Cloud Profiling Radar". In: *Atmospheric Measurement Techniques* 18.22 (2025), pp. 6747–6763. DOI: 10.5194/amt-18-6747-2025. URL: https://amt.copernicus.org/articles/18/6747/2025/.

[10] P. Kollias et al. "Evaluation of EarthCARE Cloud Profiling Radar Doppler Velocity Measurements in Particle Sedimentation Regimes". In: *Journal of Atmospheric and Oceanic Technology* 31.2 (2014), pp. 366–386. DOI: 10.1175/JTECH-D-11-00202.1. URL: https://doi.org/10.1175/JTECH-D-11-00202.1.

[11] A. Battaglia and P. Kollias. "Using Ice Clouds for Mitigating the EarthCARE Doppler Radar Mispointing". In: *IEEE Transactions on Geoscience and Remote Sensing* 53.4 (Apr. 2015), pp. 2079–2085. DOI: 10.1109/TGRS.2014.2353219.

[12] H. Horie, Y. Ohno, and N. Takahashi. "The external calibration study for EarthCARE/CPR". In: *2010 IEEE International Geoscience and Remote Sensing Symposium*. 2010, pp. 1895–1898. DOI: 10.1109/IGARSS.2010.5650733. URL: https://doi.org/10.1109/IGARSS.2010.5650733.

[13] Z. Xu et al. "EarthCARE Cloud Profiling Radar Observations of the Vertical Structure of Marine Stratocumulus Clouds". In: *EGUsphere* 2025 (2025), pp. 1–22. DOI: 10.5194/egusphere-2025-5421. URL: https://egusphere.copernicus.org/preprints/2025/egusphere-2025-5421/.

[14] Michael Eisinger et al. "The EarthCARE mission – science data processing chain overview". In: *Atmospheric Measurement Techniques* 17.2 (2024), pp. 839–862. DOI: 10.5194/amt-17-839-2024. URL: https://doi.org/10.5194/amt-17-839-2024.

[15] V. Chandrasekar, R. M. Beauchamp, and R. Bechini. *Introduction to Dual Polarization Weather Radar: Fundamentals, Applications, and Networks*. Cambridge University Press, 2023. ISBN: 9781108423175.

[16] V. N. Bringi and V. Chandrasekar. *Polarimetric Doppler Weather Radar: Principles and Applications*. Cambridge, UK: Cambridge University Press, 2001.

[17] Alessandro Battaglia et al. "Multiple-scattering in radar systems: A review". In: *Journal of Quantitative Spectroscopy & Radiative Transfer* 111.6 (2010), pp. 917–947. DOI: 10.1016/j.jqsrt.2009.11.024. URL: https://doi.org/10.1016/j.jqsrt.2009.11.024.

[18] A. Battaglia, M. O. Ajewole, and C. Simmer. "Evaluation of radar multiple scattering effects in CloudSat configuration". In: *Atmospheric Chemistry and Physics* 7.7 (2007), pp. 1719–1730. DOI: 10.5194/acp-7-1719-2007. URL: https://doi.org/10.5194/acp-7-1719-2007.

[19] A. Battaglia and C. Simmer. "How Does Multiple Scattering Affect the Spaceborne W-Band Radar Measurements at Ranges Close to and Crossing the Sea-Surface Range?" In: *IEEE Transactions on Geoscience and Remote Sensing* 46.6 (2008), pp. 1644–1651. DOI: 10.1109/TGRS.2008.916085. URL: https://doi.org/10.1109/TGRS.2008.916085.

[20] A. Battaglia and S. Tanelli. "DOMUS: DOppler MUltiple-scattering simulator". In: *IEEE Transactions on Geoscience and Remote Sensing* 49 (2011). DOI: 10.1109/TGRS.2010.2052818. URL: https://doi.org/10.1109/TGRS.2010.2052818.

[21] Alessandro Battaglia et al. "Spaceborne Cloud and Precipitation Radars: Status, Challenges, and Ways Forward". In: *Reviews of Geophysics* 58.3 (2020). DOI: 10.1029/2019RG000686. URL: https://doi.org/10.1029/2019RG000686.

[22] Nobuhiro Takahashi. "Analysis of a Precipitation System that Exists above Freezing Level Using a Multi-Parameter Phased Array Weather Radar". In: *Atmosphere* 10.12 (2019), p. 755. DOI: 10.3390/atmos10120755. URL: https://doi.org/10.3390/atmos10120755.

[23] Toshiba Infrastructure Systems & Solutions Corporation. *Multi Parameter Phased Array Weather Radar (MP-PAWR). Toshiba Sustainability Case Study*. Available at: https://www.global.toshiba/ww/sustainability/corporate/related-information/case/e07.html. 2025.

[24] Nobuhiro Takahashi et al. "Development of Multi-Parameter Phased Array Weather Radar (MP-PAWR) and Early Detection of Torrential Rainfall and Tornado Risk". In: *Journal of Disaster Research* 14.2 (2019), pp. 235–247. DOI: 10.20965/jdr.2019.p0235. URL: https://doi.org/10.20965/jdr.2019.p0235.

[25] Yuuki Wada et al. "Performance Verification of Dual-Polarized X-Band Phased Array Weather Radar at Osaka University". In: *Proc. 12th European Conference on Radar in Meteorology and Hydrology (ERAD 2024)*. Rome, Italy, 2024.

[26] Hsueh-Jyh Li and Yean-Woei Kiang. "Radar and Inverse Scattering". In: *The Electrical Engineering Handbook*. Ed. by Wai-Kai Chen. 1st. Burlington: Academic Press, 2005, pp. 671–690.

[27] M. I. Skolnik, ed. *Radar Handbook*. 3rd. New York: McGraw-Hill, 2008.

[28] D. S. Zrnic and R. J. Doviak. *Doppler Radar and Weather Observations*. Academic Press, 1993.

[29] International Telecommunication Union – Radiocommunication Sector (ITU-R). *Recommendation ITU-R P.838-3: Specific attenuation model for rain for use in prediction methods*. Disponibile su: https://www.itu.int/dms_pubrec/itu-r/rec/p/R-REC-P.838-3-200503-I!!PDF-E.pdf. 2005.

[30] Mathew R. Schwaller and K. Robert Morris. "A Ground Validation Network for the Global Precipitation Measurement Mission". In: *Journal of Atmospheric and Oceanic Technology* 28.3 (2011), pp. 301–319. DOI: 10.1175/2010jtecha1403.1. URL: https://doi.org/10.1175/2010jtecha1403.1.

[31] Steven M. Bolen and V. Chandrasekar. "Methodology for Aligning and Comparing Spaceborne Radar and Ground-Based Radar Observations". In: *Journal of Atmospheric and Oceanic Technology* 20.5 (May 2003), pp. 647–659. DOI: 10.1175/1520-0426(2003)20<647:

MFAACS>2.0.CO;2. URL: https://doi.org/10.1175/1520-0426(2003)20%3C647:MFAACS%3E2.0.CO;2.

[32] Timo Gnambs. "A Brief Note on the Standard Error of the Pearson Correlation". In: *Collabra. Psychology* 9.1 (Sept. 2023). DOI: 10.1525/collabra.87615. URL: https://doi.org/10.1525/collabra.87615.

[33] European Space Agency (ESA). *EarthCARE – Earth Clouds, Aerosols and Radiation Explorer*. Available at: urlhttps://www.esa.int/Applications/Observing_the_Earth/FutureEO/EarthCARE, accessed 14 September 2025. 2021.

[34] European Space Agency (ESA). *EarthCARE for a better understanding of Earth's radiation balance*. Available at: https://earth.esa.int/eogateway/news/earthcare-lifetime-update-mission-targets-2034-and-beyond/earthcare-for-abetter-understanding-of-earth-s-radiation-balance, accessed 14 September 2025.

[35] National Institute of Information and Communications Technology (NICT). *Multi Parameter Phased Array Weather Radar (MP-PAWR). NICT NEWS No. 498*. Available at: https://www.nict.go.jp/en/data/nict-news/NICT_NEWS498/book/pdf/7.pdf. 2023.

[36] Keitaro Asai et al. "Validation of X-Band Multiparameter Phased-Array Weather Radar by Comparing Data from Doppler Weather Radar with a Parabolic Dish Antenna". In: *Journal of Atmospheric and Oceanic Technology* 38.9 (2021), pp. 1561–1571. DOI: 10.1175/JTECH-D-20-0213.1. URL: https://doi.org/10.1175/JTECH-D-20-0213.1.

[37] A. Battaglia et al. "Multiple scattering identification in spaceborne W-band radar measurements of deep convective cores". In: *Journal of Geophysical Research* 116.D19 (2011), p. D19201. DOI: 10.1029/2011JD016142. URL: https://doi.org/10.1029/2011JD016142.

[38] Sergey Y. Matrosov, Alessandro Battaglia, and Peter Rodriguez. "Effects of Multiple Scattering on Attenuation-Based Retrievals of Stratiform Rainfall from CloudSat". In: *Journal of Atmospheric and Oceanic Technology* 25.12 (2008), pp. 2199–2208. DOI: 10.1175/2008JTECHA1095.1. URL: https://doi.org/10.1175/2008JTECHA1095.1.

[39] Haonan Chen and V. Chandrasekar. "Validation of NASA's Global Precipitation Measurement mission with a high-resolution ground radar network". In: *2016 URSI Asia-Pacific Radio Science Conference (URSI AP-RASC)*. 2016, pp. 836–839. DOI: 10.1109/URSIAP-RASC.2016.7601343. URL: https://doi.org/10.1109/URSIAP-RASC.2016.7601343.

[40] Ji-Hye Kim et al. "Global Precipitation Measurement (GPM) Ground Validation (GV) Prototype in the Korean Peninsula". In: *Journal of Atmospheric and Oceanic Technology* 31.9 (Sept. 2014), pp. 1902–1921. DOI: 10.1175/JTECH-D-13-00193.1. URL: https://doi.org/10.1175/JTECH-D-13-00193.1.

[41] K. Siegrist. *Probability and Statistics Online Textbook*. University of Alabama in Huntsville. retrieved October 29, 2025. URL: https://stats.libretexts.org/Bookshelves/Probability_Theory/Probability_%20Mathematical_Statistics_and_Stochastic_Processes_(Siegrist).

[42] Yuuki Wada et al. "Phase and Amplitude Correction for Adaptive Beamforming of Phased Array Weather Radar". In: *IEEE Transactions on Geoscience and Remote Sensing* 62 (2024), pp. 1–11. DOI: 10.1109/TGRS.2024.3470118. URL: https://doi.org/10.1109/TGRS.2024.3470118.

[43] David Burns et al. "The performance of the EarthCARE Cloud Profiling Radar in marine stratiform clouds". In: *Journal of Geophysical Research* 121.24 (Dec. 2016), pp. 14525–14537. DOI: 10.1002/2016JD025090. URL: https://doi.org/10.1002/2016JD025090.

[44] Alessandro Battaglia et al. "Mind the gap – Part 2: Improving quantitative estimates of cloud and rain water path in oceanic warm rain using spaceborne radars". In: *Atmospheric Measurement Techniques* 13.9 (Sept. 2020), pp. 4865–4883. DOI: 10.5194/amt-13-4865-2020. URL: https://doi.org/10.5194/amt-13-4865-2020.

[45] Hiroshi Kikuchi et al. "Initial Observations for Precipitation Cores With X-Band Dual Polarized Phased Array Weather Radar". In: *IEEE Transactions on Geoscience and Remote Sensing* 58.5 (May 2020), pp. 3657–3666. DOI: 10.1109/TGRS.2019.2959628. URL: https://doi.org/10.1109/TGRS.2019.2959628.